

## ***Contents — V through Z***

---

Permafrost-related Morphologies in Tempe Terra, Observations and Morphometry <i>S. van Gasselt, E. Hauber, and R. Jaumann</i> .....	3189
Geologic Evolution of Mars' North Polar Layered Deposits and Related Materials from Mars Odyssey THEMIS <i>A. R. Vasavada, M. I. Richardson, S. Byrne, A. B. Ivanov, P. R. Christensen, and the THEMIS Team</i> .....	3156
Automated Analysis of Mars Multispectral Observations <i>K. Wagstaff and J. F. Bell III</i> .....	3120
Investigating Surface Mineralogy, Alteration Processes, and Biomarkers on Mars Using Laser Raman Spectroscopy <i>A. Wang, B. L. Jolliff, and L. A. Haskin</i> .....	3270
Evaluating Putative Shoreline Adjacent to the Dichotomy Boundary near Arabia Terra <i>V. E. Webb and G. E. McGill</i> .....	3108
Potassium in the Martian Core: Implications for an Early Dynamo <i>J.-P. Williams and F. Nimmo</i> .....	3279
Measurements of Dune Heights on Mars <i>K. K. Williams</i> .....	3220
Identification of Topographically-controlled Thermal Tidal Modes in the Martian Upper Atmosphere <i>P. Withers, S. W. Bougher, and G. M. Keating</i> .....	3069
Chemistry Related to Possible Outgassing Sources on Mars <i>A. S. Wong, S. K. Atreya, and N. O. Renno</i> .....	3125
MGS Observations and Modeling of Martian Lee Wave Clouds <i>S. E. Wood, D. C. Catling, S. C. R. Rafkin, E. A. Ginder, and C. G. Peacock</i> .....	3283
Ice Keel Scour Marks on Mars: Evidence for Floating and Grounding Ice Floes in Kasei Valles <i>C. Woodworth-Lynas and J. Y. Guigné</i> .....	3128
Accumulation of Distal Impact Ejecta on Mars Since the Hesperian <i>K. E. Wrobel and P. H. Schultz</i> .....	3242
Basalt, Altered Basalt, and Andesite on the Martian Surface: Observations, Interpretations, and Outstanding Questions <i>M. B. Wyatt, H. Y. McSween Jr., P. R. Christensen, and J. W. Head III</i> .....	3271
H <sub>2</sub> O-Silicate Microphysics in Ascending Volcanic Plumes on Mars <i>A. P. Zent</i> .....	3136
Decameter-scale Ripple-like Features in Nirgal Vallis as Revealed in THEMIS and MOC Imaging Data <i>J. R. Zimbelman</i> .....	3028
The Mars Reconnaissance Orbiter (MRO) Mission <i>R. W. Zurek</i> .....	3290

**PERMAFROST-RELATED MORPHOLOGIES IN TEMPE TERRA, OBSERVATIONS AND MORPHOMETRY.** S. van Gasselt, E. Hauber, R. Jaumann, *German Aerospace Center, Institute of Space Sensor Technology and Planetary Exploration, D-12489 Berlin, Germany, (Stephan.vanGasselt@dlr.de).*

## 1 Introduction

The fretted terrain at the Martian dichotomy boundary shows various permafrost related morphologies. On the basis of Mars Global Surveyor mission data we perform morphometrical analyses of lobate debris aprons and present typical ice related morphologies from high resolution imagery. A variety of landforms indicates the possible existence of past or present ice in the near subsurface of Mars (e.g., [1, 2, 3]). Among the most spectacular ice-related features are lobate debris aprons (LDAs). They have been interpreted to be a mixture of rock particles and interstitial ice (e.g., [4]) analogous to terrestrial rock glaciers (debris transport systems comprising a creeping mixture of rock fragments and segregational or interstitial ice [5]).

Rock glaciers are sensitive indicators for the climatic environment during their formation and - if present on Mars - are thought to be possible large and easily accessible water reservoirs. The analogy between terrestrial rock glaciers and Martian lobate debris aprons is mainly based on the shape of debris aprons and their relationship to adjacent regions with permafrost-related morphology. In this study we will focus on LDA-s in Tempe Terra and investigate LDAs on the basis of high resolution imagery and topographic data. The Tempe Terra area (fig. 1) is characterized by fretted terrain [6], a type of landform often characterizing the dichotomy boundary between southern highlands and northern lowlands on Mars. In particular, we focus on an ubiquitous mantling deposit which might also indicate the past or present existence of near surface ice, but is different from the LDAs.

## 2 Topography and Morphology

The width of the fretted terrain in our study area varies between 60 km to 170 km. The undissected upland has an elevation of -2700 m at 66°W and about 0 m at 80°W. The lowland has its highest elevations also in the western part of the study area (-1700 m) and slopes gently ( $\approx 0.1^\circ$ ) towards NE, reaching minimum elevations of -3600 m at the eastern border of the study area. The elevation difference between uplands and lowlands decreases from  $\approx 3000$  m (at  $\approx 80^\circ$  W) to  $\approx 1500$  m (at  $\approx 66^\circ$  W). This elevation difference is slightly less than that reported from the dichotomy boundary in eastern Mars (2-6 km) [7].

The highlands have a generally very flat surface, sloping at an angle of less than  $0.1^\circ$  when measured perpendicular to the dichotomy boundary. The surfaces of very large upland segments bounded by fretted channels (Fig. 1) have larger slopes toward the lowlands ( $1^\circ$ - $2^\circ$ ) and might be tilted as blocks. Several fretted channels dissect the upland at the dichotomy boundary. Such channels have steep walls and flat floors [4], and their floors are often characterized by "lineated valley fill"

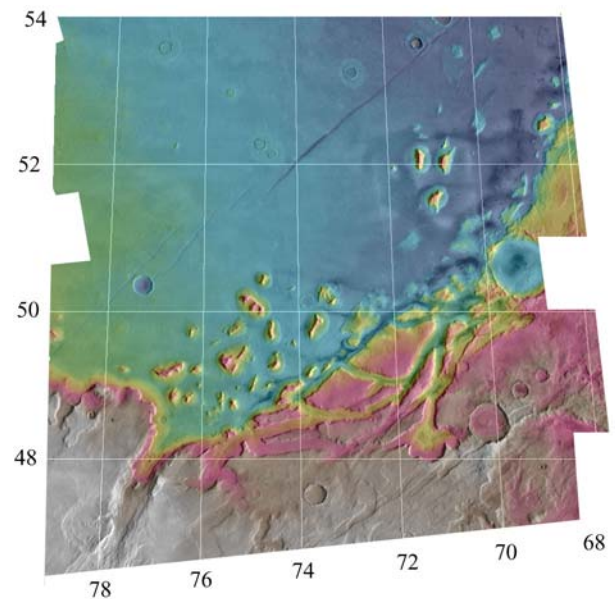


Figure 1: Viking digital image mosaic of the northern Tempe Terra region combined with MOLA topographic data.

[4] [8]. In the study area, they have uniform widths of  $\approx 5$ - $10$  km and constant depths of few hundred meters. On the floors of some fretted channels we identify crevasse-like features.

Their specific geometry resembles that of terrestrial chevron crevasses, which form by a combination of shear stress exerted by the valley walls and -to a minor degree- by longitudinal tensile stress (i.e., extending flow) resulting from glacier bed steepening [9]. We do not know, however, which processes are responsible for the deformation of the mantling deposit. One possibility would be creeping of the mantling deposit, as suggested by [10]. Their orientation seems to be structurally controlled in two ways: One preferred trend is parallel to the Mareotis Fossae ( $N50^\circ$ - $60^\circ$ E), a system of long and narrow grabens. The other is concentric about the center of a possible impact crater in the northern lowlands (center at  $79^\circ$ W,  $56^\circ$ N). Although there is evidence for fluvial sapping on the uplands near the dichotomy boundary, we find no evidence for a fluvial origin and later enlargement of fretted channels.

Very high-resolution images (1.5 - 12 m/pixel) taken with the Mars Orbiter Camera (MOC) onboard the Mars Global Surveyor (MGS) spacecraft show that the surface at the dichotomy boundary in Tempe Terra is covered by a smooth mantling deposit. It is often degraded by erosion, resulting in surfaces whose texture is highly variable, ranging from smooth over stippled, pitted, or knobby to heavily etched. In some places it is completely removed. The disintegration process is controlled by slope aspect (i.e., sun irradiation),

## 3 LOBATE DEBRIS APRONS



Figure 2: The floor of a fretted channel (a) is covered by a mantling deposit. Crevasses (cr) are situated near the channel walls (w). They also outline an impact crater completely buried by the mantle (i). Small image at the bottom left (b) shows a crater filled by the mantling deposit. The mantle seems to have flown out of the crater. Detail of MOC image M03/06586 (6.23 m/pixel).

the southern (sun-lit) slopes being more affected than northern slopes. This indicates the sublimation of a volatile constituent, as previously proposed [11] [12]. The global presence of this mantle at latitudes higher than  $\approx 30\text{-}50^\circ$  in both hemispheres has been inferred from global-scale roughness maps [13] and directly observed in MOC images [11, 14]. It was interpreted to be a mixture of ice and soil which was atmospherically deposited during a recent period of high orbital obliquity less than 100,000 yrs ago [12]. Our investigation of MOC images confirms other observations of this deposit [11, 12]. Several features related to the mantle resemble terrestrial glacial features, and some of them may be attributed to flow or creep processes. An observation in Tempe Terra might support this notion: A little crater ( $\approx 500$  m) is filled with the mantling deposit. Where the crater rim is breached, the mantle seems to have flown out of the crater (Fig. 3). A second possibility is that the underlying material (i.e. the lineated valley fill [4, 8, 15]) might have flown, and that the overlying mantle only mirrors that deformation.

Some images reveal a few more or less well-developed parallel, thin (15-20 m wide) ridges running at  $\pm$  constant elevations along upper channel walls [26]. Although they resemble lateral moraines or washboard moraines, we do not observe any evidence for transport along this valley floor (in agreement with [11] and [16]). These ridges might be related to the degradation of the mantling, and might represent zones of higher resistance of the mantle against erosion.

### 3 Lobate Debris Aprons

Lobate debris aprons have been observed primarily along steep escarpments near the dichotomy boundary [e.g., 17, 19, 11, 20] and the large impact basin of Hellas [e.g., 21]. The morphology of the lobate debris aprons in Tempe Terra is very similar to terrestrial protalus lobes [22,23] which are derived from talus slopes of mountainous permafrost environments. In this study we have observed and analyzed mesas as relics of the ancient highlands and their associated slope aprons in the northern Tempe Terra region on the basis of their morphometry.

We derived geographic coordinates, topographic elevations, lengths, areas and volumes [27]. Assumptions were made with respect to the (a) base of the debris apron, which was assumed to be horizontal and flat [5], and (b) to the volume of that part of the mesa which has been buried by the apron. The volume can be approximated using the apron height (assuming vertical walls) and the mesa area. Thickness estimations, and consequently, volume approximations, are based on DEMs and orthoimagery.

#### 3.1 Topography

The morphologic boundary between highland and lowland areas is characterized by two and sometimes three distinct components, (a) a steep upper slope (the wall-rock), (b) sometimes an intermediate shallow-sloped unit with downslope facing striae, and (c) the highly textured apron [11]. The intermediate unit mentioned by [11] is not observed very often at the

## 3 LOBATE DEBRIS APRONS

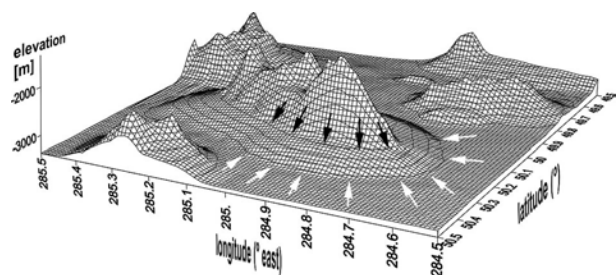


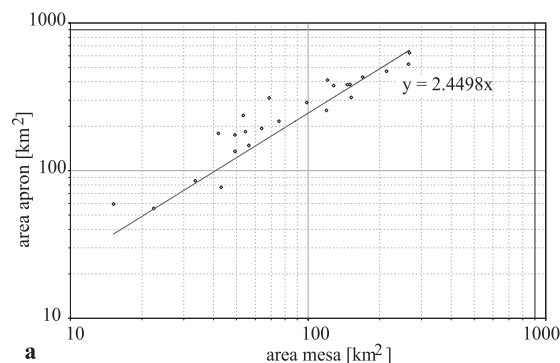
Figure 3: Characteristic morphology of lobate debris aprons at remnants of the ancient highlands. Debris aprons are characterized by a highly convex profile. White arrows are pointing to the footprint, black arrows to the boundary of wall rock to apron.

isolated remnants. At a few sample locations we measured the angles of intermediate units ( $\approx 6^\circ - 8^\circ$ ) and angles of debris aprons ( $\approx 2^\circ - 4^\circ$ ). The results are in agreement with values presented by [11].

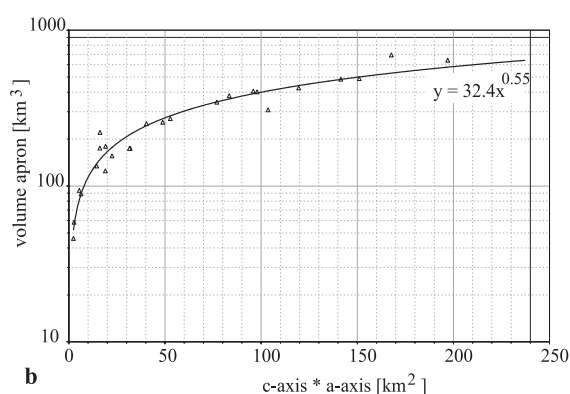
In plan view, the mesas north of the dichotomy boundary have a more or less irregular polygonal shape and a rugged top, in contrast to the more flat-topped mesas of the type locations in Elysium or Arabia Terra. Outwards from the wall rock zone large aprons evolve in radial direction and form an elliptical to circular-shaped footprint. The cross-section shapes of the aprons are convex upward, steepening towards the terminus of the apron (fig. 3). The length of the debris aprons varies between 1.4 km to 6.3 km with an average of  $\approx 4.0$  km in the northern direction and  $\approx 3.5$  km in the southern direction which indicates a dependency on the amount of sun irradiation. The average length of the aprons is less than that given by [20] for Deuteronilus and Protonilus Mensae with 10.8 to 33 km, and also less than that given by [11] and [17] (15 km). No correlation between apron or mesa length and the geographic latitude or the distance to the dichotomy boundary could be found.

The thickness of the (upper) mesas ranges from  $\approx 20$  meters to  $\approx 1100$  meters. The thickness of the aprons varies between  $\approx 70$  and  $\approx 600$  meters assuming a flat base. We observed that the relative thickness of aprons and mesas do not correlate. Furthermore, we cannot observe a correlation between the geographic latitude (or distance from the dichotomy boundary) to the thicknesses of apron or remnant. Minimum thickness values are lower than those given by [20] (276 m), the maximum values are about the same.

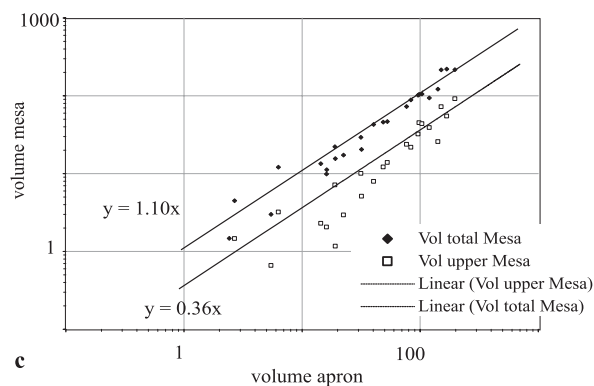
If the size of lobate debris aprons were a direct function of the amount of erosion which has taken place, we would expect a correlation between their sizes and their geographic coordinates. Therefore, it seems appropriate to consider mechanisms which are supported by climatic factors and which are independent of the size and the geographic distribution of remnants.



a



b



c

Figure 4: (a) plot of mesa areas against the area of their aprons. Aprons are about 2.5 times larger than the mesa. (b) plot showing the dependency of apron volumes to apron lengths. Accordingly, Tempe Terra apron volumes can be estimated using the lengths of the apron axes, derived from measurements in orthoimagery. (c) A function of apron volumes against mesa volumes (visible and buried part).

## 4 CONCLUSIONS

## 3.2 Quantitative Volumes and Areas

The mean volume of debris aprons at Tempe Terra (fig. 4b and 4c) ranges from  $\approx 2 \text{ km}^3$  to  $\approx 197 \text{ km}^3$  with a mean surface area of  $\approx 282 \text{ km}^2$ , ranging from  $\approx 56 \text{ km}^2$  to  $\approx 627 \text{ km}^2$  (fig. 4a). The remnant areas have a mean value of  $\approx 115 \text{ km}^2$  (15 to  $417 \text{ km}^2$ , fig. 4a) and a mean volume of  $\approx 21 \text{ km}^3$  (0.04 to  $92 \text{ km}^3$ , fig. 4c). As [5] points out, there is a close relationship between the source area of debris production and the surface area of a rock glacier. The ratio is controlled by bedrock resistance, relief and climate. Other authors proposed values between 1:1.36 to 1:4.4 [24, 25, 26]. Since the source area of debris aprons can be related to isolated steep-walled remnants (i.e., the area of the remnant), we can compare the results for Martian debris aprons. From the regression plot for 27 observations at Tempe Terra (fig. 4a) we obtain a value of  $2.45 \times AS = AR \text{ [km}^2\text{]}$ , with source area (AS) and rock glacier area (AR). The factor ranges from 1.8 to 4.5, which corresponds well with the ratios given in [24, 25, 26]. It must be kept in mind that the method is only valid if the remnant top is not flat but steep, i.e. the entire mesa can be a source for rock glacier debris input. The volumes of the debris apron therefore correlates very well with the remnant volumes (fig. 4c). The volume ratio between wall rock and debris apron represents a key value for remnant degradation. The volume of the visible part of the mesa (the upper part) is about one-third of the volume of the apron (0.36). The calculated total remnant volume and the apron volume show a ratio of  $\approx 1:1.1$ .

We observed that ratios between areas and geographic coordinates (latitude, topographic elevation, and distance from the dichotomy boundary) do not correlate at all. A constant rate of retreat of the dichotomy boundary would result in a gradual distribution concerning sizes, volumes and areas of remnants and aprons.

## 4 Conclusions

In the northern Tempe Terra region of Mars we find a variety of landforms (e.g., degraded mantling deposits, crater-fill, moraine-like features, and lobate debris aprons), which provide abundant evidence for ice-rock or ice-dust interactions. The current environmental conditions on Mars and the morphology and topography demonstrate that there can be active processes near the subsurface. Although we find a general consistency of morphometric ratios at lobate debris aprons, which indicate inactivity, there are strong indicators of active pro-

cesses in the present (degrading mantling deposit). The area, size and volume distributions of lobate debris aprons in Tempe Terra show that present climatic factors have to be considered for their formation.

## References

- [1] Rossbacher, L. A. and S. Judson, *Icarus*, 45, 39-59, 1981.
- [2] Lucchitta, B., *Lun. Planet. Sci.*, 441, 1981. [3] Mason P., M. H. Carr, F. Costard, R. Greeley, E. Hauber, R. Jaumann, *Space Sci. Rev.*, 96, p. 333-364, Kluwer, 2001.
- [4] Squyres, S. W., *Icarus*, 34, 600-613, 1978. [5] Barsch, D., *Rock glaciers*, Springer, Berlin, 1996. [6] Sharp, R. P., *J. Geophys. Res.*, 78, 4073-4083, 1973. [7] Frey, H., S. E. Sakimoto and J. Roark, *J. Geophys. Res.*, 25, p. 4409, 1998.
- [8] Squyres, S. W. *J. Geophys. Res.* 84, p. 8087, 1979. [9] Benn D. I. and D. J. A. Evans, *Glaciers and Glaciation*, Arnold, London, 1998. [10] Milliken, R. E., J. F. Mustard and D. L. Goldsby, *Lun. Planet. Sci. Conf. XXXIII*, #1870, 2002.
- [11] Carr M. H., *J. Geophys. Res.* 106, 23571-23593, 2001. [12] Mustard, J. F., C. D. Cooper and M. K. Rifkin, *Nature*, 6845, p. 411-414, 2001. [13] Kreslavsky, M. and J. Head, *Lun. Planet. Sci. XXXI*, 2000. [14] Malin, M. C. and K. S. Edgett, *Science* 294, 2146, 2001. [15] Lucchitta, B. K., *J. Geophys. Res.*, 89, supp. B409-418, 1984. [16] Hamlin, S., J. Kargel, K. Tanaka, K. Lewis and D. MacAyeal, *Lunar Planet. Sci. Conf.*, XXXI, LPI, Houston, 2000. [17] Colaprete and Jakosky, *J. Geophys. Res.*, 103, p. 5897-5909, 1998. [18] Malin, M. C. and K. S. Edgett, *Lun. Planet. Sci. Conf.*, XXX, #1028, Houston, 1999. [19] Malin, M. C. and K. S. Edgett, *Lun. Planet. Sci. Conf.*, XXXI, #1053, Houston, 2000. [20] Mangold and Allemand, *J. Geophys. Res.*, 28, p. 407-410, 2001. [21] Crown, D. A., T. L. Pierce, S. B. McElfresh and S. C. Mest, *Lun. Planet. Sci. XXXIII*, 2002. [22] Whalley, B. and F. Azizi, *JGR*, 108(E4), 8032, 10.1029/2002JGR001864, 2002. [23] Hamilton, S. and W. B. Whalley, *Geomorphology*, 14, 73-80, 1995. [24] Wahrhaftig, C. and A. Cox, *Geol. Soc. Am. Bull.*, 70: 383-436, 1959. [25] Barsch, D., *Z. Geomorph. N.F. Suppl.-Bd.* 28: 148-160, 1977. [26] Gorbunov, A. P. Fourth International Conference, July 17-22, 1983. Proceedings. Washington DC, National Academic Press, 359-362, 1983. [27] Hauber, E., S. van Gasselt and R. Jaumann, *Lun. Planet. Sci. Conf.*, XXXIII, #1658, Houston, 2002. [28] van Gasselt, S., E. Hauber and R. Jaumann, *Lun. Planet. Sci. Conf.*, XXXIII, #1856, Houston, 2002.

**GEOLOGIC EVOLUTION OF MARS' NORTH POLAR LAYERED DEPOSITS AND RELATED MATERIALS FROM MARS ODYSSEY THEMIS.** A. R. Vasavada<sup>1</sup>, M. I. Richardson<sup>2</sup>, S. Byrne<sup>2</sup>, A. B. Ivanov<sup>3</sup>, P. R. Christensen<sup>4</sup> and the THEMIS Team, <sup>1</sup>Department of Earth and Space Sciences, Box 951567, University of California, Los Angeles, CA 90095-1567, ashwin@ess.ucla.edu, <sup>2</sup>Division of Geological and Planetary Sciences, Mail Stop 150-21, Caltech, Pasadena, CA 90025, <sup>3</sup>Jet Propulsion Laboratory, Mail Stop 168-416, Pasadena, CA 91106, <sup>4</sup>Department of Geological Sciences, Arizona State University, Tempe, AZ 84287.

**Introduction:** The presence of a thick sequence of horizontal layers of ice-rich material at Mars' north pole, dissected by troughs and eroding at its margins, is undoubtedly telling us something about the evolution of Mars' climate [1,2]—we just don't know what yet. The North Polar Layered Deposits (NPLD) most likely formed as astronomically driven climate variations led to the deposition of conformable, areally extensive layers of ice and dust over the polar region. More recently, the balance seems to have fundamentally shifted to net erosion, as evidenced by the many troughs within the NPLD and the steep, arcuate scarps present near its margins, both of which expose layering.

Viking Orbiter imaging of the NPLD revealed that dark, dune-forming material is spatially associated with NPLD scarps [3]. This material may be liberated from an ice matrix by thermal erosion of the NPLD, either as sand particles or sand-sized aggregates of dust [4]. In either case, the NPLD seems to be a source of material similar in particle size and color to that present in the vast, circumpolar sand sea [3].

Recently, the stratigraphy of the NPLD has been subdivided into two unique units [5,6]. Outcrops of the upper unit are smooth and show many fine-scale layers. The lower unit consists of thicker, darker layers with an irregular, platy appearance. This stratigraphic sequence has been observed at widely separated locations within the NPLD [6]. If the layering is truly horizontal over the pole, such that the lowest portions of the stratigraphic column crop out in the marginal scarps, it suggests that the erosion of the platy unit uniquely contributes the dark, dune-forming material. Indeed, the platy unit may be an ancient sand sea now covered by the ice-rich, finely layered unit [6].

Optical and thermal infrared (IR) measurements have been used to infer and compare the properties of the different polar materials. For example, Thomas and Weitz compared the color of the dark material near NPLD scarps to material within NPLD layers and within the circumpolar sand sea [3]. Herkenhoff and Vasavada used Viking IR measurements to determine the nature of the dune-forming material and its relationship to other dark, dune-forming materials at lower latitudes [4]. However, such investigations have been limited by the relatively low spatial resolution of Vi-

king color imagery and IR data compared to the spatial dimensions of layers, troughs, scarps, and dune fields. We hope to take advantage of the unprecedented spatial resolution of Mars Odyssey Thermal Emission Imaging System (THEMIS) visible and IR imagery in order to make these inferences and comparisons with the highest possible accuracy (e.g., Figure 1).

**THEMIS Observations:** To address this science goal, we defined a number of Regions of Interest (ROI) for THEMIS to target (Figure 2) as part of the Mars Odyssey Participating Scientist program. We gratefully acknowledge the THEMIS science team and operations staff for acquiring ~100 visible and IR image cubes during Mars' northern summer ( $L_s$  110-160) as orbit tracks intersected our ROIs. The visible image cubes in our data set have five wavelength bands, along-track lengths of ~1000 pixels, and a spatial resolution of 19-38 m/pixel. The IR image cubes have ten wavelength bands and a spatial resolution of 100 m/pixel. The along-track footprint of the IR cubes often begins < 80° latitude, crosses the pole, and terminates < 80° latitude.

**Planned Analysis:** We will utilize these THEMIS data in order to understand the morphology and color/thermal properties of the NPLD and related materials over relevant (i.e., small) spatial scales. A first step will be to assemble color mosaics of our ROIs in order to map the distribution of ices, the different layered units, dark material, and underlying basement. The color information from THEMIS is crucial for distinguishing these different units (Figure 1), which are less distinct on Mars Orbiter Camera images.

We wish to understand the nature of the marginal scarps and their relationship to the dark material. Co-registered Mars Orbiter Laser Altimeter (MOLA) data will provide a measure of scarp morphologies and may help identify the process(es) eroding the NPLD (e.g., mass wasting, wind, sublimation). The dark material is present in continuous sheets at the feet of many scarps, but does not express dune bedforms there. However, dark material has barchan-type formations when present tens of kilometers away from the scarps [3]. MOLA will help identify the relationship between the spatial distribution of dark material, the presence of bedforms, and the influence of topography.

A more ambitious goal (probably beyond the time-frame of the 6<sup>th</sup> Mars Conference) is to derive the thermophysical properties of the different geologic materials using THEMIS and Mars Global Surveyor Thermal Emission Spectrometer (TES) data. Such analyses are complicated by the need for atmospheric correction (of both radiatively active CO<sub>2</sub> and dust) and accurate, representative surface temperatures. The latter may be compromised by the footprint size (compared to the areal extent of the material of interest), the influence of topography, and the absolute calibration of the measurement. However, the THEMIS data offer the promise of extending our previous analyses [4] to finer spatial scales and effort will be made to overcome these challenges. In order to derive thermal inertias and thermally derived albedos, we will employ a 1-D, radiative-convective thermal model of Mars surface, subsurface and atmosphere. The model will use simultaneous (or seasonally relevant) TES atmospheric dust opacities, and where possible, include the effects of surface slopes on insolation using MOLA topographic data.

**References:** [1] Murray, B. C. et al. (1972) *Icarus*, 17, 328. [2] Cutts, J. A. (1973) *J. Geophys. Res.*, 78, 4231. [3] Thomas, P. C. and Weitz C. (1989) *Icarus*, 81, 185. [4] Herkenhoff, K. E. and Vasavada A. R. (1999) *J. Geophys. Res.*, 104, 16,487. [5] Malin, M. C. and Edgett, K. S. (2001) *J. Geophys. Res.*, 106, 23,429. [6] Byrne, S. and Murray, B. C. (2002) *J. Geophys. Res.*, 107, 11-1.

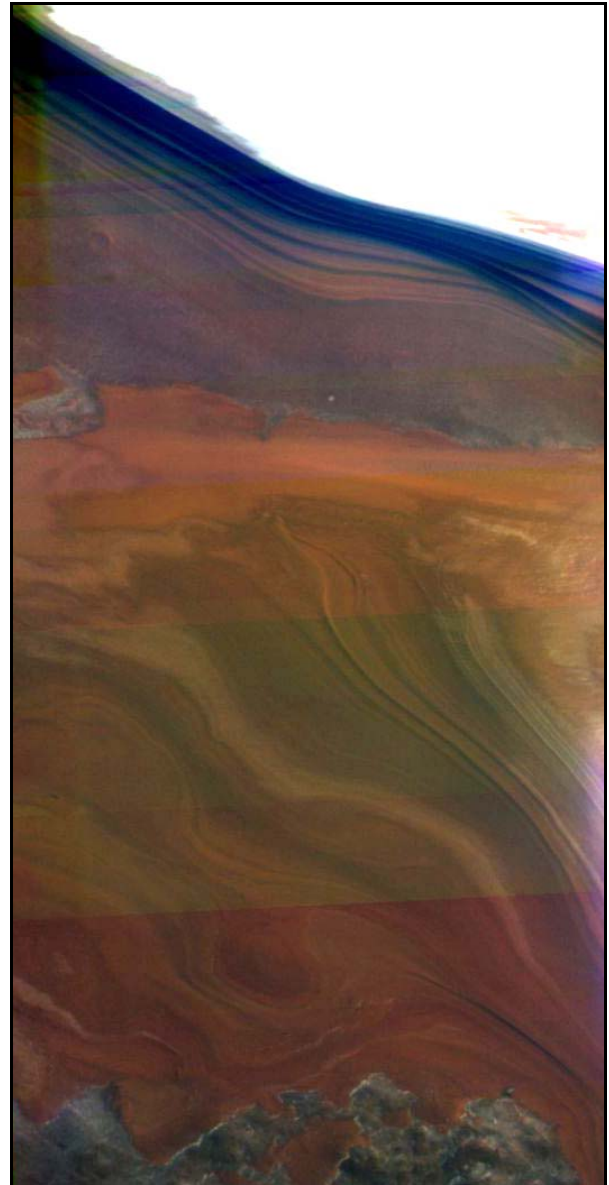


**Figure 1.** Color composite of THEMIS visible image data showing the north polar residual ice cap (top) and layered materials near the margin of the NPLD. Here the erosion of the deposits appears to “bottom out”, exposing the basement terrain underneath the NPLD (best seen along the lower edge of the image). The color information greatly aids this interpretation.

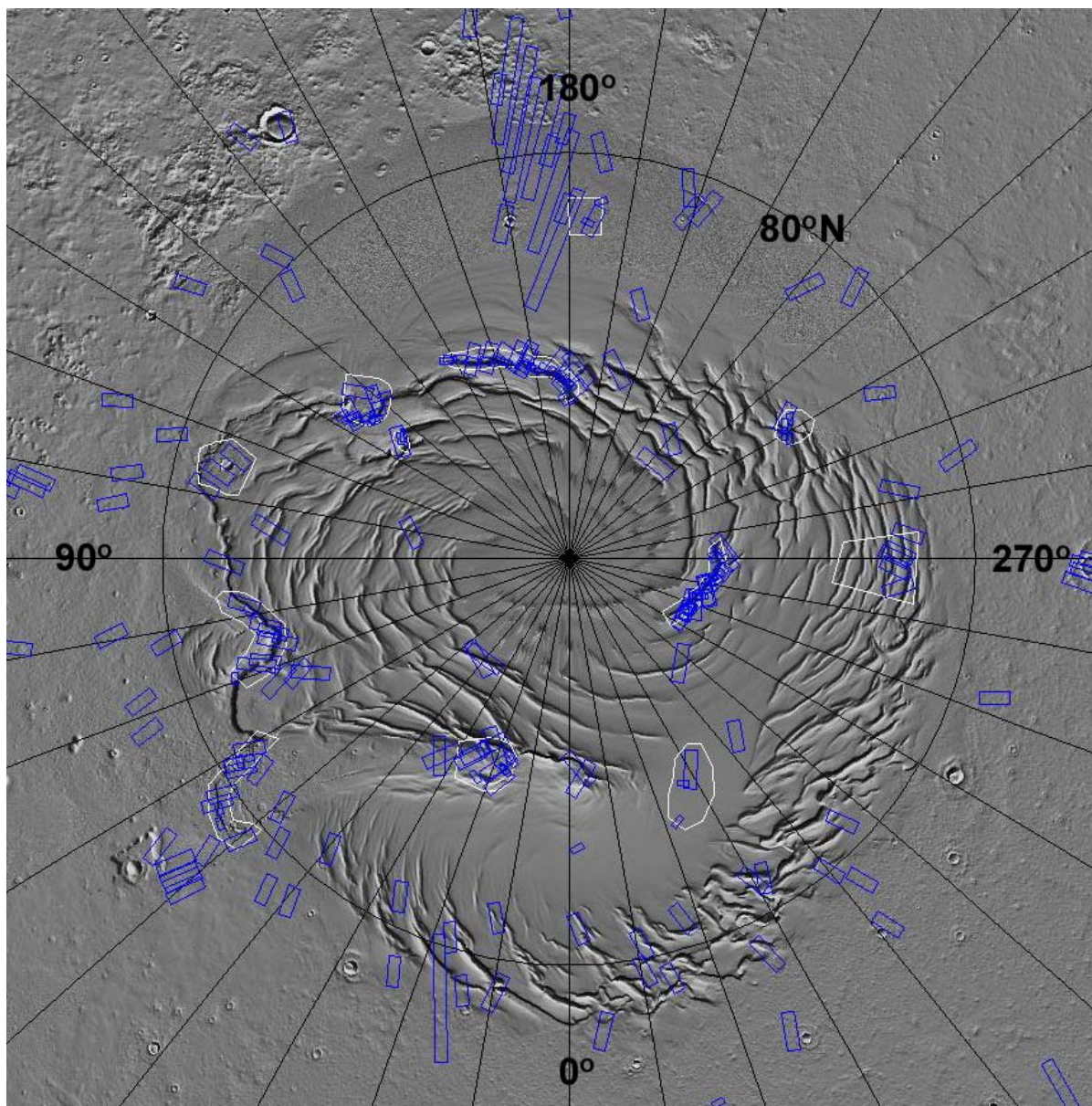


**Figure 2.** Map of Mars' north polar region showing the locations of our THEMIS ROIs (white outlines) and all acquired THEMIS visible image cubes (blue footprints). Our ROIs include arcuate scaps near the margin of the NPLD, the head of Chasma Borealis, and well-developed trough systems within the NPLD. The basemap is a shaded relief representation of Mars Orbiter Laser Altimeter data. Longitudes are West.

**AUTOMATED ANALYSIS OF MARS MULTISPECTRAL OBSERVATIONS.** K. Wagstaff, *Applied Physics Laboratory, Johns Hopkins University, Laurel MD 20723, USA, (kiri.wagstaff@jhuapl.edu)*, J. F. Bell III, *Department of Astronomy, Cornell University, Ithaca NY 14853, USA, (jfb8@cornell.edu)*.

Multispectral and hyperspectral imagers are now commonly used to obtain remote sensing measurements for the study of Mars, and many more such measurements are planned for the future. These techniques present a number of data collection, processing, and analysis challenges for planetary scientists. For example, CRISM, the spectrometer that will fly on Mars Reconnaissance Orbiter in 2005, is expected to return about 9 terabytes of data over the mission duration. Each multispectral map will be 5120x5120 pixels in size (25 MB). It is not obvious how to easily browse this data, much less perform detailed analyses of it. More data means more information and the opportunity for new insights about Mars, but it carries with it a heavier and heavier burden for the analysis process.

Conventional methods for analyzing multispectral data include techniques such as examining absorption band depths at specific wavelengths or plotting two-dimensional histograms of radiance at different wavelengths. Selecting wavelengths and band depths that will yield the most compositional or mineralogical insight requires a significant amount of expertise about the object being observed. More critically, the process can be very time-consuming, with each histogram providing a single two-dimensional slice of the data for interpretation. For spectral data with only 10 wavelengths, there are 900 such histograms. Instruments such as the HST Space Telescope Imaging Spectrograph (STIS) have observed Mars at 1024 wavelengths; there are 1,047,552 corresponding possible histograms. This is not an upper limit, however; there are several other histograms that can provide insights, such as plotting radiance at one wavelength against the radiance ratio at two other wavelengths, or plotting radiance against a band depth or slope feature.

Of course, not every pair of features will yield interesting results when plotted against each other. Often areas of interest are already known, such as the 900 nm band depth or the radiance at 440 or 750 nm for Mars observations. However, our knowledge of Mars is certainly not comprehensive. The ability to discover additional informative relationships is critical.

In this abstract, we describe the result of applying an automated clustering algorithm to two data sets composed of Mars observations. One data set was collected by STIS on the Hubble Space Telescope; the other was obtained by the Mars Pathfinder Lander. We find that the results are comprehensible and, when a manual analysis is available for comparison, there is a good amount of agreement between the two sets of results. The automated analysis, however, requires significantly less time to produce results.

**Hubble Space Telescope STIS Data.** We first introduce the STIS data set. These observations were collected by a spectrograph on HST at several different wavelengths (Bell III et al., 2001). The observing period was from April to May of 1999, corresponding to the middle of northern summer on Mars. Consequently, the quality of the observations of the northern part of the planet is high, while the southern latitudes have poorer coverage. Each map is composed of  $360 \times 180$

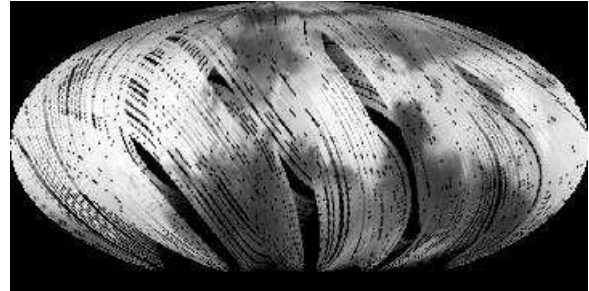


Figure 1: Global map of Mars, observed at 907 nm from Earth orbit by an imaging spectrograph on the Hubble Space Telescope. The image is in a Mollweide equal-area map projection.

pixels; the goal is to partition the pixels into coherent regional clusters on Mars. Figure 1 shows all of the pixels at a specific wavelength, 907 nm. Brighter areas correspond to higher intensity. The black striping and missing data regions are artifacts of the scanning method used by the spectrograph. Excluding missing data and pixels that fall outside the map, each image is composed of 47,221 pixels. Each pixel is described by 26 features, corresponding to the pixel's intensity at each of 26 different wavelengths, 528–1016 nm, selected from the original 1024.

We applied the k-means clustering algorithm to this data. K-means (MacQueen, 1967) takes as input a data set and the number of desired clusters,  $k$ . It produces a partition of the data set into  $k$  clusters such that items inside a cluster are very similar and distinct from items in other clusters. Each cluster is represented by its mean, or centroid. For multispectral analysis, the center of a cluster is a spectrum composed of the mean values for each of the wavelengths.

Figure 2 shows the result of partitioning the STIS data into seven clusters. Most of the clusters vary only in their albedo; their general spectral shapes are similar. Two noteworthy exceptions are the green and grey clusters. The green cluster is

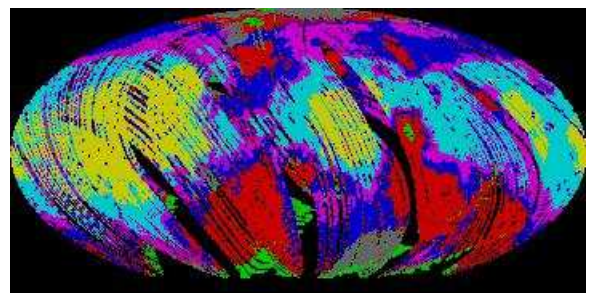


Figure 2: Results of k-means clustering with  $k = 7$ . Each color represents a spectral class that was determined by the algorithm to be spectrally unique. Many of the classes follow the classical albedo boundaries.

## AUTOMATED MULTISPECTRAL ANALYSIS OF MARS DATA: K. Wagstaff and J. F. Bell III

composed of very dark and flat spectra. It occurs in the southern regions of the data set, where observing conditions were poor (near the limb, and thus artificially darkened), near the north polar cap, and in an isolated spot that turns out to correspond to Syrtis Major. The southern regions can be considered an artifact of the data collection process. The north polar spots are likely to be dark soils and/or bedrock exposed by the retreat of the north polar cap, due to the time of year. Syrtis Major has been consistently identified as an unusually dark region on Mars; see e.g., McCord et al. (1971).

The other exceptional cluster is represented by grey in Figure 2. It occurs at the north pole and in a round region near the southern part of the planet. The average spectrum for this cluster is also unusually flat spectrum, but it differs from the green cluster in that it is much brighter (reflectance about 0.12 versus 0.08 for the green cluster). It does not exhibit the typical Martian spectral qualities of low blue and high red reflectance. We hypothesize that this cluster represents ice and/or clouds observed on the planet, and the physical location of the grey pixels bears this out. The north pole is a likely place to find ice, and the southern region corresponds directly to Hellas Crater, where thin clouds may form.

In both of these cases, the areas of interest highlighted by the analysis do not necessarily provide new knowledge about Mars. However, even at the coarse resolution provided by this data set, the results we obtain are consistent with previous knowledge about the planet. This provides support for using such methods on other Mars data sets, where less existing knowledge may be available.

**MPF Lander Data.** The Imager for the Mars Pathfinder Lander obtained a series of 12-color multispectral images during the lander's mission in 1997. A subset of these images, focusing primarily on soil deposits, has been analyzed by Bell et al. (2000) using manual and histogram-based classification methods. Figure 3 shows the 58 multispectral spot images at 600 nm. Bell et al. identified eight distinct soil and dust units: "Bright I-IV", "Surface dust", "Atmospheric dust", "Dark", and "Disturbed" (disturbed soil occurs in regions where the rover's wheels traveled). We also applied the k-means clustering algorithm to this data set, specifying eight clusters, as suggested by Bell et al. The resulting classification of the spot data is shown in Figure 4, where each cluster is represented by a different color. For the following discussion, we will refer to the k-means clusters by their color, and the clusters obtained by Bell et al. by the above descriptions.

The average cluster spectrum for each class is shown in Figure 5. They are color-coded to match the colors used in Figure 4. There are several interesting similarities to the clusters manually identified by Bell et al. The red and purple clusters correspond well to the "Dark" and "Disturbed" soil units. For both clusters,  $R_{750}$  is less than 0.2, matching the condition specified by Bell et al. The two soil types are distinguished in Bell et al.'s analysis by their  $R_{440}$  and 900 nm band depth values. "Dark" soil units have  $R_{440} > 0.035$ , while "Disturbed" soil has  $R_{440} < 0.035$ . We do not observe these exact values, but the 900 nm band depth for the red cluster is twice as large (0.06) as that for the purple cluster.

The orange cluster obtained by k-means corresponds well to the unit identified as atmospheric dust by Bell et al. In

both analyses, it occurs in sky areas of the spot images. In our results, it also occurs on the top of a rock (spot 16). It is characterized by a high blue reflectance and a low red/blue ratio (i.e., the spectrum is relatively flat compared to other areas). In our analysis, this cluster is also distinguished from the other clusters due to its negative band depth at 900 nm. Every other cluster has either a negligible or a positive band depth at this wavelength. We also found that our cluster covers 7% of the pixels, while the atmospheric dust identified by Bell et al. only covers 4%. We hypothesize that some "Bright III" units may be included in this cluster, as they are generally characterized by a negative 900 nm band depth.

The remaining clusters are all composed of relatively bright material. They probably correspond to a collection of the "Bright I", "Bright II", "Bright IV", and "Surface Dust" clusters. We have not yet matched them more closely with each type. The distinctions identified by Bell et al. between these types depend on the 800–1000 nm slope and the 900 nm absorption band depth. Calculating these values over the cluster representative spectra did not sufficiently distinguish them; for example, all of the calculated 800–1000 nm slopes were between  $-0.00011$  and  $-0.00010$ . We believe that calculating these values on individual spectra and then looking at the range of values for each cluster may yield more insight.

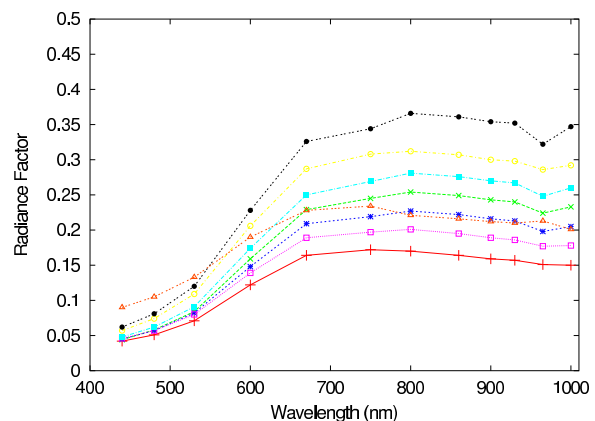


Figure 5: Average spectra for each of the eight clusters identified in Figure 4.

The analysis results we have obtained on this data set via an automated method are largely consistent to the results obtained by a manual analysis. This correspondence lends support to using automated methods to provide a "first pass" analysis of a data set.

**Conclusions.** Automated data analysis provide a means for handling the massive data volumes that planetary scientists increasingly face. By identifying distinct sub-groups in a data set, they highlight both overall trends and interesting exceptions. The speed of automated methods can save time devoted to preliminary investigations and make the analysis of terabyte-scale data sets feasible.

**References.** [1] Bell et al. (2000) JGR, 105, 1721–1755. [2] Bell et al. (2001) Bull. Am. Astro. Society, 33, 1127. [3] MacQueen (1967) Fifth Symp. on Math, Statistics, and Probability, 281–297. [4] McCord et al. (1971) Icarus, 14, 245–151.

## AUTOMATED MULTISPECTRAL ANALYSIS OF MARS DATA: K. Wagstaff and J. F. Bell III

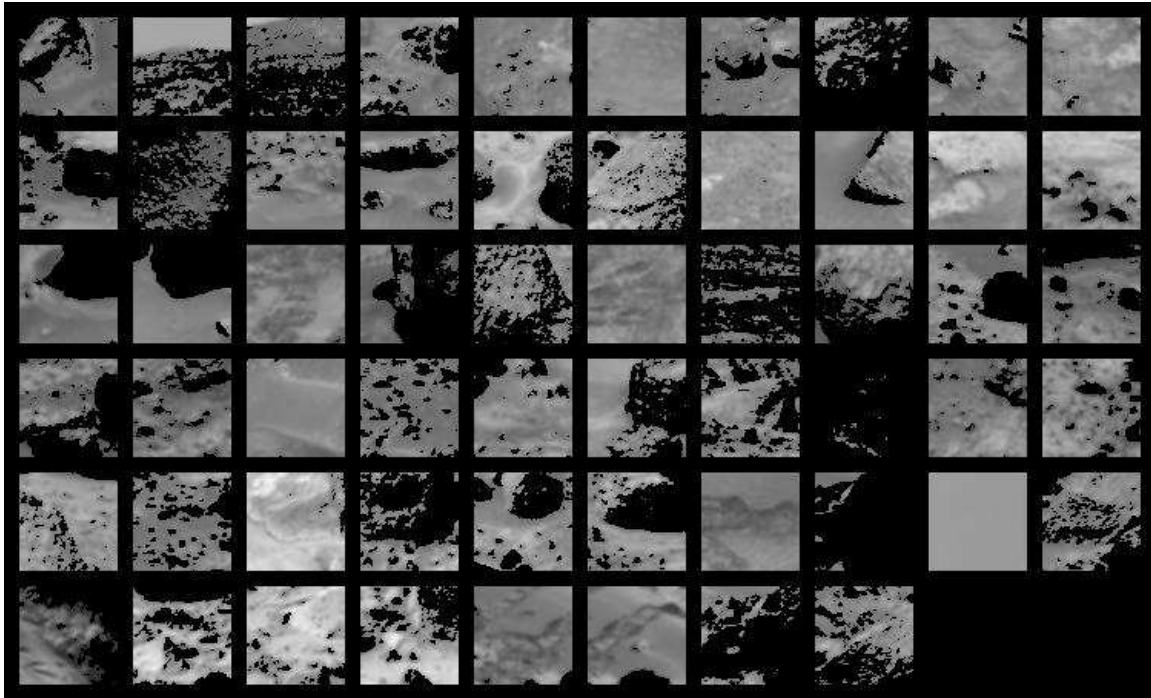


Figure 3: MSS soils and dust composite (combined left and right eye) mosaic of the 58 multispectral spots (each 64x64 pixels). The greyscale image shows intensity at 600 nm. Dark areas are regions where rocks, shade, and parts of the spacecraft have been masked out. Spots are numbered 1–58, starting at the top left and proceeding left to right.

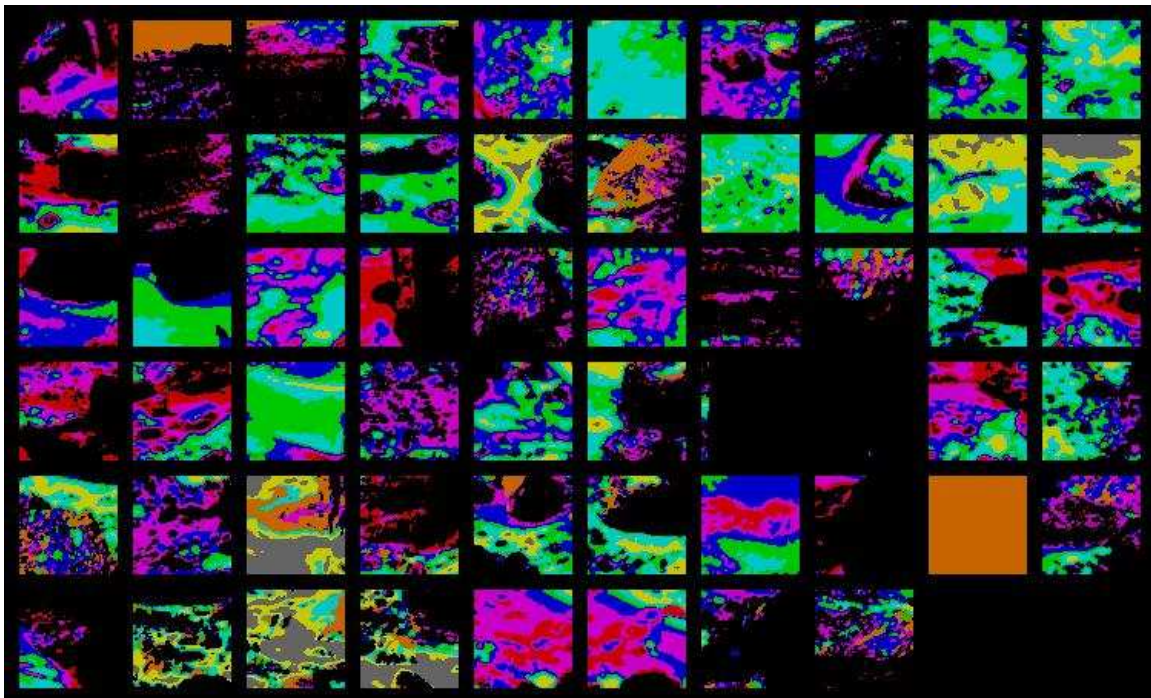


Figure 4: Automated classification of the MSS data into eight distinct spectral types.

INVESTIGATING SURFACE MINERALOGY, ALTERATION PROCESSES, AND BIOMARKERS ON MARS USING LASER RAMAN SPECTROSCOPY Alian Wang, B. L. Jolliff, and L. A. Haskin, Department of Earth and Planetary Sciences and the McDonnell Center for the Space Sciences, Washington University, Campus Box 1169, One Brookings Drive, St. Louis, MO 63130. <alianw@levee.wustl.edu>.

**Introduction:** In a surface investigation of Mars, a key priority should be definitive identification and characterization of surface materials (e.g., definitive mineralogy), which will improve our understanding of Mars' evolutionary history. As used here, "definitive" mineralogy includes mineral identification and determination of key mineral chemical compositions; however, it is also important to determine the relative proportions of different minerals in a rock or soil as well as textural relationships of mineral assemblages. Because we know the chemical and physical conditions under which individual minerals form, we learn about past martian environmental conditions from such detailed mineralogical information. The record of alteration in surface rocks is expected to reach back in time from relatively recent alteration of rock surfaces, to past stream and lake environments, to hydrothermal settings of the upper martian crust, and to the planet's early igneous chemical differentiation. An assessment of whether life might have formed on Mars requires a broad understanding of the nature of the planet, with an emphasis on the presence and role of water during its evolution. With better knowledge of past and present Mars' environments, we can speculate more rationally on the possible development of life on Mars.

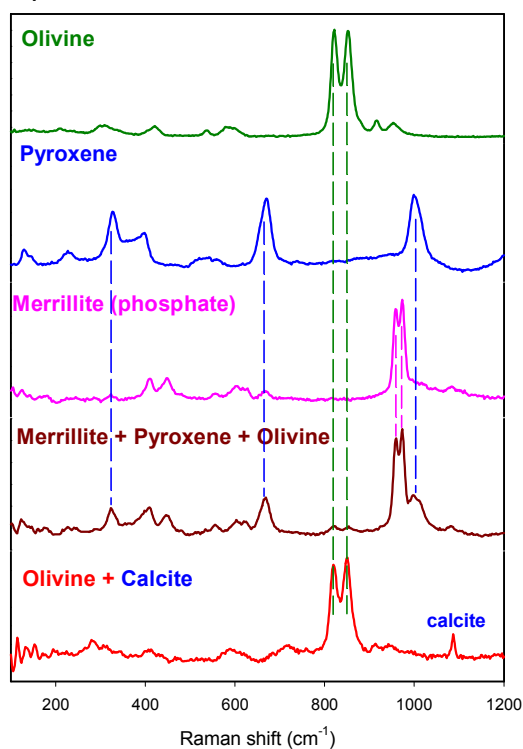
Despite a wealth of information from past and on-going missions to Mars, the capability to determine the mineralogy of surface materials and to connect mineralogy with lithologic characteristics that are diagnostic of the environment in which those materials formed remains inadequate. The 2003 Mars Exploration Rovers (MER) will carry a Mini-TES and a Mössbauer spectrometer, which will provide some detailed mineralogy information. For general characterization of minerals and/or biogenic phases (reduced carbon, PAHs, etc) on the surface of Mars, we have been developing a miniaturized laser Raman spectrometer for *in situ* analyses -- the Mars Microbeam Raman Spectrometer, MMRS [1]. We are also developing strategies to use Raman spectroscopy as a stand-alone technique and to be used synergistically with other *in situ* analysis methods in future planetary missions. Through studies of Martian meteorites and terrestrial analogs, we are gaining experience of what compositional and structural information can be obtained on key mineral groups using *in-situ* Raman measurements. We are developing methods for determining mineral proportions in rocks or soils and identifying rock types from sets of closely spaced, rapidly acquired spectra. We are studying how weathering and alteration affect the Raman and luminescence features of minerals and rocks,

and we are investigating the Raman characteristics of biogenic organisms and their remains. These studies form the scientific basis for *in-situ* planetary Raman spectroscopy, and they are being done in parallel with instrument development towards a flight version of the MMRS [1].

**Planetary Raman spectroscopy.** Laser Raman spectroscopy is well suited for on-surface mineralogical investigations of Mars for the following reasons:

1) It is definitive; i.e., minerals are unambiguously identified through their fingerprint spectra. Raman peaks are sharp and non-overlapping; straightforward identification of phases in a mixture can be achieved from raw spectra, spectral deconvolution in general is not required. Figure 1 shows five spectra taken from EETA79001, three single phase spectra (olivine, pyroxene, phosphate) and two mixture spectra in which the contributing phases are obvious.

Figure 1. Single-phase and multi-phase Raman spectra obtained from EETA79001 martian meteorite



2) Raman spectroscopy does not suffer from a "grain size effect." Raman peak positions and peak widths do not change even when the size of particles decreases to 1-2  $\mu\text{m}$ , although overall intensity may decrease because of scattering.

## Planetary Raman Spectroscopy: A. Wang, B. L. Jolliff, L. A. Haskin

3) Analyses are rapid, requiring only a few seconds to half a minute to obtain a spectrum.

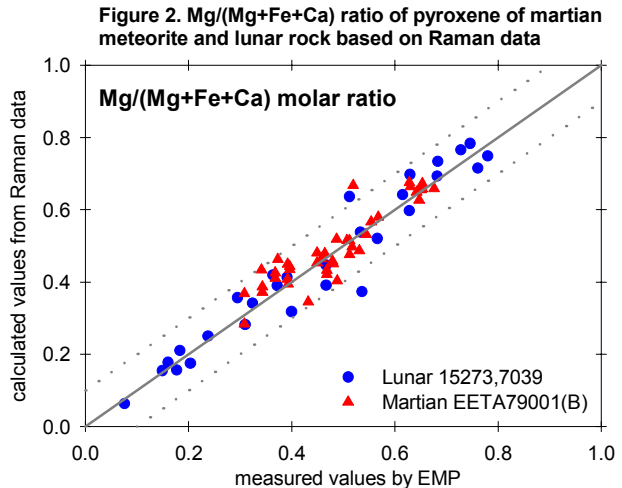
4) The analysis method requires no sample positioning, a Raman probe will send a laser beam towards sample surfaces (rock or soil), and will collect the backscattered radiation.

5) No sample preparation is required; original rough surfaces of rocks and soils give informative spectra. Freshly exposed surfaces, potentially available if the rover carries a rock abrader, are best for studying original rock mineralogy, but rock coatings are important to determining environmental effects [2].

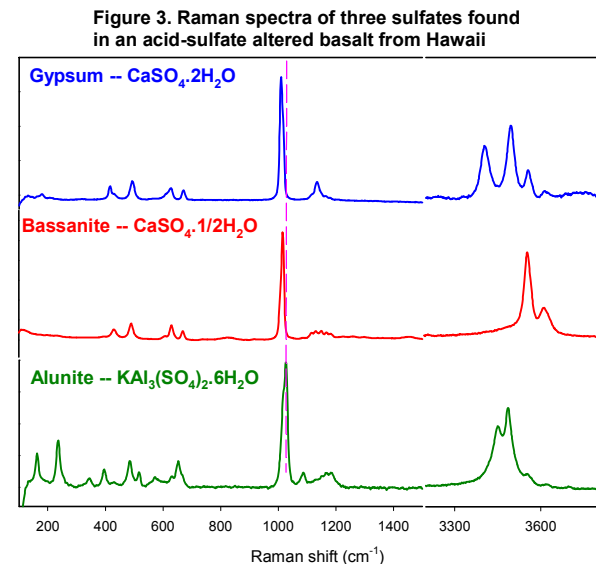
6) It provides approximate minerals modes, rock identification, and information on grain size and rock texture through our Raman “point-counting” procedure, [3, 4]. Broader-beam techniques integrate over major, minor, and trace minerals in a sampling area such that less abundant phases may not be definitively identified because the spectrum is dominated by the major phases. Minor and trace phases register strongly with the microbeam Raman technique when they fall within the small sampling area (10-30  $\mu\text{m}$ ) activated by the laser beam. Alteration minerals that occur in cracks and vesicles would likely be detected and identified within the linear scan ( $\sim 1$  cm) by the Raman probe (e.g., [5]). The spatial relationships within mineral assemblages are obtained in the same way; sets of juxtaposed minerals that form together at various locations within a rock can be key to discovering possible biologically mediated formation of a mineral or mineral assemblage.

In the following paragraphs, we describe examples of results from our planetary Raman spectroscopic studies that demonstrate the usefulness of this technique and the potential of the MMRS for future missions.

**Silicate mineralogy.** Raman spectroscopy provides straightforward identification of silicates, including ortho-, chain-, double-chain-, ring-, layer-, and framework-silicates [6]. The differences in degree of polymerization of the major silicate groups provide distinct and systematic variations in their Raman spectral patterns. Furthermore, Raman peak positions of some mafic silicate minerals provide information on cation ratios, e.g., Mg/(Mg+Fe) in olivine [7] and Mg/(Mg+Fe+Ca) in pyroxene [8], which relate directly to rock genesis. Figure 2 compares Mg/(Mg+Fe+Ca) ratios in pyroxene derived from Raman data and those analyzed by electron probe microanalysis. Based on the compositional distribution of pyroxene (and olivine) in a rock, we obtain insight on the cooling rates of parent magmas and the crystallization of that rock. The Mg/(Mg+Fe) variations in olivine and pyroxene grains along a Raman point-count traverse reveal three generations of olivine during the formation of EETA79001 martian meteorite.



**Carbonates, sulfates, phosphates.** Raman spectroscopy provides excellent sensitivity for oxyanionic minerals, e.g., carbonates, sulfates, and phosphates (e.g., [9]). The strong covalent bonding in  $\text{CO}_3$ ,  $\text{SO}_4$ , and  $\text{PO}_4$  groups provide characteristic strong and narrow Raman peaks, which are readily detected even in mixtures and at low concentrations. Major cation variations (e.g., Mg, Fe, Ca) can be determined from well resolved peak positions. Figure 3 shows Raman spectra of three sulfates found in a Hawaiian acid-sulfate altered basalt; peaks from the  $\text{H}_2\text{O}$  vibration occur in the 3200–3800  $\text{cm}^{-1}$  region.



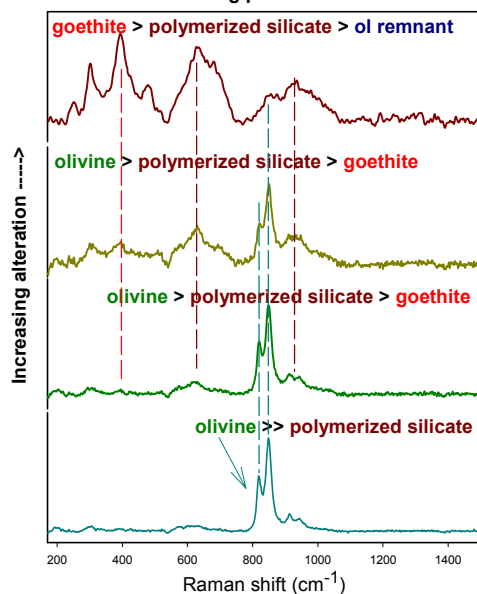
**Oxides and oxyhydroxides** -- Fe-oxides and oxyhydroxides have modest covalent character, and thus are relatively weak Raman scatterers. Chromite, magnetite-ulvöspinel, ilmenite-hematite and their solid solutions are, nevertheless, well characterized by the spectral patterns and positions of their major and minor Raman peaks, so they can be distinguished even based on spectra with low S/N. In some cases such as in the

## Planetary Raman Spectroscopy: A. Wang, B. L. Jolliff, L. A. Haskin

chromite series, major cation ratios can be determined from variations in Raman spectra [10, 11].

**Alteration mineralogy.** In addition to the main rock-forming minerals, phases formed at different stages of alteration and information about their degree of structural order can be identified. We have studied a basalt cobble from Lunar Crater Volcanic Field, NV, in which olivine grains altered to iddingsite along their edges and fractures [12]. The structure of altered olivine affects its Raman peak positions and peak widths, so it can be distinguished from unaltered phenocrystic olivine. A more polymerized structure (between chain and phyllosilicate) was formed where alteration was more intense. Goethite and hematite were identified among the products of alteration. Figure 4 shows phase variations in the alteration zone.

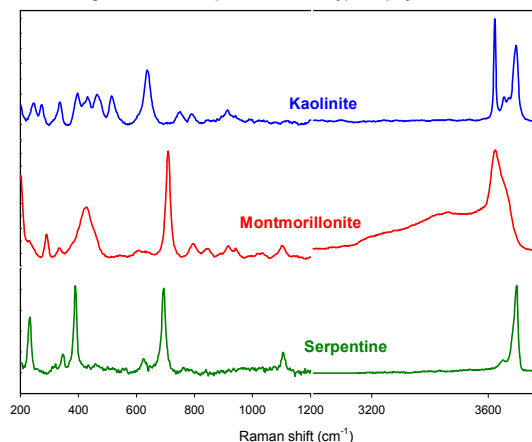
Figure 4. Raman Spectra taken in linear traverse showing phase variations



**Mineralogical and other forms of H<sub>2</sub>O.** Water of all forms, ice, liquid, gaseous, bound (OH), clathrate, and unbound (H<sub>2</sub>O) in minerals have characteristic Raman features. The Raman spectral features of hydrous phyllosilicates provide a way to distinguish their structures (di-octahedral or tri-octahedral), chemistries (Mg, Fe, Al-bearing), local site symmetry, and the types and number of crystallographically equivalent sites around OH groups [13]. Figure 5 shows Raman spectra of two di-octahedral clay minerals (kaolinite & montmorillonite) and a tri-octahedral phyllosilicate (serpentine).

**Organic materials.** Graphitic carbon and organic C-C, C-H, C-O, C-N, bonds are strong Raman scatterers. We detected reduced carbon in a 3.35 Ga chert from South Africa (Fig. 6) to a level of  $\leq 50$  ppm using the MMRS brassboard [8]. In a study of a weathered basalt cobble, we encountered a crustose lichen in a

Figure 5. Raman spectra of three typical phyllosilicates



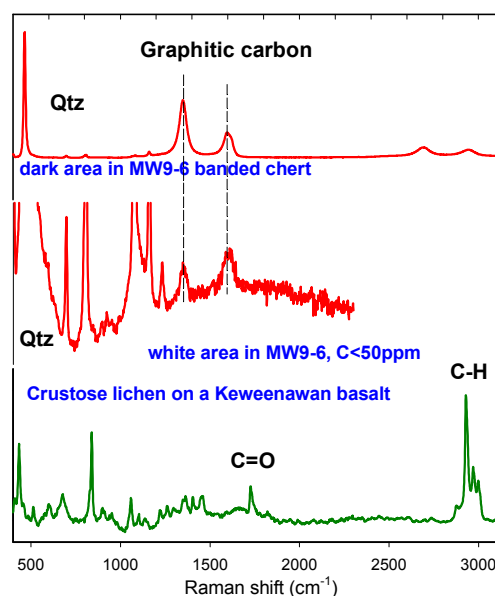
Raman point-count traverse, and its protective wax coating yielded strong Raman peaks.

Laser Raman spectroscopy for planetary surface analysis has some limitations, as follows:

Raman spectroscopy is not well suited to detect strongly ionic minerals such as halite. Simple salts with more covalent character, however, give useful spectra, e.g., fluorite, CaF<sub>2</sub>.

Glassy materials yield relatively broad and weak spectra, and the extraction of signals for glass beneath the spectral peaks of crystalline phases is difficult. Nonetheless, basaltic glass and silica-rich glass are easily observed and can be distinguished in spectra of low background.

Figure 6. Raman spectra of reduced carbon and a crustose lichen



Some materials photoluminesce to the extent that mineral spectral features are obscured. On the other hand, intense photoluminescence carries valuable information; for example, it is commonly associated with organic matter in terrestrial materials. Inorganic photo-

## Planetary Raman Spectroscopy: A. Wang, B. L. Jolliff, L. A. Haskin

luminescence seldom prevents mineral identification, and provides additional information on mineral compositions, such as the existence of rare-earth elements and  $Mn^{2+}$ .

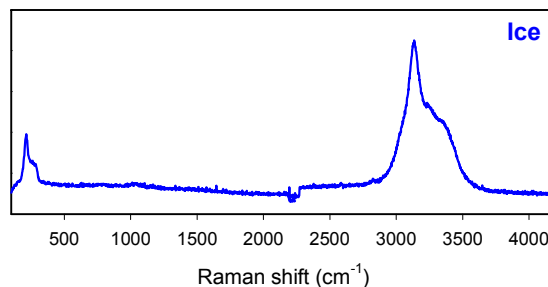
**Current development status of the MMRS.** The Mars Microbeam Raman Spectrometer (MMRS) was designed to achieve the desired scientific performance as described in above section, and was described in detail by [1]). The MMRS has three major parts: a Raman probe, a miniaturized spectrograph, and electronics (including the laser). The mass of the MMRS is ~2.6 kg. Operationally, the Raman probe will be positioned against the target by a robotic arm of a rover or a lander or fixed in place and samples delivered to it. A set of 50–100 spectra will be taken along a ~1 cm traverse on the target during a 1-4 hour period. Total energy usage is estimated to be ~35 Whrs per 100 spectra.

The current status of the MMRS is that an advanced brassboard (ADBB) of MMRS is accomplished this year [13]. The probe and spectrograph have been redesigned with improved optics, and the electronics have been miniaturized. The CCD detector is now cooled thermoelectrically in anticipation of eventual terrestrial field testing of the instrument. Based on measurements on a set of standard common minerals (quartz, feldspar, olivine, pyroxene and calcite), the ADBB has a detection sensitivity ~40% that of our state-of-the-art laboratory Raman system, thus twice that of the previous MMRS brassboard. The ADBB has an improved spectral resolution, and still maintains the required spectral range ( $207\text{--}4325\text{ cm}^{-1}$ ), which to covers the fundamental vibrational bands of minerals, OH,  $H_2O$ , and organic species. The ADBB also has an improved Raman-to-photoluminescence S/N ratio, and an improved depth of sampling field. Target surfaces are likely to be rough and uneven in the field; the design of the MMRS nevertheless eschews automatic focusing for the sake of system simplicity. To compensate, the probe has a substantial depth of sampling field (DSF).—The DSF of ADBB is >12 mm for a colorless calcite and a light green olivine, and ~2 mm for a very dark pyroxene.

A whole-system cold performance test at  $-24^\circ\text{C}$  was conducted for the ADBB system at the National Ice Core Laboratory, Denver. Raman spectra of ice and mineral grains embedded in ice were obtained (Fig. 7).

**Acknowledgements:** Support of this work comes from NASA grants NAG5-7140, NAG5-10703 and NAG5-12684 (blj), internal support from JPL and Washington University.

Figure 7. Raw spectrum obtained at  $-24^\circ\text{C}$  from ice core



#### References:

- [1] Wang A., et al. (2003a) Development of the Mars microbeam Raman spectrometer (MMRS), *JGR 108*, 5-1–5-18.
- [2] Israel E., et al. (1997) Laser Raman spectroscopy of varnished basalt and implications for in-situ measurements of Martian rocks. *JGR 102*, 28,705–28,716.
- [3] Haskin L.A., et al. (1997) Raman spectroscopy for mineral identification and quantification for in-situ planetary surface analysis: A point count method, *JGR 102*, 19,293–19,306.
- [4] Wang A., Jolliff B.L., and Haskin L.A. (1999a) Raman spectroscopic characterization of a highly weathered basalt: Igneous mineralogy, alteration products, and a micro-organism *JGR 104*, 27,067–27,077.
- [5] Wang A., Jolliff B.L., and Haskin L.A. (1999b) Raman spectroscopic characterization of the martian SNC meteorite Zagami *JGR 104*, 8509–8519.
- [6] Wang A., et al. (1994) A database of standard Raman spectra of mineral and related inorganic crystals. *Appl. Spectrosc.* 48, 959–968.
- [7] Wang A., et al. (2000) Mineral features of EETA79001 martian meteorite revealed by point-counting Raman measurements as anticipated for in-situ exploration on planetary surfaces. *LPS XXXI*, Abstract #1887.
- [8] Wang A. et al. (2001) Characterization and comparison of structural and compositional features of planetary quadrilateral pyroxenes by Raman spectroscopy. *Amer. Mineral.* 86, 790–806.
- [9] Kuebler K. et al. (2001) Can we detect carbonate and sulfate minerals on the surface of Mars by Raman spectroscopy? *LPS XXXII*, Abstract # 1889.
- [10] Wang A. et al. (2003b) Fe-Ti-Cr oxide in martian meteorite EETA79001 studied by point-counting procedure using Raman spectroscopy. *LPS XXXIV*, Abstract #1742.
- [11] Malezieux J.M. & Birious B. (1988) *Bull. Mineralogical* 111, 649–669.
- [12] Kuebler K. et al. (2003) A study of olivine alteration to iddingsite using Raman spectroscopy. *LPS XXXIV*, Abstract #1953.
- [13] Wang A. et al. (2002) Raman spectroscopic characterization of phyllosilicate. *LPS XXXIII*, Abstract #1374.
- [14] Haskin L.A. and Wang A. (2003) *LPS XXXIV*, Abstract #1651.

**Evaluating putative shorelines adjacent to the dichotomy boundary near Arabia Terra.** Valerie E. Webb<sup>1</sup> and George E. McGill<sup>1</sup>,<sup>1</sup>Department of Geosciences, University of Massachusetts Amherst, 01003. vwebb@geo.umass.edu.

**Introduction:** In 1989, Parker *et al.* [1] identified two geologic contacts, Contact #1 and Contact #2, which they believed demarcated two distinct highstands of a global ocean ponded within the northern lowlands. Since then, Clifford and Parker [2] presented new nomenclature for Contact #1 and Contact #2, now known as the Arabia and Deuteronilus trends, respectively. To date, a total of nine putative shorelines have been identified by Parker *et al.*, [1, 2, 3], who categorized both global and regional scale trends. Our ~400,000 km<sup>2</sup> study area (Fig. 1) is just north of Arabia Terra, contiguous to the dichotomy boundary and centered on Cydonia Mensae. It is significant in further testing the shoreline hypothesis because it contains both the global scale trends Arabia and Deuteronilus, along with a regional trend known as Acidalia [2].

Further significance in our study arises from the fact that most previously published work [1,2,3,4] on the northern ocean's shorelines has been executed at much too low a resolution to provide quantitatively meaningful data. Our large-scale, relatively high-resolution study thus allows for a coherent dataset with which we can then use to test formation and post-formation shoreline models. Our analyses were aided by the interpretation of all available datasets, including Viking, MGS and Mars Odyssey datasets.

Recently, we rejected a shoreline interpretation for the Acidalia trend [5], due to the absence of evident erosion and the lack of its conformity to an equipotential surface. Our current results are in agreement with these earlier conclusions. Thus, this study will focus primarily on the Arabia and Acidalia trends.

Here, we provide new evidence supporting a shoreline interpretation for the Arabia and Deuteronilus trends. In the case of Arabia, we present a new site for the trend near the Bamberg crater area (Fig. 2). This newly adapted locality greatly strengthens the trend's approximation to an equipotential surface, with a mean elevation of -3700m and a mean deviation of  $\pm 13$ m. We also conclude that the Deuteronilus trend appears to represent two distinct, regional shorelines, with mean elevations of -4200m and -4000m. Analysis of THEMIS imagery further strengthens the case for a shoreline interpretation of these trends (Fig. 3).

**Methods:** We began our analysis by first interpolating nine topographic grids of key areas within our study area (Figure 1). Each DEM was

gridded at 231 m/pixel from a shapefile of MOLA Precision Experiment Data Record (PEDR) profiles downloaded from National Space Science Data Center's CD-ROM Catalog. The purpose of gridding our own data was two-fold: 1) we wanted to insure higher horizontal resolution and accuracy than is currently available from the Planetary Data System (PDS) imaging team's gridded 460 m/pixel model, and 2) we needed high-resolution DEM's to georeference (or align in spatial coordinates) Parker's unpublished MDIM's with the location of his shorelines. Higher horizontal resolution of the DEM corresponds to higher accuracy in the georeferencing of Viking and MGS datasets. Since the along-track shot spacing is ~300 m [6], and the across-track shot spacing within our area averaged ~200 m for the entire study area, but varied from less than 100 m to over 6 km, we feel that a pixel size of 231 m was a modest interpolation pixel size.

Next, we were able to georeference the two datasets together into the MGS coordinate system. Using Arc GIS 8.2 (a computing platform using both Arc Info and Arc View), we defined control points on both datasets and performed a polynomial transformation on the Viking MDIM's. The georeferenced dataset integrated the raw MOLA PEDR profiles, the gridded DEM, and Parker's Viking MDIM's (with the plotted shorelines) and projected them all into the same coordinate space.

The resultant dataset allowed us to determine where an individual MOLA profile crosses a plotted shoreline. We tabulated the elevations of each of these crossings based on the raw MOLA data. If a shoreline did not directly fall within a MOLA shotpoint, an inverse distance weighted relationship was used to calculate the elevation of each tabulated crossing. Thus, the vertical accuracy of the elevations used in this study are dependent on two factors: The resolution of the raw MOLA data, as explained above and in Smith, *et al.* [6]; and the weighted distance between the closest shot points and the measurement, which inherently varies from negligible to 150 m (half-way between two shot points).

More than 3000 observed crossings of the putative shorelines with MOLA profiles were used in this study to evaluate the topographic expressions of the shoreline trends.

**Discussion and Results:** From our analyses, we found that the Arabia trend is a close approximation to an equipotential surface. The only

substantial deviation from elevation constancy is near the Bamberg crater area (Fig. 1). If the crater impacted after the shoreline was in place, it would necessarily obliterate any evidence of its trend, and a shoreline could not be mapped in the area of its ejecta. If the crater formed before the shoreline, then the trend seen in Figure 1 is still most probably not a shoreline, due to the lack of its topographic expression.

However, our alternate hypothesis is that the shoreline continues north of the one originally mapped by Parker. Figure 2 shows our newly proposed location of the Arabia shoreline, trending north of Bamberg crater. This new portion of the trend follows an elevation contour consistent with the rest of the shoreline. We suggest that if this newly proposed trend is a shoreline then it is younger than the bolide event. However, it is important to note that high resolution Viking imagery within this area is rare, and evidence for coastal erosion along this newly proposed trend is still needed. We are currently awaiting new THEMIS imagery in order to shed new light on this issue.

If we shift the contact north, then the Arabia trend in its entirety conforms to an equipotential surface, with a mean elevation of  $-3707$  m and a mean deviation of  $\pm 13$  m. This contact is the oldest of all three originally mapped trends [2]. Its equivalence to an elevation contour within the entire study area suggests that little modification has occurred since the time of its formation.

Also, here we provide new evidence for the Arabia trend near Mawrth Vallis through the analysis of THEMIS imagery. Figure 3 yields a spatial correlation between an apparent geologic contact and the Arabia trend. In the THEMIS IR image, a brightness contrast exists between the material above and below the contact. This apparent contrast is separate from that of slope effect. Further, the material below the shoreline is clearly smoother than the material above it. The two portions of the visible THEMIS images within this area yield a potential coastal geomorphic contact that is concurrent with the location of the original Arabia trend. Since these observed contacts follow a single elevation contour, these observations are in agreement with a shoreline interpretation for the Arabia trend.

The Deuteronilus trend (see Figure 1) is the contact that Head *et al.*, [4] found to be closest to an equipotential surface. Our results are in agreement with their conclusions except that we find the observed elevations of this trend appear to be bimodal, with two clusters of data at  $-4000$  m and  $-4200$  m. These two groups appear to represent two distinct regional shorelines, as the originally mapped shoreline is not a

single equipotential surface. Since local deformation would necessarily disrupt the nearby, older Arabia trend along with the Deuteronilus trend, which runs just south of it, we have ruled out major post-formation modification as a responsible agent for the bimodality of the data. Topographic analysis further supports this conclusion, since there is no systematic variation in the along-trend profile, as would be present if tectonics disrupted a single, equipotential surface.

**Conclusions:** Shoreline recognition and evidence of coastal erosion provide valuable support for the past existence of a global ocean within the northern lowlands. Since 1989 [1], the validity of shorelines on Mars has been part of a highly controversial hypothesis regarding the hydrologic and geomorphic development of the northern plains [7, 8, 9, 10]. More high resolution, large scale studies must be executed in order to shed new light on this topic.

Here, we provide new data supporting a shoreline interpretation for the originally mapped Deuteronilus trend through the analysis of all available datasets. We also present an adapted locality for a small portion of the Arabia trend, strengthening its conformity to an equipotential surface. Further work is needed to determine if more than one flooding event occurred or if all of the presented regional shorelines represent multiple highstands of a single regressive body of water. Within our study area, our results support the first of these two scenarios, as age constraints and evidence of erosion upon the individual trends suggests, but either two settings are possible as potential resurfacing agents of the northern lowlands.

**References:** [1] Parker, T.J., *et al.* (1989) *Icarus*, 82, 111–145. [2] Clifford, S. M. and T.J. Parker (2001) *Icarus*, 154, 40–79. [3] Parker, T.J., *et al.* (1993) *JGR*, 98, 11061–11078. [4] Head, J. W., *et al.* (1999) *Science*, 286, 2,134–2,137. [5] Webb, V.E. and G.E. McGill, (2003) LPSC XXXIV Abst. #1132. [6] Smith, D.E., *et al.* (2001) *JGR*, 106, 23,689–23,722. [7] Malin, M.C., and K.S. Edgett (1999) *GRL*, 26, 3049–3052. [8] Rice, J.W. (2000) LPSC XXX 2006–2007. #8] Withers, P. and G.A. Neumann (2001) *Nature*, 410, 651. [9] Buczkowski, D.L. and G.E. McGill (2002) *GRL*, 29, 10.1029/2001GL014100. [10] Carr, M.H. and J.W. Head (2002) AGU, 83(47), Fall Meet. Suppl. Abst. #P51B-0357.

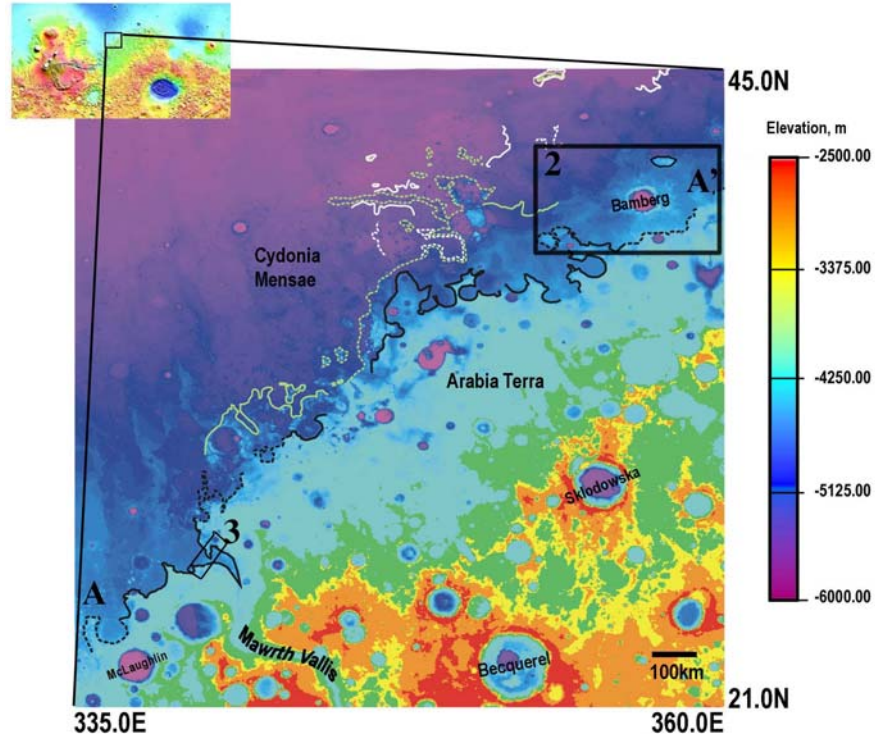


Figure 1: Location of Parker’s putative shorelines plotted on 1/128deg per pixel gridded topography as provided by the PDS imaging team’s MOLA Experiment Gridded Data Record (EGDR). Deuteronilus shown in green, Acidalia in white, and Arabia in black. Simple Cylindrical projection.

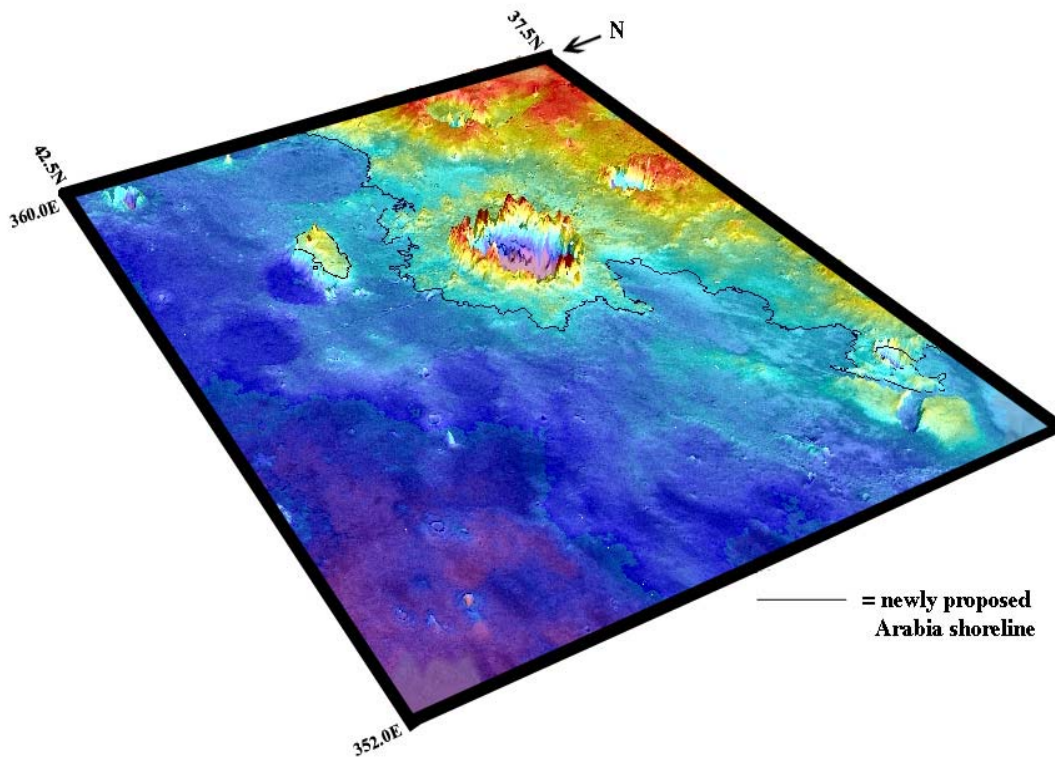
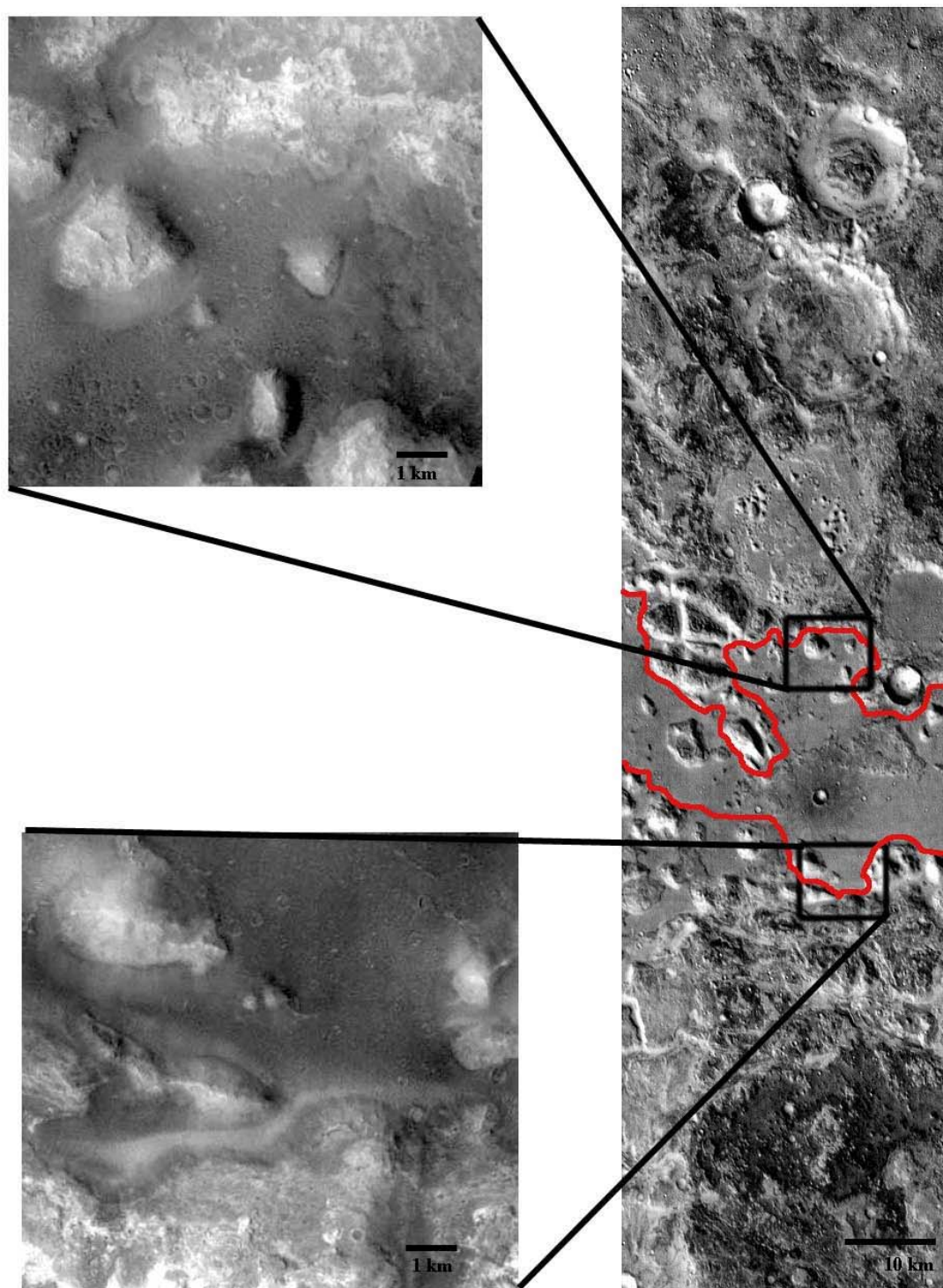


Figure 2: Newly proposed Arabia shoreline plotted on 3D perspective DEM looking southeast, gridded at 231 m/pixel. Vertical Exaggeration is ~ x20. The mean elevation of the profile shown is  $-3700\text{m} \pm 2\text{ m}$ .



**Figure 3: Evidence of coastal erosion near Mawrth Vallis. Daytime THEMIS IR image #I01561006 is on the right, with two insets from the visible THEMIS image #V01561007 on the left. The Arabia trend is shown in red. Center latitude/longitude of I01561006 is 24.955N and 340.326E, see Figure 1 for context.**

**POTASSIUM IN THE MARTIAN CORE: IMPLICATIONS FOR AN EARLY DYNAMO.** J.-P. Williams<sup>1</sup> and F. Nimmo<sup>2</sup>, <sup>1</sup> Dept. Earth and Space Sciences, University of California, Los Angeles, CA 90095, jpi-erre@mars.ucla.edu, <sup>2</sup>Dept. Earth Sciences, University College London, Gower St, London WC1E 6BT, UK, nimmo@ess.ucla.edu.

**Abstract:** Planetary geodynamo are driven by thermal or compositional convection in the core. Mars is thought to have possessed a geodynamo which ceased ~0.5 Gyr after the formation of the planet. A possible, but ad hoc, explanation for this behavior is an early episode of plate tectonics, which drove core convection by rapid cooling of the mantle. In this paper we examine an alternative scenario: that the Martian core contains several hundred ppm potassium. The radioactive decay of <sup>40</sup>K provides an extra source of energy to power an early dynamo; its short half-life (1.25 Gyr) ensures that the dynamo will stop early in the planet's history. Recent experimental results suggest that the potassium is likely to partition into the core at the relatively low pressures and high sulfur contents appropriate to Mars [1,2,3]. Thus, the presence of potassium in the Martian core provides a natural explanation for the geodynamo behavior without needing to invoke plate tectonics. Our results also suggest that core solidification is unlikely to have occurred, since this would probably prolong the geodynamo for several Gyr. If the core is entirely liquid, this places a lower bound on sulfur content of ~5 % by weight.

**Introduction:** Strong, linearly magnetized regions of the Martian crust discovered by the Mars Global Surveyor (MGS) Magnetometer/Electron Reflectometer (MAG/ER) investigation [4,5], indicate the presence of an earlier epoch in which Mars possessed a dynamo. The majority of the magnetized crust is in the ancient, heavily cratered terrains in the southern hemisphere. Their absence in and around the large impact basins of Argyre and Hellas imply the Martian dynamo had ceased by the time these impact events occurred, constraining this period to within the first ~500 million years of the planets history [6].

Previous work shows that an early phase of plate tectonics transitioning into a stagnant lid regime could provide the appropriate heat flux out of the core to drive an early, short-lived dynamo [7]. However, strong evidence for plate tectonics having occurred is lacking. Inner core solidification causes compositional convection [8, 9] but requires a sulfur content lower than considered geochemically plausible [10,11] and is unlikely to produce the short geodynamo duration. Radiogenic heating in the core provides an explanation for an early, brief dynamo without invoking the speculative hypothesis of plate tectonics.

**Model Description:** Our thermal evolution model is based on that of [7], which calculates the core and mantle thermal evolution assuming stagnant lid convection is operating. The core parameters adopted are discussed below; we assume that the core remains liquid throughout. We calculate the rate of entropy production within the core as a function of time using the methods of [12] and [13]. The rate of entropy production required to drive the geodynamo is not known; here we assume that any value in excess of the conductive value is sufficient (see Fig 1).

**Martian Core:** Properties of the Martian core are constrained by analysis of the Martian meteorites [10, 11], and the planet's mass and moment of inertia [14] although uncertainties in the core density and size remain as these quantities depend on the interior temperature profile and light element abundance. Further, it is unclear how the thermal expansivity varies with depth in the core and this will affect the adiabat. Recent results by Yoder et al. [15] from MGS radio tracking data indicate the core is at least partially liquid, with an inferred radius between 1520 and 1840 km.

**Model Results:** Figure 1 show our results for a nominal case for Mars with a core sulfur content Fe - 14.2 wt% S and initial core and mantle temperatures of 2800 K. Figures 1A and B show the case with no potassium in the core. Though  $\Delta E$  is maximum early in the core history from the initially higher heat flux out of the core, it never exceeds the conductive threshold, and the geodynamo will thus not operate. With the addition of 400 ppm potassium to the core (Figure 1C and D), it can be seen that the entropy production is now sufficient to drive an early dynamo during the first ~500 Myr. The heat fluxes after 4.5 Gyr are similar because <sup>40</sup>K has decayed.

**Discussion:** Our model demonstrates that the addition of potassium in the core provides a heat source capable of generating the power required to drive a dynamo in a liquid Martian core and provides an explanation for its termination within the first 500 Myr of the planet's history. Future work will explore the effects of varying the initial temperatures of the core and mantle, and the viscosity structure of the mantle.

Our results also suggest that the core is entirely liquid as solidification of an inner core is likely to generate a dynamo with a duration of several Gyr. This places a lower bound on the core sulfur content.

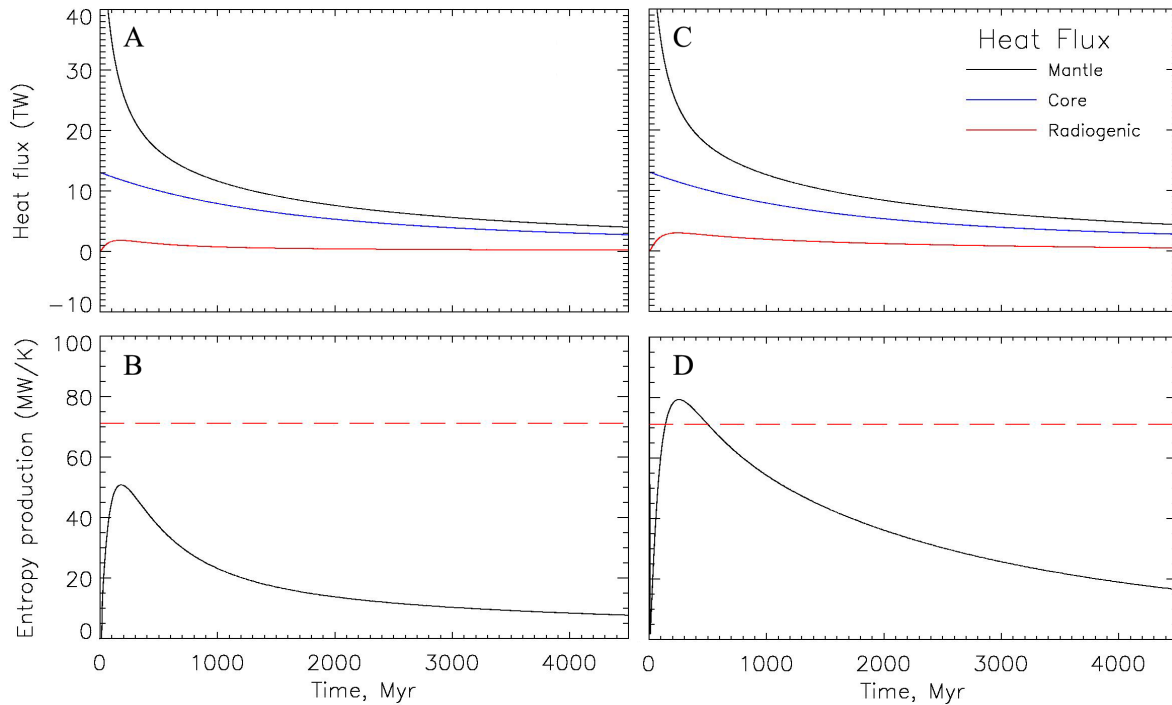


**Figure 1.** Model results showing mantle and core heat fluxes with mantle radiogenic heat production, and core entropy production for liquid Martian core with 14.2 wt% sulfur. A and B) The Core contains no potassium. C and D) with the addition of 400 ppm potassium in the core, excess entropy production drives dynamo that ceases at ~500 Myr. Solid line denotes the rate of entropy production  $\Delta E$  with time. Dashed line denotes the minimum (conductive) entropy production required to drive a geodynamo.

Comparisons of experimental high pressure melting curves for iron and iron sulfide mixtures [15, 16] with corresponding adiabats for the core indicates the liquid core must contain  $> 5$  wt% S. Models based on the chemistry of SNC meteorites [10, 11] estimate a core sulfur content of ~15 wt%, placing the adiabat well above the empirical melting temperatures.

**References:** [1] Gessmann C. K. and Wood B. J. (2002) *EPSL*, 200, 63-78. [2] Murthy et al. (2002) submitted to *Science*. [3] Lee K. K. and Jeanloz R. (2002) *EOS Trans. Am. Geophys. Union.*, 83(47) Abstract #MR62B-1065. [4] Acuna M. H. et al. (1999) *Science*, 284, 790-793. [5] Connerney J. E. P. et al. (1999) *Science*, 284, 794-798. [6] Strom R. G. et al. (1992) in *Mars* Ed. Kieffer et al. UA press. [7] Nimmo F. and Stevenson D. J. (2001) *JGR*, 105, 11,969-11,979. [8] Stevenson D. J. et al. (1983) *Icarus* 54, 466-489. [9] Spohn T. et al. (1998) *Astron. Astrophys. Rev.*, 8, 181-236. [10] Longhi J. et al. (1992) in *Mars* Ed. Kieffer et al. UA press. [11] Wänke H. and Drebus (1988) *Phil. Trans. Roy. Soc. London*, A235, 545-557. [12] Gubbins D. et al. (1979) *Geophys. J. R. Astro. Soc.*, 59, 57-99. [13] Nimmo F. et al. (2003) *Geophys. J. Int.*, submitted. [13] Folkner W. M. et al. (1997)

*Science*, 278, 1749-1751. [14] Yoder C. F. et al (2003) *Science*, 300, 299-303. [15] Boehler R. (1986) *GRL*, 13, 1153-1156. [16] Fei Y. et al. (2000) *Am. Mineral.*, 85, 1830-1833.

**MEASUREMENTS OF DUNE HEIGHTS ON MARS.** K. K. Williams, Center for Earth and Planetary Studies, National Air and Space Museum, Smithsonian Institution, MRC 315, Washington, DC 20013-7012, williamsk@nasm.si.edu.

**Introduction:** Dunes on Mars were first detected during the Mariner 9 mission [1, 2]. The dunes demonstrated that the martian atmosphere must have possessed the combination of wind velocity and atmospheric density necessary to construct dunes in the past Mars climate [3]. Although no evidence of dune change has yet been found [4-7], the question of whether or not the present wind regime can move sand-sized material remains unanswered. The characteristics of dunes do, however, provide information about the history of sediment transport on Mars.

Prior to Mars Global Surveyor, it was not possible to accurately measure the heights of dunes, so estimates of their heights were limited to assumptions of dune slopes. Mars Orbiter Laser Altimeter (MOLA) data can be used to measure heights of large dunes [e.g., 8], but the beam footprint and spacing prevent height measurements of smaller dunes such as barchans. Repeat imaging by Mars Orbiter Camera (MOC) with different look angles allows stereo measurement of heights for dunes of all sizes. The height of a dune can then be used to estimate the volume, a parameter that can be used to further understand the history of aeolian processes on Mars.

In this study, stereo images of dunes in Proctor crater (figure 1) are used to measure the heights of dune brinks. The measured heights are compared to other martian and terrestrial dunes, and the volumes of sand in some dunes are estimated using a simplified geometry for dunes [9].

**Measurement of Dune Height:** Three repeat MOC narrow angle images of barchan dunes at the northern edge of the dune field in Proctor crater have been released. These images are listed in Table 1 and have different viewing geometries. Each image has a resolution better than 5 m/pixel.

Stereo geometry provided by the different look angles allowed for geometric measurement of dune heights. To measure the heights, common points such as dune brinks, boundaries, boulders, and outcrops were selected. Distances between selected points were measured and used together with viewing geometries to construct profiles across the dunes (e.g., Figure 2). Heights of the barchan dunes in the top part of figure 1

**Figure 1.** Portion of MOC image E17-00444 showing barchanoid dunes at the northern edge of the dune field in Proctor crater. North is toward the top.

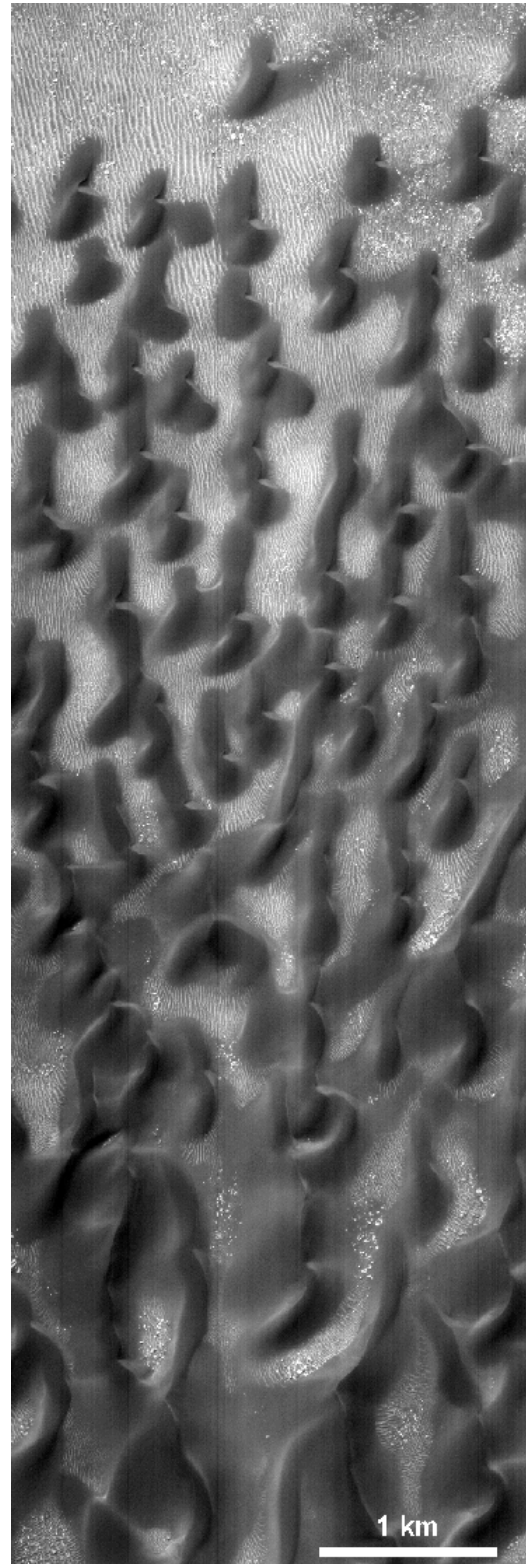


**Table 1.** Characteristics of repeat MOC images of barchan dunes in Proctor.

Image ID	Date	Ls	Resolution	Emission angle <sup>a</sup>
M02-02711	20JUN99	157.31	2.77 m/pixel	0.29°
E03-01039	11APR01	144.34	4.87 m/pixel	22.47°
E17-00444	07JUN02	23.79	4.36 m/pixel	12.06°

<sup>a</sup>Angle between the spacecraft and a 'normal' drawn perpendicular to the surface of Mars.



**Figure 2.** Example of topographic profile over two dunes. Profile is constructed using geometry of distinct points (red dots) on stereo images. Dune on the right is 90 m tall and dune on the left is 80 m tall.

vary but are generally 30-40 m. Dune heights increase moving south into the dune field, and dune morphologies become more complex with the greater supply of sand (figure 1). The larger dunes have heights of up to 100 m.

**Estimate of Dune Volume:** Because barchanoid dunes have a variety of shapes, it is difficult to measure their volumes exactly. A first-order approximation is used to model the volume of a barchan dune following the technique of *Bourke et al.* [9].

The smaller dunes measured in figure 1 have heights of 30-40 m and volumes of approximately 660,000 m<sup>3</sup>. Compared to estimates for dunes of similar height elsewhere on Mars [9], dunes in Proctor crater have greater volumes by a factor of ~3. This is consistent with the Proctor dunes having basal areas larger than the dunes measured by [9].

**Conclusions:** The ability to measure dune heights accurately provides further information about Mars dune characteristics that can be used to better understand the history of aeolian processes on that planet. Previously, discussions of the three-dimensional shapes of dunes on Mars was limited to assumptions of dune slopes. Estimates of dune volumes can be compared to dune volumes in other areas to develop a quantitative understanding of the budget of aeolian material across Mars.

The ability to measure accurate dune heights and to use those measurements to estimate dune volumes opens up a new way to quantify dune characteristics that will aid in better understanding the history (and potential activity) of aeolian processes on Mars.

**References:** [1] McCauley, J.F. et al. (1972) *Icarus*, 17, 289-327. [2] Cutts, J.A. and Smith, R.S.U. (1973) *JGR*, 78, 4139-4154. [3] Greeley, R. and Iversen, J.D. (19985) *Wind as a Geological Process*, 333 pp. [4] Zimbelman, J.R. (2000) *GRL*, 27, 1069-1072. [5] Malin, M.C. and Edgett, K.S. (2001) *JGR*, 106, 23,429-23,570. [6] Edgett, K.S. and M.C. Malin (2000) *JGR*, 105, 1623-1650. [7] Williams, K.K. et al. (2003) *LPS XXXIV*, Abstract #1639. [8] Fenton, L.K. (2003) *JGR*, submitted. [9] Bourke, M. et al. (2003), *JGR*, submitted.

**IDENTIFICATION OF TOPOGRAPHICALLY-CONTROLLED THERMAL TIDAL MODES IN THE MARTIAN UPPER ATMOSPHERE.** Paul Withers<sup>1</sup>, S. W. Bougher<sup>2</sup>, and G. M. Keating<sup>3</sup>, <sup>1</sup>Lunar and Planetary Laboratory, University of Arizona, Tucson, AZ 85716, USA (withers@lpl.arizona.edu), <sup>2</sup>Space Physics Research Laboratory, Atmospheric, Oceanic, and Space Sciences Department, University of Michigan, Ann Arbor, MI 48109-2143, USA, <sup>3</sup>George Washington University at NASA Langley, MS 269, Hampton, VA 23681, USA.

**Introduction:** Mars Global Surveyor (MGS) accelerometer (ACC) observations of the martian upper atmosphere have revealed large variations in density with longitude during northern hemisphere spring at altitudes of 130 – 160 km, all latitudes, and mid-afternoon local solar times (LSTs) [1,2,3]. This zonal structure is due to tides from the surface. The zonal structure is stable on timescales of weeks, decays with increasing altitude above 130 km, and is dominated by wave-3 (average amplitude 22% of mean density) and wave-2 (18%) harmonics. We use a simple application of classical tidal theory to identify the dominant tidal modes and obtain results consistent with those of General Circulation Models. Our method is less rigorous, but simpler, than the General Circulation Models and hence complements them. Topography has a strong influence on the zonal structure.

**Zonal Structure:** Density measurements at fixed altitude, latitude, LST, and season show a clear dependence on longitude. This zonal structure is stable on timescales of a few weeks and spans most of the planet. This zonal structure must originate in the lower atmosphere; it cannot be created *in situ*. There are no zonal inhomogeneities present in solar heating, which powers the dynamics of the martian atmosphere, or in the upper boundary of the atmosphere. There are many zonal inhomogeneities near the lower boundary of the atmosphere, including topography, surface thermal inertia, surface albedo, and lower atmosphere dust loading, which may influence this zonal structure. Since the zonal structure must propagate through, and be affected by, the lower atmosphere, observations of the zonal structure in the upper atmosphere may reveal information about the properties of the lower atmosphere. This zonal structure is caused by atmospheric tides, which are global-scale atmospheric oscillations at periods which are subharmonics of a solar day [4].

**Classical Tidal Theory:** An atmospheric disturbance forced by solar heating can be decomposed into tidal modes with a specific temporal frequency that is a multiple of the rotational frequency of Mars and a specific zonal wavenumber. When viewed from a sun-synchronous platform like the MGS spacecraft that only makes upper atmospheric density measurements at one LST for extended periods of time, such tidal modes appear as time-independent zonal structure with an apparent zonal wavenumber that is a function of the

true temporal frequency and true zonal wavenumber of the tidal mode. In classical tidal theory, each tidal mode can be further decomposed into a sum of Hough modes [5,6]. The meridional structure of a Hough mode is separable from its vertical structure. A sum of Hough modes can thus describe any global-scale atmospheric disturbance forced by solar heating. For a given Hough mode to cause significant zonal structure in the MGS accelerometer observations its latitudinal structure must allow efficient excitation by solar heating and its vertical structure must allow propagation to high altitudes with minimal damping. We have considered the vertical and latitudinal structures of many Hough modes and identified those which can be excited by solar heating and reach the upper atmosphere. Based on those results we suggest which true temporal frequencies and true zonal wavenumbers are responsible for each apparent zonal wavenumber in the observed zonal structure.

**Topography:** Of the zonal inhomogeneities mentioned earlier, topography is the most likely contributor to the zonal structure in the upper atmosphere. Solar heating, the driver for martian atmospheric dynamics, has a meridional profile that is peaked near the equator and decays monotonically towards the poles. A zonal inhomogeneity which matches this meridional profile is most likely to excite strong tidal modes in the atmosphere. Neglecting lower atmospheric dust loading, which is variable over time, only the wave-2 and wave-3 components of topography have a suitable meridional profile. Since the apparent zonal wavenumber of the observed zonal structure is equal to the zonal wavenumber of the zonal inhomogeneity that contributed to the relevant tidal mode, this is consistent with the observed wave-2 and wave-3 dominance in the observed zonal structure.

**References:** [1] Keating *et al.* (1998) *Science*, **279**, 1672-1676 [2] Withers (2003) PhD dissertation, University of Arizona, [3] Withers *et al.* (2003) *Icarus*, under review [4] Forbes (1995) Tidal and Planetary Waves in *The Lower Mesosphere and Upper Thermosphere*, pp. 67-87 [5] Chapman and Lindzen (1970) *Atmospheric Tides* [6] Forbes and Hagan (2000) *GRL*, **27**, 3563-3566

**CHEMISTRY RELATED TO POSSIBLE OUTGASSING SOURCES ON MARS.** A. S. Wong, S. K. Atreya and N. O. Renno, Department of Atmospheric, Oceanic and Space Sciences, University of Michigan, Ann Arbor, MI 48109-2143 (aswong@umich.edu).

**Introduction:** An earlier paper, “Chemical markers of possible hot spots on Mars” by A. S. Wong, S. K. Atreya and Th. Encrenaz [1], explored the modification of the atmosphere of Mars following an influx of methane, sulfur dioxide and hydrogen sulfide ( $\text{CH}_4$ ,  $\text{SO}_2$ ,  $\text{H}_2\text{S}$ ) from any outgassing sources which are referred to as hot spots. The feasibility of detection of the new species by Planetary Fourier Spectrometer on Mars Express is reported in a subsequent paper, “Atmospheric photochemistry above possible martian hot spots” by A. S. Wong, S. K. Atreya, V. Formisano, Th. Encrenaz and N. Ignatiev [2]. This abstract is a follow-up on the previous two papers. Here we treat the effect of any outgassed halogens rigorously. We also make estimates of dilution factors relative to the source location following convection and meridional transport.

The typical terrestrial outgassing species include  $\text{H}_2\text{O}$ ,  $\text{CO}_2$ ,  $\text{SO}_2$ ,  $\text{H}_2\text{S}$ ,  $\text{CH}_4$ , and small amounts of halogens. None of the sulfur, hydrocarbon and halogen species have yet been detected in large-scale surveys of the martian atmosphere. Any localized and transient sources, if present, are likely to go undetected in such observations due to dilution following transport away from source and the relatively short photochemical lifetimes of the species. With the above in mind, and due to considerable interest in the question of extinct or extant life on Mars, we have developed a one-dimensional photochemical model, considering the possibility that  $\text{SO}_2$ ,  $\text{H}_2\text{S}$ ,  $\text{CH}_4$ , and  $\text{HCl}$  from any outgassing sources may be introduced into the martian atmosphere. From this model we predict the abundances of the various new molecules that are expected to be formed in the ensuing atmospheric chemistry. The hot spot photochemical model is based on a globally averaged standard martian atmosphere model which includes all common atmospheric species including nitrogen species, found between the ground and 220 km. A detailed discussion of the model can be found in [1].

**Sulfur Chemistry:** The presence of  $\text{SO}_2$  and  $\text{H}_2\text{S}$  in the atmosphere of Mars has been speculated previously [3, 4]. The upper limits of  $\text{SO}_2$  and  $\text{H}_2\text{S}$  are 0.1 ppm each for globally averaged observations [5]. In our model, we have both gases outgassing from the surface together, and we vary the concentration of each from 0.1 ppm to 100 ppm. The principal reaction pathways are shown in Figure 1. Only for the purpose of illustration, we present the result of one case in

which the surface mixing ratio of each outgassed species is set to 100 ppm (Figure 2). The resulting mixing ratios and column abundances of  $\text{SO}_2$ ,  $\text{H}_2\text{S}$ , and  $\text{SO}$  are summarized in Table 1. All sulfur species scale more or less proportionally with the amount of outgassing species.

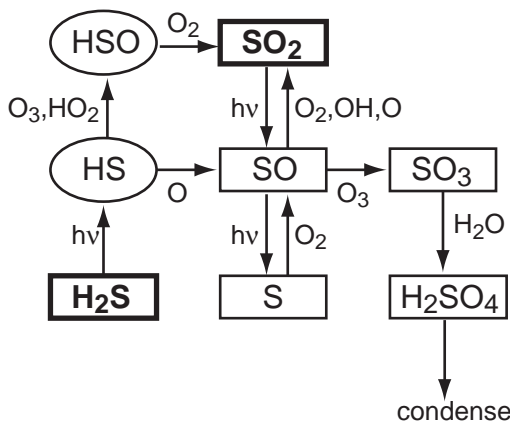


**Figure 1.** Important reaction pathways for sulfur species in the martian atmosphere.

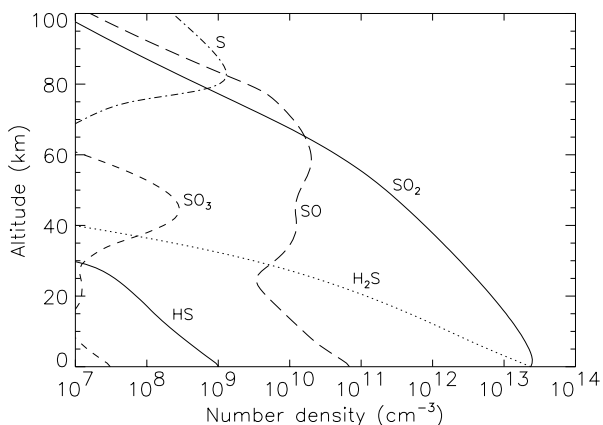


**Figure 2.** Calculated number density profiles of important sulfur species, assuming 100 ppm each of  $\text{H}_2\text{S}$  and  $\text{SO}_2$  is outgassed at the surface of Mars.

Once in the atmosphere,  $\text{SO}_2$  will be photodissociated to produce  $\text{SO}$ . The reaction of  $\text{SO}$  with  $\text{O}_2$  or  $\text{OH}$  recycles some  $\text{SO}_2$ , while the reaction with  $\text{O}_3$  forms  $\text{SO}_3$ , which quickly combines with water vapor to form  $\text{H}_2\text{SO}_4$  and subsequently condenses in the lower atmosphere. Outgassed  $\text{H}_2\text{S}$  is rapidly converted to  $\text{SO}_2$  and the reactions follow that of  $\text{SO}_2$  (see Figure

1). The photochemical lifetime of SO<sub>2</sub> is 160 days, and that of H<sub>2</sub>S is 9 days.

**Table 1.** Summary of possible detectable species from martian hot spots, their mixing ratios (at 10 km), column abundances (above 10 km), and photochemical lifetimes, assuming 100 ppm of SO<sub>2</sub>, H<sub>2</sub>S and CH<sub>4</sub>, and 1 ppm of HCl are outgassed from the surface of Mars.

Species	Mixing ratio at 10 km	Column abundance (cm <sup>-2</sup> )	Photochemical lifetime
SO <sub>2</sub>	1.7×10 <sup>-4</sup>	1.8×10 <sup>19</sup>	180 days
H <sub>2</sub> S	1.8×10 <sup>-5</sup>	7.4×10 <sup>17</sup>	9 days
SO	1.7×10 <sup>-7</sup>	7.8×10 <sup>16</sup>	4.6 hours
CH <sub>4</sub>	1.0×10 <sup>-4</sup>	1.0×10 <sup>19</sup>	670 years
CH <sub>2</sub> O	2.8×10 <sup>-11</sup>	1.6×10 <sup>13</sup>	7.5 hours
CH <sub>3</sub> OH	4.3×10 <sup>-12</sup>	8.2×10 <sup>11</sup>	74 days
C <sub>2</sub> H <sub>6</sub>	6.4×10 <sup>-12</sup>	9.6×10 <sup>11</sup>	25 days
HCl	1.0×10 <sup>-5</sup>	1.0×10 <sup>17</sup>	5.7 years

**Hydrocarbon Chemistry:** If present, methane could be of geochemical or biological origin. The present upper limit of CH<sub>4</sub> from global surveys is 0.02 ppm [5]. Our model calculates the abundances of new species that get formed upon the introduction of CH<sub>4</sub> into the martian atmosphere by outgassing, and the important pathways are shown in Figure 3. For the purpose of illustration, the result for a case with 100 ppm CH<sub>4</sub> is shown in Figure 4. The most abundant species are CH<sub>4</sub>, CH<sub>2</sub>O, CH<sub>3</sub>OH, and C<sub>2</sub>H<sub>6</sub>, and the resulting mixing ratios and column abundances are summarized in Table 1.

At altitudes above 80 km, CH<sub>4</sub> is photodissociated into CH, <sup>3</sup>CH<sub>2</sub>, <sup>1</sup>CH<sub>2</sub> and CH<sub>3</sub>, and its oxidation by O(<sup>1</sup>D) forms CH<sub>3</sub>. <sup>3</sup>CH<sub>2</sub> reacts with CO<sub>2</sub> to form CH<sub>2</sub>O. At the low altitudes, the oxidation of methane by OH forms CH<sub>3</sub>. CH<sub>3</sub> reacts with O to form CH<sub>2</sub>O, reacts with OH to form CH<sub>3</sub>OH, and recombines to form C<sub>2</sub>H<sub>6</sub>. The abundances of hydrocarbons derived from the methane photochemistry are very low even when the concentration of methane is relatively large in the atmosphere. The reason is that CH<sub>4</sub> does not dissociate efficiently to start the hydrocarbon chemistry. Photolysis of CH<sub>4</sub> is largely shielded by the much more abundant CO<sub>2</sub> whose absorption cross section overlaps that of CH<sub>4</sub>. In the lower atmosphere, the most effective way to break down methane is by reaction with OH, which is quickly removed by CO and O. The photochemical lifetime of CH<sub>4</sub> is about 670 years, which is the longest amongst the principal hydrocarbon species. Therefore, CH<sub>4</sub> may be easier to detect even far from the source region, provided that its

source flux is reasonably large. On the other hand, CH<sub>2</sub>O has a relatively short lifetime of several hours. Therefore, if the previous tentative detection of CH<sub>2</sub>O (0.5 ppm, [6]) is confirmed by future observations, it would imply a nearly continuous supply of methane to the atmosphere. Moreover, the amount of methane required would have to be much greater than the “global” upper limit of 20 ppb, since the models produce only 30 ppt of CH<sub>2</sub>O with 100 ppm of CH<sub>4</sub>. On the other hand, CH<sub>2</sub>O itself could also be outgassed from the interior, or formed in surface reactions.

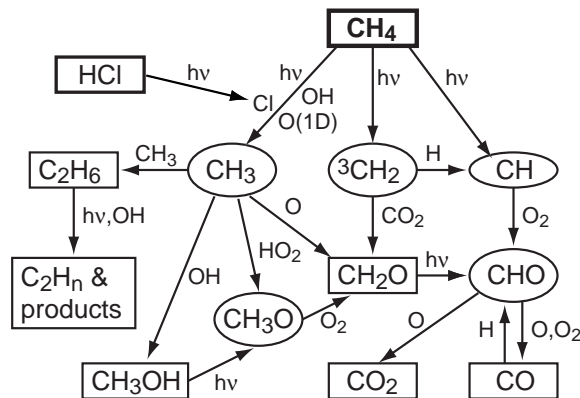


**Figure 3.** Important reaction pathways of hydrocarbon and halogen chemistry in the martian atmosphere.

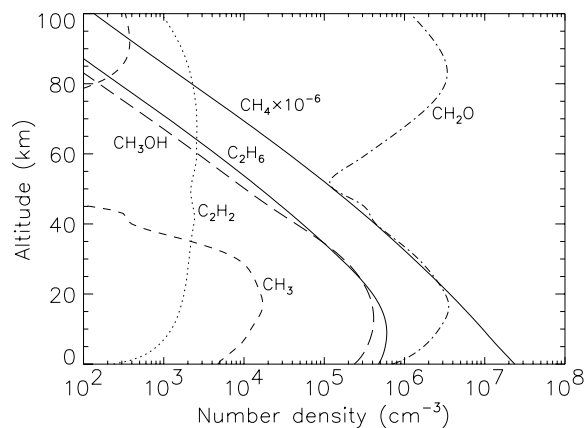


**Figure 4.** Calculated number density profiles of important hydrocarbon species, assuming 100 ppm of CH<sub>4</sub> is outgassed at the surface of Mars.

**Halogen Chemistry:** In terrestrial outgassing, only a very small amount of halogens (HCl, Cl<sub>2</sub>, etc.) are released from outgassing processes. The total amount of halogens comprises a small fraction, about 1%, of SO<sub>2</sub>, mostly in the form of HCl [7]. On Mars, the present global upper limit of HCl is 2×10<sup>-9</sup> [8], which is presumably the most abundant halogen. Our model finds that with up to 1 ppm of HCl outgassing,

the direct effect of halogens on the “standard” atmosphere, as well as on sulfur chemistry, is negligible.

We investigate the effect of halogens on hydrocarbon chemistry. When HCl is released into the atmosphere together with methane, it is broken down by the solar ultraviolet photons at  $\lambda \leq 230$  nm and OH radicals to form the atomic chlorine. Chlorine reacts in a similar way to OH, enhancing the breakdown of methane into  $\text{CH}_3$  (Figure 3) and subsequently increasing the production of other hydrocarbons. Our model shows, with 1 ppm of HCl outgassing alongside with 100 ppm of  $\text{CH}_4$ , the column abundances of  $\text{CH}_2\text{O}$ ,  $\text{CH}_3\text{OH}$ , and  $\text{C}_2\text{H}_6$  are increased by 6, 2 and 3 times, respectively, compared to the case of no HCl outgassing (Figure 5). The overall effect on  $\text{CH}_4$  is minimal. The lifetime of HCl is calculated to be 5.7 years.

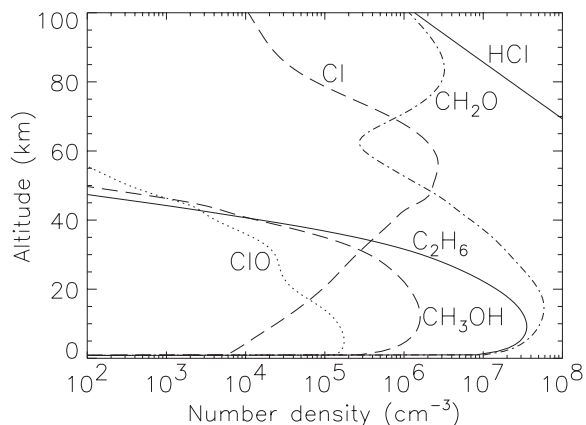


**Figure 5.** Calculated number density profiles of important hydrocarbon and halogen species, assuming 100 ppm of  $\text{CH}_4$  and 1 ppm of HCl are outgassed at the surface of Mars. This figure illustrates the effects of halogens on hydrocarbon chemistry.

**Conclusion and Discussions:** We have shown that if outgassing is taking place somewhere on Mars today, only a handful of new species with significant abundance would be formed as a result of photochemical processes involving the products of outgassing. In particular, the outgassed  $\text{H}_2\text{S}$  and  $\text{SO}_2$  would produce significant amounts of only SO in the gas phase. Similarly, photochemistry of any outgassed  $\text{CH}_4$  would produce appreciable amounts of only  $\text{CH}_2\text{O}$  and  $\text{CH}_3\text{OH}$ , but the hydrocarbon photochemical products would be much less abundant than  $\text{CH}_4$ . Thus, the best candidates for the chemical markers of any hot spots on Mars are  $\text{SO}_2$ ,  $\text{H}_2\text{S}$ ,  $\text{CH}_4$ , possibly HCl, SO,  $\text{CH}_2\text{O}$ , and  $\text{CH}_3\text{OH}$ . The largest source of methane in the earth's atmosphere is methanogenic bacteria living in anaerobic soils in tropical forests, swamps and rice paddies and in the guts of cattle and other grass eating animals, with smaller contributions from fossilized

matter. Methane and its products could serve as possible biomarkers in the martian atmosphere as well. Halogens would probably outgas in very small amounts, and their only noticeable effect on the atmosphere and outgassing chemistry is the slight increase of hydrocarbon photoproducts.

In the relatively short time-scale of about an hour, ordinary convective processes alone can reduce the mixing ratios of outgassed species by factors of  $10^4$ – $10^5$ , spreading the outgassed species over distances of up to 50 km away from the source. In addition, the time-scale for spreading the outgassed species over the entire planet (with corresponding dilution factor of  $\sim 10^8$ ) would be approximately one year. In view of these time scales and the relatively short photochemical lifetimes of the species, detection of any sulfur or hydrocarbon species would indicate presence of currently active hot spot/s in close proximity of the observation. Unless the source flux is extremely large, detection far from a transient source would be unlikely due to dilution. The best conditions for detecting any possible hot spots would be over valleys, between early and mid mornings. At this time period, any outgassed species would be trapped between the surface and the top of the thermal inversion created by the nocturnal radiative cooling of the surface and lower atmosphere. Thus, the near surface concentration of outgassed species would be the highest. As the depth of the convective layer increases during the morning, this concentrated layer gradually grows, up to values larger than the atmospheric scale height (about 10 km). During the cold season, convection is inhibited, the thermal inversions are stronger, and the convective layers shallower. Therefore, morning limb observations during winter are ideal for detecting any possible martian hot spots. The best locations to find hot spots include martian high latitudes where most of the signs of recent water seepage and ground water runoff have been seen, and calderas of volcanoes in the Tharsis.

**Acknowledgements:** SKA acknowledges support received from NASA's Planetary Atmospheres Program and NASA's Mars Program Office at JPL for U.S. Participation in the Mars Express Project.

**References:** [1] Wong A. S. et al. (2003) *JGR*, 108(E4), 5026, doi:10.1029/2002JE002003. [2] Wong A. S. et al. (2003) *Adv. Space Res.*, in press. [3] Farquhar J. et al. (2000) *Nature*, 404, 50–52. [4] Wänke H. and Dreibus G. (1994) *Phil. Trans. Phys. Sci. Eng.*, 349, 285–293. [5] Maguire W. S. (1977) *Icarus*, 32, 85–97. [6] Korablev O. I. et al. (1993) *PSS*, 41, 441–451. [7] Walker J. C. G. (1977) *Evolution of the atmosphere*, p. 205, Macmillan. [8] Krasnopolsky V. A. et al. (1997) *JGR* 102, 6526–6534.

**MGS Observations and Modeling of Martian Lee Wave Clouds.** S. E. Wood<sup>1</sup>, D. C. Catling<sup>1</sup>, S. C. R. Rafkin<sup>2</sup>, E. A. Ginder<sup>1</sup>, C. G. Peacock<sup>1</sup>, <sup>1</sup>*Dept. of Atmospheric Sciences, University of Washington, Seattle WA,* <sup>2</sup>*Dept. of Space Studies, Southwest Research Institute, Boulder CO.*

**Introduction:** Lee wave clouds form when stable air is deflected vertically by a topographic obstacle and undergoes a wave-like oscillation in the lee of the obstacle. Condensation occurs at the adiabatically-cooled crest of the waves, usually leaving a regular train of clouds aligned orthogonal to the prevailing wind and/or a “ship’s wake” divergent pattern. The existence of lee waves in the Martian atmosphere has been known since Mariner 9 [1]. Craters varying in size from a few to hundreds of kilometers commonly generate lee waves on Mars (i.e., **Figure 1**). For larger craters, waves can extend up to nearly 1000 km downstream of their source [1-5]. The wavelength and propagation characteristics of lee waves are determined by the temperature (stability) and wind profiles of the atmosphere, as well as moisture in the impinging flow, so they allow us to make inferences about the atmospheric structure and dynamics. Also the statistical occurrence of lee wave clouds in preferred seasons and locations allows us to tie lee wave incidence to the general climatic state of the Martian atmosphere. In previous missions, coverage has not been systematic. Mars Global Surveyor (MGS) provides an opportunity to systematically look at the occurrence of lee waves and correlate this with meteorological predicaments. The only significant limitation from MGS is lack of local time coverage.

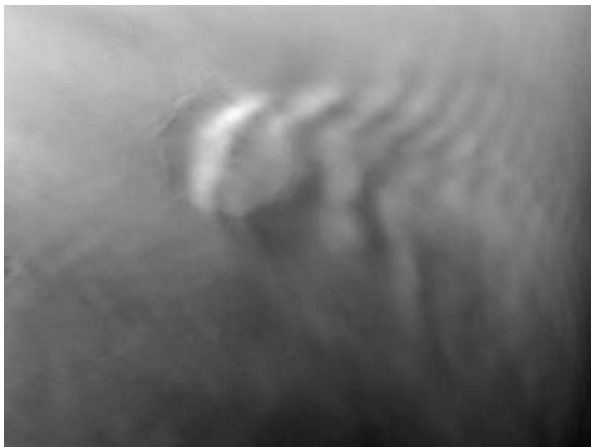


**Fig. 1.** Lee wave clouds generated by Milankovic crater (55N, 148W, diam~110 km) on  $L_s=234$ . (MOC-WA image M08/07249).

MOC wide-angle (WA) images have a better footprint for observing clouds than the narrow-angle MOC images. The red- and blue-filtered WA images

allows us to distinguish ice clouds (bright in the blue) from dust clouds (bright in the red), at least where paired images of the same scene were taken. Radio Science (RS) data can provide vertical temperature profile context in principle, but there is scant overlap in local time with the relevant images. The Thermal Emission Spectrometer (TES) has better coverage in space and time than RS; it can provide context for cloud and vapor distribution, but temperature profiles have insufficient vertical spatial resolution for direct application to lee waves. MOLA provides excellent surface topography for models, as well as some direct cloud observations. However, direct cloud observations are biased towards CO<sub>2</sub>-ice clouds, which are reflective, rather than H<sub>2</sub>O-ice clouds, which are absorptive.

**Observations and Interpretation:** We are currently compiling a cloud catalog from MOC WA images of condensate clouds. Consistent with the results of [5], which is based on global swath images, lee wave clouds are found to occur in the mid-latitude and polar regions in fall and winter of the respective hemisphere, with wavelengths of up to 50 km. Unlike [5], our study also includes all of the regional-scale WA images, which allows detection of lee wave clouds with smaller wavelengths (i.e., **Figure 2**) as well as a more detailed analysis of their shape and structure. In some cases we observe shadows that can be used to derive cloud heights.

Two particular questions come to mind: (1) Why is the Martian atmosphere apparently prone to a large amount of lee wave activity (2) What determines the seasonal trends?

We find that the occurrence of lee waves has less to do with the water vapor abundance and more to do with the dynamical state of the atmosphere. Northern hemisphere water vapor peaks at  $\sim L_s$  120 and yet there is little occurrence of lee wave clouds before  $L_s=170$ . The reason can be deduced from understanding the conditions required for lee wave occurrence, as follows.

*Conditions for trapped lee waves:* The horizontal ( $k$ ) and vertical wavenumbers ( $m$ ) of the wave are coupled through the Scorer Parameter ( $l$ ), given by:

$$l^2 = \frac{N^2}{U^2} - \frac{1}{U} \frac{\partial^2 U}{\partial z^2}, \text{ where } l^2 = m^2 + k^2 \quad (1)$$

where  $U$  is the wind speed and  $N$  is the Brunt-Vaisala frequency [e.g., 6]. The horizontal propagation of the

wave, and the presence of clouds, is strongly controlled by the atmospheric structure. For example, if  $k < l$ , then the lee wave is vertically propagating (does not damp with height). Such a wave can result in the appearance of a single wave disturbance directly over the obstacle through a depth of the atmosphere where  $l$  remains greater than  $k$ . When  $k > l$ , the wave is damped with height ( $m$  is imaginary). In the simplest “two layer” idealization for trapped waves in the lee of a ridge, the lower layer has conditions such that the intrinsic frequency of the wave,  $Uk$ , is less than  $N$  and in the upper layer has  $Uk > N$ . Under these conditions, the wave is not damped in the lower layer, while it is evanescent (dying away in amplitude) in the upper layer. The wave is thus trapped. Thus if the vertical variations of  $N$  and  $U$  are such that the Scorer Parameter decreases significantly with height, then cross-topographic flow is prone to give rise to a lee waves.

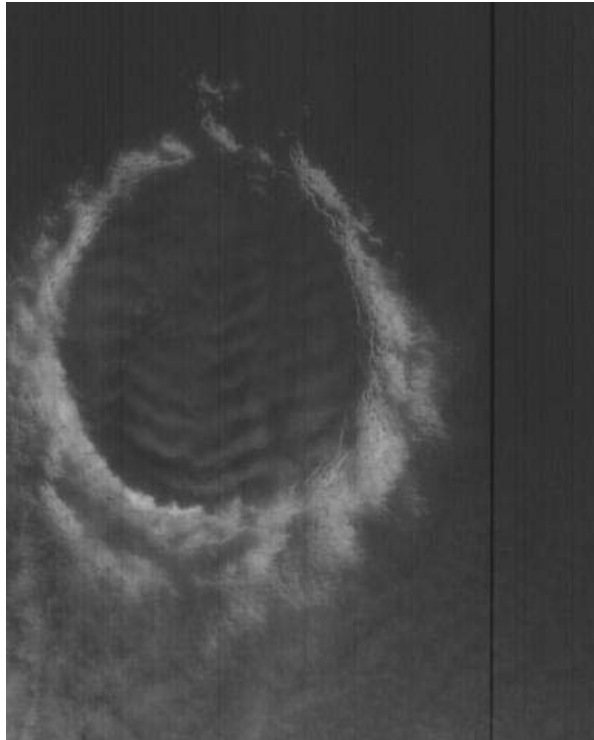


**Fig. 2.** Small wavelength (~7km) lee wave clouds inside Lomonosov crater (65N, 9W, diam~150km) on  $L_s=53$ . (MOC-WA image M19/01563).

Values of  $N(z)$  can be obtained from RS temperature profiles typical of a particular season or GCM output. Values of  $U(z)$  must generally be obtained from GCM output for a particular location. From these values we can derive  $l(z)$  as a function of time and space. We can also calculate an effective “Scorer wavelength” ( $\lambda_s = 2\pi/l$ ) as a function of height

This  $\lambda_s$  parameter must increase with altitude  $z$  for waves to exist, and if so, it provides an upper limit to their wavelength. **Figure 3** shows profiles for a location near Korolev crater (73N, 196W) at three different seasons showing development of conditions conducive to leewaves.

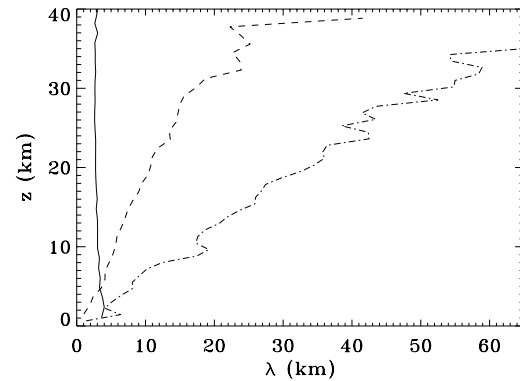


**Fig. 3.** Vertical profiles of the “Scorer wavelength” in the atmosphere at high northern latitudes derived from Radio Science occultation profiles taken on  $L_s=100$  (solid line),  $L_s=166$  (dashed line), and  $L_s=180$  (dot-dash line).

This shows that lee waves are not expected for the summer season, as indeed is observed. Only as summer progresses to fall does the Scorer parameter become liable to decrease significantly with height (or equivalently  $\lambda_s$  increases with altitude  $z$ ). This gives rise to the conditions for trapped lee waves.

Consequently, the answer to why Mars has significant autumn and winter lee wave activity in midlatitudes is that the wind shear is very large, with wind speeds increasing greatly with height because of the winter midlatitude jet stream. For a linear velocity profile, Eqn. (1) becomes  $l^2 \approx N^2/U^2$ , which is dominated by the denominator term in zonal wind. The answer to why lee waves are prevalent in the autumn and winter is that the strong variation of wind with height is only set up during these seasons.

We are also undertaking more detailed modeling using linear models that can predict the horizontal wavelength (which is the main feature observed in images), and shapes of the waves. A particular trait of crater lee waves on Mars that often occurs is a pattern of diverging cloud trains as seen in a “ship’s wake”. This is in contrast to transverse clouds, which are orthogonal to the wind direction in the lee of the crater. More comprehensive and less idealized simulations can be obtained from the MRAMS mesoscale model [7].

**References:** [1] Briggs G. A. and Leovy C. B. (1974) *Bull. Amer. Met. Soc.*, 55, 278. [2] Pirraglia, J. A., (1976) *Icarus*, 27, 517. [3] Briggs, G. A. et al., (1977) *JGR* 82, 4121. [4] Pickersgill, A. O., and G. E. Hunt, *JGR* 84, 8317. [4] Kahn R. (1984) *JGR* 89, 6671-6688. [5] Wang H. and Ingersoll A. P. (2002) *JGR* 107, 5078 [6] Durrant, D. R. (1986) in *Met. Monographs*, 23, 59, Amer. Met. Soc. [7] Rafkin, S. C. R. et al. (2001) *Icarus* 151, 228.

**ICE KEEL SCOUR MARKS ON MARS: EVIDENCE FOR FLOATING AND GROUNDING ICE FLOES IN KASEI VALLES.** Christopher Woodworth-Lynas and Jacques Yves Guigné, Guigné International Ltd. 685 St. Thomas Line, Paradise, Newfoundland, CANADA A1L 1C1 709 895 3819 chriswl@guigne.com

**Introduction:** We present new observations from preliminary analyses of Mars Global Surveyor Mars Orbiter Camera images of surficial features interpreted to be the result of interactions between the keels of floating ice masses on submerged sediment. These narrow, intersecting curvilinear trough-like features are ice keel scour marks and are present in large reaches of the Kasei Valles system (Figure 1). We base our interpretations on the morphology of individual scour marks, on ice keel grounding structures and on local scour mark patterns. We compare these Mars observations with identical contemporary structures forming in an analogous environment in the St. Lawrence River on earth.

**Background:** If an ocean existed in the north polar basin, it is quite reasonable to expect that it would have been seasonally partly or fully covered by floating sea ice, e.g. Luchitta *et al.* [1] as is the case for the Arctic and Southern Oceans on Earth. Similarly, it is reasonable to expect that even at temperate latitudes large rivers emptying into a cold ocean could carry significant volumes of river ice out into the ocean as, for example, the St. Lawrence River does each spring. Floating ice (river ice, lake ice, sea ice or icebergs) commonly leaves mechanical traces of its former presence through the creation of ice keel scour marks on the seafloor (Figure 1). One way to test the hypothesis of ice-covered rivers and of an ice-covered ocean on Mars is to search for scour marks that may be preserved on ancient sedimentary flood surfaces.

Scour marks are the seafloor tracks made by floating ice masses as their keels mechanically plough into soft sediments of lake, river or ocean floors. On Earth scour marks are ubiquitous features on the seafloors of the modern Canadian Arctic (Figure 2) and sub-arctic regions from Baffin Bay to the Grand Banks (Figure 3) and on the Beaufort Sea and Russian polar continental shelves, as well as on the circumpolar seafloor on the continental margin of Antarctica. Scour marks on the modern seafloor may range from present day to 10 or 20 thousand years in age.

Scour marks commonly survive the transition from submergence to exposure above water level and ancient features are commonly seen, for example, over large areas of southern Manitoba and parts of southern Ontario formerly occupied by glacial Lake Agassiz and glacial Lake Iroquois [2]. They are also found on

several large islands of the Arctic Archipelago (e.g. King William Island, Victoria island) and are readily identified from aerial photographs. These relic features were formed in large pro-glacial lakes and (in the Arctic) areas formerly submerged below sea level some 10,000 years ago [3]. Scour marks preserved in Pre-Cambrian, Ordovician and Carboniferous/Permian age glacialine sediments have also been identified on exposed bedding plane surfaces in several localities worldwide [4].

On Earth scour marks form today in water depths from < 5 - 500 m, and fall in the range < 100 m to several kilometers long, 5 - 100 m wide and < 1 - 5 m deep (exceptionally 25 m). The surface morphology of scour marks typically comprises a curvilinear trough from which seabed material has been excavated and ploughed up and to the sides by the entrenched, moving ice keel, to form two co-linear berms of excavated material. Scour marks commonly occur in extensive and numerous criss-crossing populations. The orientations and distributions of scour marks can be linked to wind and current directions and to long-term changes in sea levels and ice regimes.

**Rationale:** In a preliminary analysis we examined several hundred high resolution narrow angle images acquired by the Mars Orbiter Camera (MOC). We chose to restrict our initial search for ice keel scour marks to two general environments: the margins of Chryse Planitia in the vicinity of an ancient shoreline, Contact 2, proposed by Parker *et al.* [5] and largely substantiated by Ivanov and Head [6] (2001), and to the valley floor regions of the six great valley systems that empty into Chryse: the Mawrth, Ares, Tiu, Simud, Maja and Kasei Valles systems. We restricted our search to these regions because it was felt that floating ice masses, either river ice carried out into an ocean from the valleys, or sea ice would likely ground and scour in the littoral waters of a river mouth and near-shore region, and that traces of this activity may well be preserved on the most recently deposited surfaces.

**Description of Martian features:** On the flat valley floor of Kasei Valles we have found networks of curvilinear, intersecting, parallel-sided troughs that meander and intersect with no consistent orientation (Figures 2 to 3). In most areas the troughs are cut into a typically rough-textured surface that characterizes the flat valley floor, and the troughs are always of darker

albedo than the rough-textured valley floor. The troughs typically are at least 1 km long and some exceed 3 and 4 km and range in width from 10 – 50 m. By observing sun shadows it is possible to distinguish narrow ridges, or berms, on one or both sides of most troughs. Where berms are not observed, and where the sun angle is more or less orthogonal to the troughs, shadows are cast on the side nearest the sun, and bright, illuminated margins form the other side. Some troughs close to the valley margins are buried beneath talus slopes. In places multiple, overlapping sub-parallel troughs coalesce into wide (100 - 300 m), irregular-sided grooved and ridged surfaces.

Associated with the troughs are poorly- to moderately well-defined irregular to sub-circular, smooth, low albedo regions, the margins of which are defined by low continuous ridges. These ridge-defined smooth areas range in size from 200 to 600 m, exceptionally up to 950 m. They may occur as solitary features, but more commonly occur in groups forming jig-saw-like ridge networks (e.g. Figure 3).

In MOC images where it is observed the rough-textured surface of the valley floor is caused by small-scale, poorly- to moderately well-defined, discontinuous, narrow arcuate lineaments that have the appearance of possible degraded megaripple crests. The arcuate lineaments are generally oriented across the valley and are defined by high albedo with a lower albedo, wider inter-lineament area. Wavelengths range between 33 and 40 m.

The parallel-sided troughs with berms, the ridge-defined smooth areas and the arcuate lineaments are restricted in their occurrence to the lowest and flattest portion of the valley floor of the southernmost branch of Kasei Valles (Figure 1). They do not appear to occur at or east of the valley mouth in Chryse Planitia. They do not occur on any of the older, elevated surfaces of the Kasei system.

**Description of St. Lawrence Estuary features:** Ice keel scour marks are formed on extensive tidal mud flats during the breakup of river ice each spring in the St. Lawrence estuary (Figure 4). Scour marks are common on mud flats on the southern shore in a stretch at least 125 km long where the estuary is 15 – 25 km wide. The scour marks are formed in shallow water (<1 m to approximately 3 m deep) during flood tides and are exposed during low tide e.g. Dionne [7,8]. The scour marks form a network of curvilinear, parallel-sided troughs that meander and intersect. The troughs range from 1 m to 20 or 30 m in width. Some troughs are characterized by ridges and grooves

formed by irregularities in the base of the ice keel. The margins of most troughs are characterized by narrow ridges, or berms, formed by the bulldozing and ploughing action of the scouring ice keels. Depending on location there is a preferred orientation of the troughs that roughly parallels the river axis. However networks of scour marks are formed at high angles to the shoreline and are the result of scouring ice masses driven shore-wards by strong cross-valley winds (scour marks in center right of Figure 4).

The scour marks are formed by keels of large, flat first-year ice floes that are typically 20 - 50 m in diameter and 1 - 2 m thick. Large, composite ice masses that are 3 - 4 m thick formed by ice pressure during the winter months have deeper keels and tend to make deeper scour marks in deeper water.

The scour marks are associated with irregularly shaped depressions, the margins of which are generally characterized by small ridges. These features are grounding pits created by ice floes that become stranded during low tide. As the floes settle into the riverbed, mud is displaced outwards and upwards along the margins to form low ridges that preserve an imprint of the floe. In places large numbers of floes ground together creating jigsaw-like patterns of ridges (Figure 4). Where moving floes ground together the leading edges may create a local system of arcuate ice push ridges.

**Interpretation of Martian features:** We interpret the small-scale troughs on the floor of the Kasei Valles system as ice keel scour marks made by the grounding keels of floating ice floes. We interpret the associated ridge-defined low albedo regions as grounding pits made by stranded tabular floes. The megaripple-like surfaces on which the scour marks and grounding pits appear to have formed in the lower Kasei Valles formed during a period of strong unidirectional down-valley currents. There may have been floating ice present and ice scouring may have occurred during megaripple formation but all traces have been erased by the migrating ripples. As the strong currents associated with the megaripples waned, ice scour marks and ice floe grounding pits formed and were preserved. The meandering tracks of the scour marks point to a significant decrease in unidirectional flow, and suggest that winds may have played a significant role in driving the scouring floes.

We interpret the wide lanes of multiple, overlapping sub-parallel troughs as zones marking the boundary between stationary fast ice and moving ice. Shear zones such as these are commonly formed between landfast ice and the offshore arctic pack in the Cana-

dian and U.S. Beaufort Sea. These regions of linear shear in the ice canopy, referred to as Stamukhi zones, are typically regions of intense ice keel scouring of the seafloor e.g. Barnes *et al.* [9]; Reimnitz and Barnes [10].

*Regional context.* We have found that the ice keels scour marks appear to be quite restricted in their occurrence to the southern branch of Kasei Valles and that scouring occurred for a long distance up-valley. Indeed cursory examination of a few MOC images of the southwestern reaches of Kasei Valles, towards Valles Marineris, show regions of possible scour marks and areas of ice floe grounding pits. We have not yet found traces of ice keel scouring in the valley floors of the Mawrth, Ares, Tiu, Simud and Maja valley systems, and have found no traces in Chryse Planitia in the vicinity of Contact 2.

The geological units that define the six Valles systems emptying into Chryse Planitia span the time interval from mid-Noachian, all of the Hesperian and into the early Amazonian (Ivanov and Head, 2001; Tanaka, 1997). The youngest Valles geological unit is Kasei unit 2 mapped by Rotto and Tanaka (1995) and Tanaka (1997). It is in this unit that the Kasei Valles scour marks all formed.

**Discussion and implications:** An analysis of MOC images of the southern portion of the Kasei Valles system show the preserved traces of ice keel scour marks and ice floe grounding pits on the flat valley floor within the stratigraphic Kasei unit 2. The scour marks are therefore of early Amazonian age and are the most recent features preserved in all of the six valley systems surrounding Chryse Planitia.

Scour marks are a proxy indicator of environment, from which the following three fundamental conclusions are drawn, namely that they demonstrate:

1. the former presence of a water body;
2. the water body must have been at least seasonally, or perhaps permanently, covered by ice floes;
3. the water area must have been large enough for wind and current to drive the floes forward during ice/seabed interaction.

#### References:

[1] Luchitta, B.K., H.M. Ferguson and C. Summers. 1986. Sedimentary deposits in the northern lowland plains, Mars. JGR, 91 supplement E166-E174.

[2] Gilbert, R.J., Handford, K.J. and Shaw, J., 1992. Ice scours in the sediments of glacial Lake Iroquois, Prince Edward County, eastern Ontario. *Geographie physique et Quaternaire* v. 46, 189-194.

[3] Woodworth-Lynas, C.M.T. and J.Y. Guigné. 1990. Iceberg scours in the geological record: examples from glacial Lake Agassiz. In, *Glacimarine environments: processes and sediments* (J.A. Dowdeswell and J.D. Scourse, eds.). Geol. Soc. Spec. Pub. No. 53: 217-233.

[4] Woodworth-Lynas, C.M.T. 1992. The geology of ice scour. Ph.D. thesis, University of Wales.

[5] Parker, T.J., D.S. Gorsline, R.S. Saunders, D.C. Pieri and D.M. Schneeberger. 1993. Coastal geomorphology of the Martian northern plains. JGR, 98: 11061-11078.

[6] Ivanov, M.A. and J.W. Head. 2001. Chryse Planitia, Mars: Topographic configuration, outflow channel continuity and sequence, and tests for hypothesized ancient bodies of water using Mars Orbital Laser Altimeter (MOLA) data. JGR, 106 (E2): 3275-3295.

[7] Dionne, J.C., 1972, Ribbed grooves and tracks in mud tidal flats of cold regions: *J. of Sed. Pet.* v. 41: 848-851.

[8] Dionne, J.C., 1974, Polished and striated mud surfaces in the St. Lawrence tidal flats, Québec: *Can. J. Earth Sci.* v. 11: 860-866.

[9] Barnes, P.W., D.M. Rearic, and E. Reimnitz. 1984. Ice gouging characteristics and processes, In, *The Alaskan Beaufort Sea - Ecosystems and Environments*. Academic Press, Orlando: 185-213.

[10] Reimnitz, Erk, and P.W. Barnes. 1974. Sea ice as a geologic agent on the Beaufort Sea shelf of Alaska: In, *The Coast and Shelf of the Beaufort Sea*, edited by J.C. Reed, and J.E. Sater, Arctic Institute of North America, Arlington, VA: 301-351.

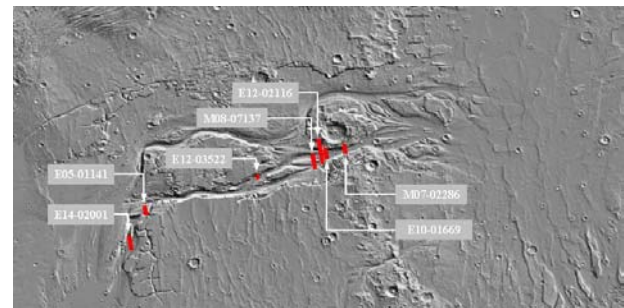


**Figure 1: Kasei Valles showing MOC images used in the study.**

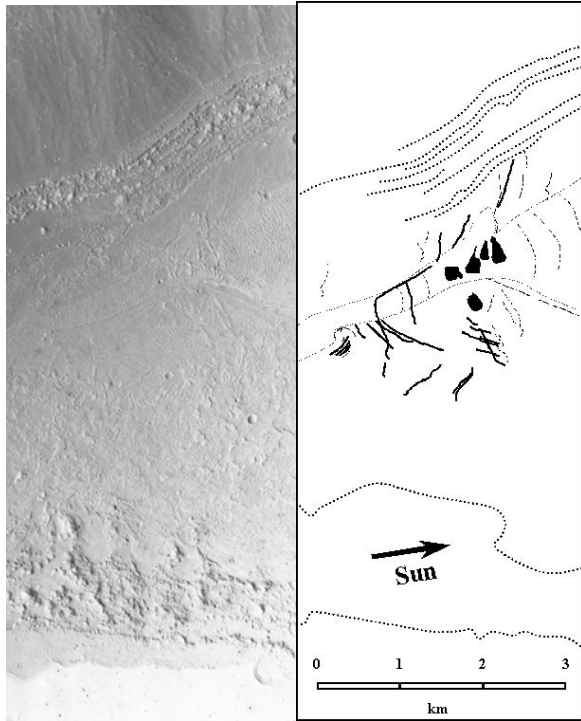


Figure 2. MOC image and interpretation of ice keel scour marks (black lines) in southwestern Kasei Valles (MOC image E0-501141).

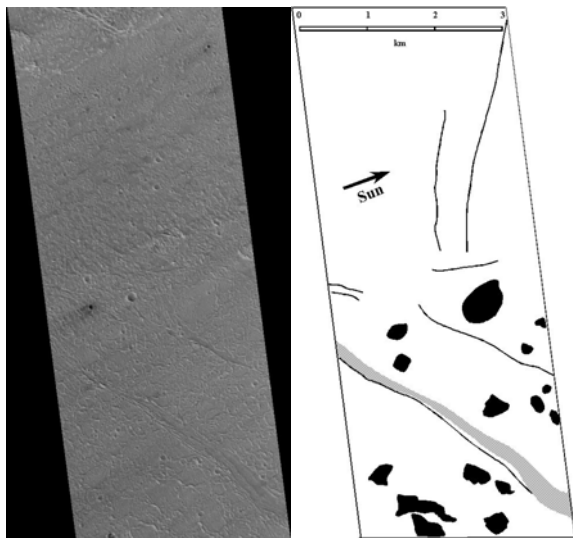


Figure 3. MOC image and interpretation of ice keel scour marks (black lines) and ice floe grounding pits (black patches) in mid-Kasei Valles (MOC image E12-03522).

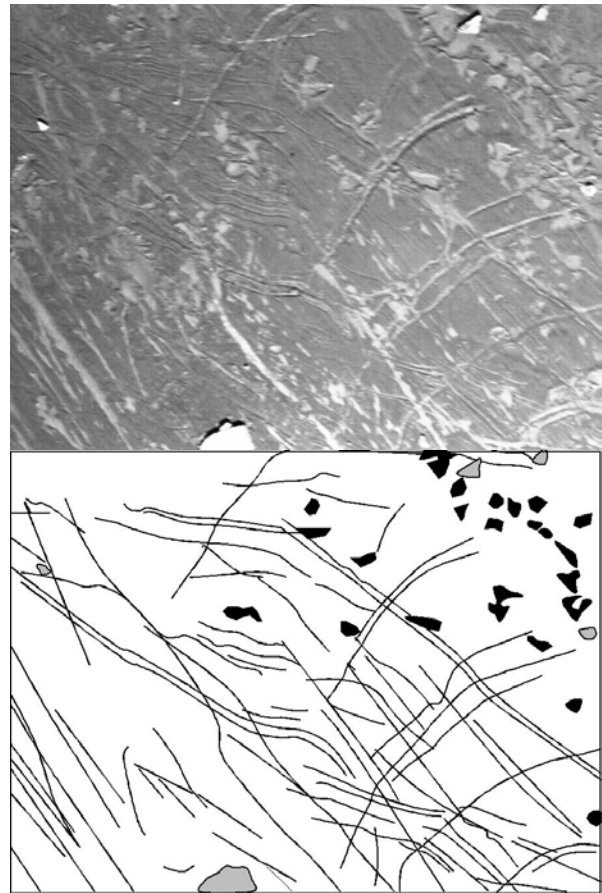


Figure 4. Aerial photograph of ice keel scour marks and ice floe grounding pits (black lines and black areas), St. Lawrence Estuary, Canada. Most scour marks are parallel to the river but some, oriented towards the top right, have been created by wind-driven floes (view approximately 1 km wide).

**ACCUMULATION OF DISTAL IMPACT EJECTA ON MARS SINCE THE HESPERIAN.** K. E. Wrobel and P. H. Schultz, Department of Geological Sciences, Brown University, Box 1846, Providence, RI 02912-1846 (Kelly\_Wrobel@brown.edu).

**Introduction:** Dark regions of Mars remain enigmatic. Are they unweathered volcanics? Pyroclastics? Exposed bedrock? Even more enigmatic are the conflicting explanations from spectral studies. Recently it has been suggested that these dark areas may represent impact glasses (or even tektites) emplaced by a nearby crater [1]. However, consideration of the Coriolis force emplaced on ejecta in flight reveals that simple emplacement models are inappropriate. Previous studies have considered the effects of planetary rotation, or the Coriolis effect, on distal ejecta deposition on Mars [2-3] and Earth [4-6]. Results of such studies [2] showed that rotational effects are significant for Mars and thus need to be taken into consideration when mapping ejecta distributions.

Small particles of ejecta from major impacts have contributed to global surface materials on Mars. In conjunction with this global ejecta layer, the surface also displays these large, concentrated regions of dark materials composed of either enigmatic andesitic materials, such as in Acidalia (Type II) [7-8] or more mafic materials (Type I). The present study examines this issue further by estimating the total accumulations of possible glasses (distal materials) since the end of the Noachian.

**Background:** Previous models involving ejecta deposition do not completely account for the effects of planetary rotation. One major misconception is that the only required correction is a simple adjustment of the landing position of the ejecta latitudinally according to how much the planet rotated beneath the particle while in flight. Such an approach neglects angular momentum effects. The definition of the Coriolis force in equation form ( $-2m(\mathbf{\omega} \times \mathbf{v}_r)$  where  $m$  is the mass of the body,  $\mathbf{\omega}$  is the rotation rate of the body and  $\mathbf{v}_r$  is the velocity of the projectile) intrinsically incorporates angular momentum. By containing the equation of the Coriolis force directly in a series of detailed ballistic equations, this study presents an accurate model of all effects of planetary rotation on ejecta deposition.

Previous work [2] focused on displaying rotational effects on ejecta deposition by mapping out where prominent contributions of ejecta from individual craters should be observed. One particularly surprising result was the substantial accumulation typically found in the hemisphere opposite from impact. The Coriolis force causes a distinct trend to occur in the locations of ejecta deposition sites [2,4]. Such trends result in significant concentrations of deposits at rather unexpected

locations. Earlier results have shown that a single, 200 km sized crater could deliver meters of material to the pole opposite from the impact [2]. The present study shows how the cumulative effects of such concentrated deposits from a series of craters could have global implications.

**Approach and Results:** Trajectories of ejecta deposition sites have been mapped on surface projections of Mars for every Hesperian-aged crater (or younger) that is greater than 100 km in diameter (22 craters in total). These craters were chosen for this study because they would be the most likely to contribute to the dark materials on the surface. All ejecta were launched at 45° in order to model a radial, gravity-controlled excavation component. Ejecta-scaling models [9-10] were incorporated in order to estimate deposit thickness values and to plot ejecta contributions. Cumulative distribution maps have been produced to illustrate the global significance of the concentrated deposits that result from the Coriolis force.

Figure 1a shows contributions of late-arriving, distal ejecta in the northern hemisphere from craters in the southern hemisphere. Two particular regions stand out (marked on Figure 1a). Comparison of this image with the map of Mars below it (Figure 3) shows that these regions of enhanced deposition of distal clasts approximately coincide with areas of dark, concentrated materials.

Figure 1b displays the total ejecta contributions to the northern hemisphere from all of the craters in this study. The concentrations shown in image 1b are saturated with the ejecta from the northern hemisphere craters. Thus, the thickest sequences (shown in red, yellow and green) represent primarily proximal ejecta deposits.

One can see that the two regions of enhanced deposition exhibited in Figure 1a do not completely fall into the regions of major contributions from the northern craters. Due to their proximity, the craters in the northern hemisphere will dump material into the two labeled regions. However, the important aspect is that the southern craters will still be supplying a substantial amount of the ejecta (up to 50% in some regions) that one should expect to find at these two particular areas. Also, the ejecta that is being deposited in these regions from the southern hemisphere craters (Figure 1a) will be glass-rich, distal ejecta that, on average, will arrive later than any proximal (not necessarily glass rich)

deposits from the nearby craters in the northern hemisphere (Figure 1b).

The image in Figure 2a shows distal, glass-rich ejecta contributions to the southern hemisphere of Mars from large, young northern hemisphere craters. Again, distinct regions show enhanced deposition. These regions coincide with parts of Syrtis Major Planum (region 1) and Hesperia Planum (region 2), two very significant zones of dark materials on the surface.

Figure 2b displays the cumulative ejecta contributions to the southern hemisphere from both the southern and northern hemisphere craters. This image primarily shows the focus of the deposit sites from the southern hemisphere craters. Due to their proximity, such deposits will saturate the image. These deposits are again proximal (not necessarily glass-rich) deposits.

These thickest deposits emplaced from the southern hemisphere craters (Figure 2b) do not coincide with the regions of enhanced deposition shown in Figure 2a. Thus, the cumulative material expected in these numbered regions (couple of meters in thickness) will contain a significant quantity of distal, glass-rich ejecta from craters from the opposite hemisphere. Again, as was the case for the northern hemisphere, these distal ejecta deposited from the northern hemisphere craters will be late-arriving and thus will be emplaced on top of any proximal deposits from the nearby craters. In fact, the northern craters will deliver ~1m of material to Syrtis Major Planum and up to 10 meters of ejecta to regions of Hesperia Planum.

**Discussion:** Previous studies [2,4,11] demonstrated that rotational effects are latitudinally dependent. Regardless of latitude, deposition sites of ejecta “wrap” in the hemisphere opposite from impact resulting in regions of enhanced ejecta emplacement. This wrapping trend will occur around the opposite pole for high-latitude impacts and equatorially for low-latitude impacts [2,4]. Focusing on high-latitude impacts, these results imply that larger sized craters could bring a concentration of late-arriving ejecta to unexpected locations at the pole opposite from impact resulting in regions of enhanced deposition similar to those shown near the equator in Figures 1a and 2a. When considering high-latitude craters in a cumulative sense, the amount of unexpected material that may build up at the pole opposite from such impacts may be significant enough to propose an alternate hypothesis to the origin of the dark materials found at the poles. All of the high-latitude southern hemisphere craters used in this study would deliver a cumulative concentration of ~53 m of material to 65°N and poleward. Approximately the same was found to be true of the amount of mate-

rial delivered to the south-polar region from high-latitude northern hemisphere impacts (~49 m of deposits).

Radial decay laws do not provide completely accurate predictions of the distributions of ejecta from a crater. Previously, attempts to map possible ejecta contributions to the dark materials found at regions such as Syrtis Major Planum and Hesperia Planum would focus on mechanisms of emplacement from direct components of ejecta from large, nearby craters. It was not expected that the craters farther away in the opposite hemisphere could be contributing a substantial amount of ejecta to such regions. However, rotational effects on ejecta emplacement cause this to occur. Regions of enhanced deposition in unexpected locations build up to the extent that when considering the cumulative effects of many craters, the hypothesis of an ejecta-based origin for concentrated regions of dark materials seems very plausible.

There are other manners in which large concentrations of ejecta may be focused at particular, unexpected regions of deposition, contributing to an area of dark materials.

*Plume Driven/Entrained Ejecta.* If a target surface of an impact on Mars happens to be particularly susceptible to shock heating, some vaporization may occur. Ejecta launched at angles greater than 45° from the horizontal can be useful as a first-order estimate of ejecta trajectories from a possible early-time vapor phase. In Figure 4, the effect of the Coriolis force on the deposition of plume driven/entrained ejecta is shown. This figure shows deposition sites of ejecta that have been launched at an angle of 80° from the horizontal from the Lyot crater (220 km crater at 50°N, 331°W). Deposition is severely limited immediately east of the crater and greatly enhanced west of the crater as a direct result of the rotational effects.

A thin global layer of ejecta may result from deposition from a vapor plume, analogous to the K/T boundary. A localized concentrated region of deposits (meters thick in some areas) is not expected. This is exactly what occurs, however, due to the Coriolis effect on the deposition of plume-entrained ejecta. The region west of the Lyot crater that will receive an enhanced concentration of deposits coincides with Acidalia Planitia, another large area of dark materials on the surface of Mars.

*Impact Basins:* Basins such as Hellas, Chryse, and Isidis are going to deposit enormous amounts of ejecta all over the surface of Mars. Rotational effects will play a role in the location of the deposition sites of these ejecta. Unexpected regions of enhanced accumulations will occur. In the case of basins, such accumulations could amount to hundreds of meters of ma-

terial being deposited at unpredicted locations. It is difficult to map exactly where such enhanced deposition may occur due to the old age of the impact basins. The pole that was present at the time of their formation may not coincide with the present polar location [12]. Future work is necessary in order to assess the paleogeographic coordinates of the basins and the resulting locations of greater ejecta deposition.

**Conclusions:** The Coriolis force created by the rotation of Mars has some rather significant effects on the cumulative build up of deposits from craters. The total contribution of impact glass deposits through time could be a plausible source for the dark materials found in concentrated areas on the surface. Due to rotational effects, craters in the opposite hemisphere tend to focus distal ejecta deposition to specific locations. Direct proximal ejecta deposited in the same hemisphere as the source crater (predominantly displayed in Figures 1b and 2b) may not be very glass-rich due to the proximity of the crater to the deposits. However, any ejecta that are brought to the regions of dark materials from craters in the opposite hemisphere will consist of late-arriving distal deposits that could be very glass-rich.

**References:** [1] Schultz P. H. and Mustard J. F. (2001) *LPS XXXII*, Abstract #1668. [2] Wilbur K. E. and Schultz P. H. (2002) *LPS XXXIII*, Abstract #1728. [3] Lorenz R. D. (2000) *Icarus*, 144, 353-366. [4] Wrobel K. E. and Schultz P.H. (2003) *LPS XXXIV*, Abstract #1190. [5] Kring D. and Durda D. (2002) *JGR*, 107, 10,1029/2001JE001532. [6] Alvarez W. et al. (1995) *Science*, 269, 930-935. [7] Bandfield J. L. et al (2000) *Science*, 287, 1626-1630. [8] Christensen P. R. et al (2001) *JGR*, 106, 23823-23871. [9] Housen K.R. et al. (1983) *JGR*, 88, 2485-2499. [10] O'Keefe J.D. and Ahrens T.J. (1977) *Proc. Lunar Sci. Conf. 8<sup>th</sup>*, 3357-3374. [11] Dobrovolskis A. (1981) *Icarus*, 47, 203-219. [12] Schultz P. H. (1985) *Sci. American*, 253, 94-102 [13] <http://www1.las.es/~amil/ssystem/hires/mars.jpg>.

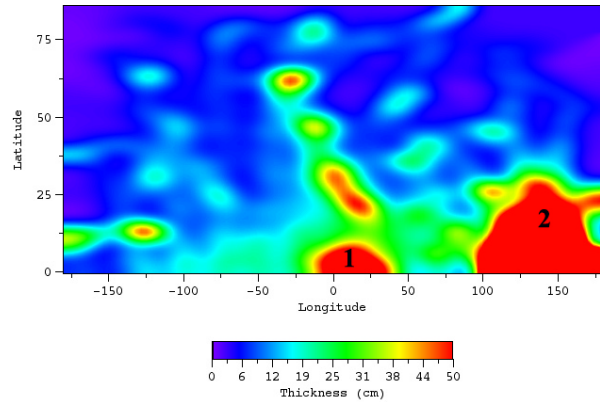


**FIGURE 1a:** This image displays the cumulative ejecta contributions to the northern hemisphere of Mars from Hesperian-aged (or younger) **southern hemisphere** craters of 100 km diameter or greater. Due to the source craters for these accumulations being located in the opposite hemisphere, the deposits shown are primarily late-arriving distal (glass-rich) materials. The two numbers distinguish regions of enhanced deposition that occur as a direct result of rotational effects on ejecta emplacement.

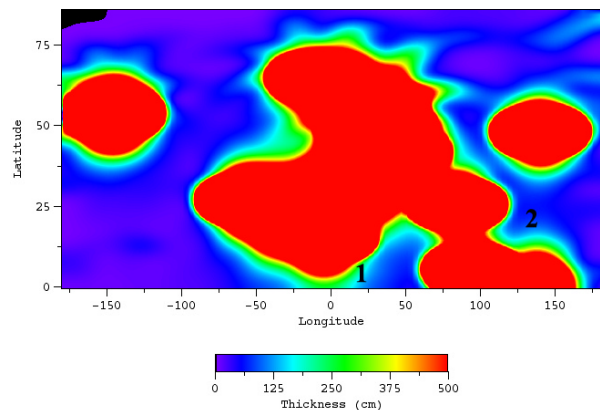


**FIGURE 1b:** This figure shows the cumulative ejecta contributions to the northern hemisphere of Mars from **all** (those located in both the southern and northern hemisphere) Hesperian-aged (or younger) craters of 100 km diameter or greater. The thickest sequences are saturated with proximal deposits (not necessarily glass-rich) from local craters (northern hemisphere craters). The two numbers mark the two regions of enhanced deposition of ejecta from southern hemisphere craters as illustrated in Figure 1a.

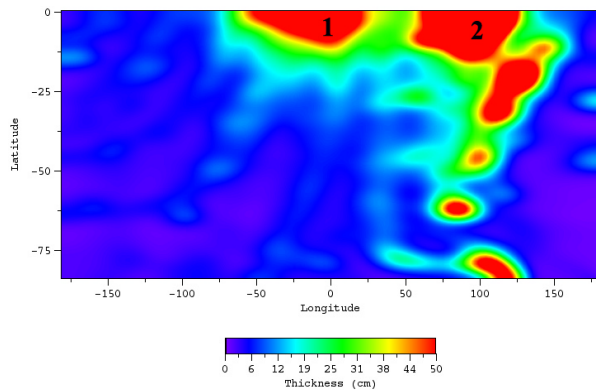


**FIGURE 2a:** This image shows the cumulative ejecta deposits brought to the southern hemisphere from Hesperian-aged (or younger) craters of 100 km diameter or greater located in the **northern hemisphere**. Due to the source craters of these deposits being located in the opposite hemisphere, the majority of material mapped in this image would consist of late-arriving distal ejecta (glass-rich). The two numbers label significant regions of enhanced deposition that occur as a direct result of rotational effects on ejecta emplacement.

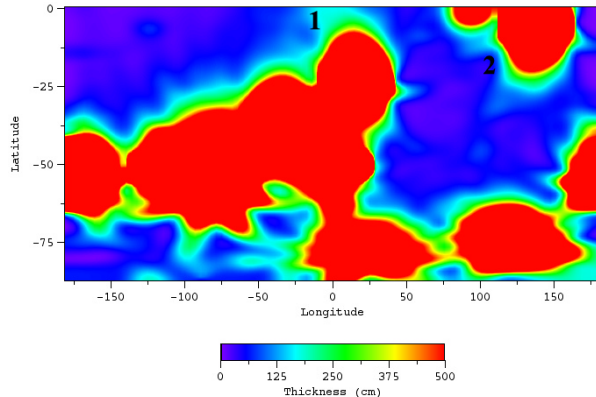


**FIGURE 2b:** Shown in this figure is the cumulative contribution of ejecta deposited in the southern hemisphere from **all** (those located in both the southern and northern hemisphere) Hesperian-aged (or younger) craters of 100 km diameter or greater. The deposits mapped are saturated with proximal deposits (not necessarily glass-rich) from the southern hemisphere craters. The two numbers mark the regions of enhanced deposition of distal ejecta from northern hemisphere craters as illustrated in Figure 2a.

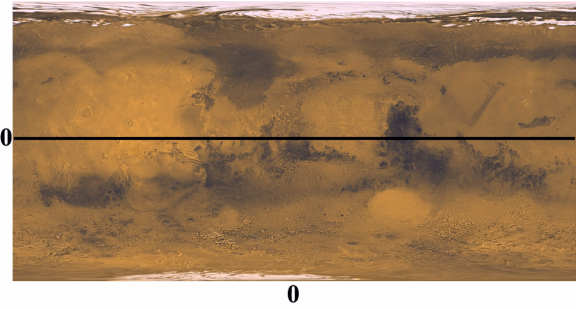


**FIGURE 3:** Shown is a full global image of the surface of Mars [13]. The main purpose for the inclusion of this image is to display the dark concentrated regions that are visible on the surface. Comparison of this image with Figures 1 and 2 show strong coincidences between the locations of these dark materials and the areas of enhanced deposition of distal ejecta resulting from rotational effects.

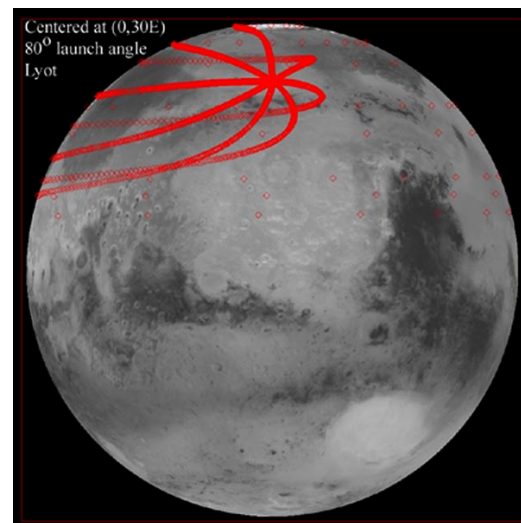


**FIGURE 4:** This image illustrates the deposition sites of ejecta launched at 80 degrees from the horizontal from the Lyot crater (220 km crater at 50°N, 331°W). Ejecta launched at high angles can serve as a first-order estimate of ejecta that is entrained in a vapor plume. Rotational effects result in limited deposition immediately east of the crater and enhanced ejecta emplacement west of the crater, possibly leading to large, local accumulations.

**BASALT, ALTERED BASALT, AND ANDESITE ON THE MARTIAN SURFACE: OBSERVATIONS, INTERPRETATIONS, AND OUTSTANDING QUESTIONS.** M. B. Wyatt<sup>1</sup>, H. Y. McSween, Jr.<sup>2</sup>, P. R. Christensen<sup>1</sup>, and J. W. Head III<sup>3</sup>, <sup>1</sup>Department of Geological Sciences, Arizona State University, Tempe, AZ 85287 (michael.wyatt@asu.edu), <sup>2</sup>Department of Geological Sciences, University of Tennessee, Knoxville, TN 37919, <sup>3</sup>Department of Geological Sciences, Brown University, Providence, RI 02912.

**Introduction:** To classify a volcanic rock accurately, and distinguish it from an altered volcanic surface or sedimentary rock of similar composition, one must utilize an assortment of chemical, mineralogical, and textural analyses. Questions and uncertainties in classifications can arise without a full suite of such measurements as some mineral phases and chemical trends alone are not discriminating factors for assigning petrologic names. Such difficulties are common when classifying rocks on Mars using in-situ and orbital remote sensing techniques because of a lack of chemical, mineralogical, and textural measurements at comparable spatial and spectral resolutions. We can, however, add a perspective to improve our understanding of the origin and composition of martian surface materials by placing existing compositional measurements into newly emerging geologic contexts.

The purpose of this work is to summarize current observations and interpretations of martian low-albedo surface compositions, focusing on those derived from the Mars Global Surveyor Thermal Emission Spectrometer (MGS-TES) experiment, and place them into geologic contexts relevant to mapped distributions. Outstanding questions pertaining to the origin and composition of martian low-albedo surface materials are discussed and ongoing work to address these issues is presented.

**Background:** Prior to MGS-TES, measurements of mineral and bulk rock chemistries have led to a variety of interpretations of the surface composition of martian low-albedo regions.

*Orbital Remote Sensing.* Visible/near-infrared spectroscopic data of some martian low-albedo regions, interpreted to be composed of rock and residual dark soil, are characterized by ~1 and 2- $\mu\text{m}$  absorptions that are commonly attributed to the presence of ferrous iron ( $\text{Fe}^{2+}$ ) in the form of pyroxene and hematite (both nanophase and crystalline) [e.g., 1-4]. Based on these observations, Phobos-2 ISM spectra of Syrtis Major have been interpreted to represent two-pyroxene basalts similar to basaltic shergottite meteorites [5]. A different perspective suggested by [6] attributes the observed signatures in dark regions to lesser amounts of pyroxene plus dark altered materials that are more consistent with the observation of a 3- $\mu\text{m}$  water band in intermediate to low albedo regions. High-resolution

telescopic spectra of Acidalia Planitia [7] exhibit weaker mafic mineral bands compared to Syrtis Major which may be consistent with the presence of basaltic glass and/or surface coatings.

*In-situ Measurements.* Mars Pathfinder rocks were determined to be chemically similar to andesite based on alpha proton X-ray spectrometer (APXS)-measured element abundances [8], but textural and visible/near-infrared multispectral evidence supporting the hypothesis that these rocks are volcanic is more ambiguous [9]. A sedimentary origin or surface coating could thus not be ruled out without textural or mineralogical data. A re-analysis of APXS chemistry indicates that Pathfinder rocks may in fact have a high water content, which supports a non-igneous classification [10]. Furthermore, soil compositions at the Viking and Mars Pathfinder landing sites were compared by [11] and it was concluded that the global dust formed by weathering of basalt rather than andesite.

**MGS-TES: Mineral Abundances and Bulk Oxides:** Studies of low-albedo regions on the martian surface using atmospherically corrected thermal emissivity data from the Mars Global Surveyor Thermal Emission Spectrometer (MGS-TES) have identified two distinct global surface spectral signatures [12-15]. The Surface Type 1 (ST1) spectral end-member has been interpreted as an unaltered basalt characterized by high deconvolved modal abundances of plagioclase and clinopyroxene [12-13, 16]. The Surface Type 2 (ST2) spectral end-member has been variously interpreted as an unaltered andesitic composition (basaltic andesite to andesite) [13, 16] or partly altered basalt [17]. The unaltered andesitic composition is characterized by high deconvolved modal abundances of plagioclase and high-silica volcanic glass [13, 16]. The partly altered basalt is characterized by high deconvolved modal abundances of plagioclase and alteration phases (sheet silicates, K-feldspar, and silica coatings) and low modal pyroxene [17]. Detectable abundances of hematite [e.g. 18], orthopyroxene [e.g. 19], and olivine [e.g. 19] have also been identified in regional and local occurrences where ST1 basaltic compositions dominate surface units. The identification of these phases may represent unique surface lithologies (i.e. dunite), or higher abundances of each phase in a basaltic surface unit (i.e. olivine bearing basalt).

Although TES is a mineralogical tool, bulk rock geochemistry can be derived from deconvolved modal mineralogies by combining the compositions (wt. % oxides) of spectral end-members in proportion to their relative modes. Estimated ST1 and ST2 chemical compositions [20] from deconvolutions derived using modified spectral end-member sets of [13,16-17, 21] were shown to be very similar in their overall respective bulk chemistries. Assuming an igneous composition for both ST1 and ST2 lithologies, [20] suggested that ST2 andesites might have formed by fractional crystallization under hydrous conditions of a ST1 basaltic andesite parent magma. The required H<sub>2</sub>O for this is intriguing because such high contents are typically found only in terrestrial subduction zone environments and are in contrast with predicted martian mantle volatile contents. Assuming an igneous composition for ST1 and an altered composition for ST2, [20] also suggested that weathering of ST1 could produce sediments with ST2 compositions. Neither surface type was shown to be compositionally similar to basaltic shergottites or the global dust, but dust formation was shown to be possible by the addition of iron-oxides to ST2.

*Terrestrial Examples.* The cut surfaces of Deccan and Columbia River flood basalts are terrestrial examples of rocks with similar spectral shapes, deconvolved mineral abundances, and derived bulk rock chemistries compared to the ST1 spectral end-member [12-13, 16]. The flood basalt samples contain phenocrysts of plagioclase and pyroxene in a microcrystalline groundmass of the same phases and have bulk silica and alkali values which classify them as subalkaline basalt-basaltic andesites (49.5-51.7 wt% SiO<sub>2</sub> and 3.2-4.1 wt% Na<sub>2</sub>O+K<sub>2</sub>O) [22]. The cut surface of a continental arc-andesite from the Medicine Lake Highlands and a partly altered Columbia River flood basalt surface (whose cut surface is the same as the CRB sample above) are terrestrial examples of rocks with similar spectral shapes compared to the ST2 spectral end-member [13, 16, 17]. The Medicine Lake Highland sample contains small amounts of plagioclase and pyroxene phenocrysts with a glassy to microcrystalline-intergranular groundmass composed of the same phases and has bulk silica and alkali values which classify it as a subalkaline andesite (57.2 wt% SiO<sub>2</sub> and 5.15 wt% Na<sub>2</sub>O+K<sub>2</sub>O) [22]. The partly altered Columbia River flood basalt surface contains small amounts of plagioclase and pyroxene and secondary products interpreted as amorphous silica and sheet silicates (Fe-smectite and Ca-montmorillonite) [22].

*Mapped Distributions of Surface Compositions.* The distribution of the ST1 unit (basalt) is restricted to southern highlands and Syrtis Major regions that are of

Noachian or Hesperian age and a few local deposits in the northern plains [13, 23]. The ST2 unit (andesitic and/or altered basalt) displays the highest concentrations in the younger Amazonian-age northern lowlands regions of Acidalia Planitia and the circumpolar sand seas [13]. ST2 compositions are also present in moderate abundances, or an intermediate composition, throughout the low-albedo highlands south of ~ 40°S with higher concentrations in several isolated regions south of Solis Planum, southeast of Hellas Basin, and along the edge of the southern polar cap [13, 21]. The distribution of the highest concentrations and largest extents of the two surface spectral units is thus split roughly along the planetary dichotomy which separates ancient, heavily cratered crust in the southern hemisphere from younger lowland plains in the north. However, intermediate compositions and/or mixing of units and isolated regions are also present [13, 21].

**Outstanding Questions:** The initial ambiguity in interpreting the ST2 lithology from deconvolved mineral abundances and laboratory rock spectra arose because volcanic siliceous glass (a major component of andesite) was shown to be spectrally similar to some alteration phases (sheet silicates and suggested silica coatings) over the spectral ranges used in deriving the atmospherically corrected ST1 and ST2 spectral end-members [17]. Absorption features between 500-550 cm<sup>-1</sup> in laboratory spectra distinguish sheet silicates from high-silica volcanic glass; however, this region was excluded while deriving the ST1 and ST2 spectral end-members because the CO<sub>2</sub> atmosphere of Mars becomes largely opaque near this spectral region. The original interpretation of the high-silica glass spectral end-member phase as a primary volcanic glass was also shown to be too limited, as deconvolved modal abundances of the natural surface of a Columbia River flood basalt suggested it could also represent an amorphous high-silica alteration product [17]. Analyses by [24] have further shown that the addition of high-silica alteration coatings on basalts results in a surface that is spectrally similar to andesite. Recent work by [25] and [26] have shown additional alteration phases such as zeolites and palagonites to be spectrally similar to high-silica glass, thus adding to the possible range of mineral phases present in ST2 materials. Future work is needed to understand better the degree of substitution and spectral effects of varying crystallinity in amorphous phases over a range of chemical compositions as accurate deconvolution of mixture spectra is largely dependent on the input of spectral end-members that represent an appropriate range of compositions in the mixture.

**Geologic Context:** A perspective can be added to improve our understanding of the origin and composi-

tion of martian surface materials by placing existing compositional measurements and distributions of surface materials into newly emerging geologic contexts. An important but often overlooked perspective is that a single interpretation of spectra may not be warranted everywhere on Mars (Ockam wasn't always right). Here we focus on the distribution of TES derived ST2 materials in three different martian geologic environments: 1) northern lowlands, 2) north circumpolar sand seas, and 3) southern highlands.

*Northern lowlands.* The mapped distribution of ST2 in the northern lowlands is shown to be concentrated in Acidalia Planitia, part of the low-albedo surfaces of the Vastitas Borealis Formation (VBF) [13, 17]. The VBF makes up one of the largest surface units on Mars and was initially mapped on the basis of its morphologic and albedo characteristics and its occurrence below the martian highland/lowland boundary [27]. Volcanic, tectonic, glacial, periglacial, and sedimentary related processes have been attributed to various landforms observed in the unit [28-37 references therein].

The VBF plains have most recently been interpreted as sedimentary deposits derived from outside the basin [38] or altered sediments formed through local reworking of earlier deposits by permafrost processes [39]. The sediments are interpreted to be underlain by ancient ridged volcanic plains. Both of the VBF "new-view" theories propose these materials have undergone significant reworking by either transport and/or indigenous weathering and may support alteration of basaltic sands within this depocenter. The VBF morphology is characterized by a mixture of smooth plains, polygonal troughs and fractures, and pitted domes whose origins have been suggested to involve interactions between surface, and near-surface, volatile-rich material (water and/or ice) [38,39]. TES spectra of the VBF boundary in southern Acidalia Planitia, where it is not obscured by dust, indicate that the proportion of ST1 (unaltered basalt) material increases outside the basin [40].

Recent work by [41 and references therein] summarizes evidence for the probability of sedimentary silica existing on Mars and emphasizes the highly mobile nature of silica during near surface alteration of basaltic rocks under a wide variety of temperature, pressure, and fluid conditions. Palagonitization is a commonly proposed alteration process for the martian surface and the production of palagonites and secondary clays, both of which have been shown to be spectrally similar to high-silica volcanic glass, result in a high degree of silica mobilization [41 and references therein]. The geologic context of the VBF as a sedimentary basin with either transported or indigenous

materials having interacted with surface or near-surface volatile rich materials [38-39] supports an altered basalt classification for the TES ST2 unit in the northern lowlands.

*North circumpolar sand seas.* The largest continuous area of dunes on Mars are the transverse dune fields in the north circumpolar sand seas. Small simple barchan dunes and large mega-barchans also occur on the margins of the sand seas and in areas of thin sand cover. Observations of possible reversals of dune-forming wind directions suggest that these dunes are active today and there is evidence the dunes have some sources within the polar layered deposits.

The ST2 unit (andesitic and/or altered basalt) displays the highest concentrations in the northern lowlands regions of Acidalia Planitia and the circumpolar sand seas [13]. The north circumpolar sand sea environment is however very different from the northern lowland plains. It is very unlikely that weak alteration rinds or coatings (i.e. sheet silicates, palagonites, and zeolite) could persist on the primarily active north polar sands that are being constantly abraded. Silica coatings can however be resistant to mechanical weathering and may remain as coatings or cementing agents.

If polar dune fields are derived from polar layer deposits, they could represent basaltic compositions with resistant silica coatings. Conversely, the polar dune fields could be locally derived from an andesitic source or transported from a regional andesitic source. The presence of weak alteration rinds and coatings is very unlikely, leaving silica (coating vs. primary volcanic glass) as the likely phase contributing to the ST2 spectral shape.

*Southern highlands.* ST2 materials are present in moderate amounts, or as an intermediate composition, throughout the southern highlands with higher concentrated abundances occurring in several isolated regions south of Solis Planum, southeast of Hellas Basin, and along the edge of the southern polar cap [13, 21]. ST1 materials are also located in the southern highlands and Syrtis Major regions that are of Noachian or Hesperian age [13].

It has been shown that ST2 andesites might have formed by fractionation of ST1 basaltic andesite magma under hydrous conditions in the shallow martian crust based on TES derived bulk chemistry [20]. The required H<sub>2</sub>O for this is intriguing because such high contents are typically found only in terrestrial subduction zone environments and are in contrast with predicted martian mantle volatile contents. Although the addition of water to the martian mantle through subduction has not generally been advocated, [42] suggested that andesitic crust could have formed on

Mars through hydrous melting. In this model, mantle water is primordial, leading to an early crust of andesite with later dry, basaltic volcanism. Bimodal magmatism, leading to the production of siliceous melts from basaltic parent magmas, was argued by [43] to occur through the formation of lenses within solidification fronts. It is not obvious however that such a mechanism could operate on a global scale and produce volumetrically significant amounts of andesite. ST2 is an altered ST1 in the southern hemisphere, the observed distribution of materials could represent incomplete weathering. However, the southern highlands are old and heavily cratered with little evidence for resurfacing or interactions between surface or near-surface volatile rich materials. It is therefore very unlikely that the processes which resurfaced the northern lowlands are the same processes which affected the surface compositions of the southern highlands.

**Ongoing Work:** An outstanding question regarding deconvolved mineral abundances of ST1 and ST2 is the ability to distinguish alteration phases (sheet silicates, silica coatings, zeolites, and palagonites) from high-silica volcanic glass. The original TES atmospheric and surface spectral shapes were derived using conservative spectral ranges (233-508  $\text{cm}^{-1}$  and 825-1301  $\text{cm}^{-1}$ ) in part to avoid  $\text{CO}_2$  hot band and isotope features [13]. Absorption features between 500-550  $\text{cm}^{-1}$  in laboratory spectra distinguish some sheet silicates from high-silica volcanic glass. Silica coatings and some zeolites and palagonites do not exhibit the same distinctive spectral shapes as sheet silicates, and may be extremely difficult to distinguish from high-silica volcanic glass [24-26].

Current work is focused on re-deriving local TES atmospheric and surface spectral shapes at wavelengths that cover the diagnostic 500-550  $\text{cm}^{-1}$  range to determine if sheet silicates or other alteration phases (zeolites and palagonites) are identified or distinguished from high-silica volcanic glass. Atmospheric gas shapes ( $\text{H}_2\text{O}$  and  $\text{CO}_2$ ) have been accurately modeled by [44 and references therein] and are removed from spectra thus allowing a greater spectral range for deriving surface spectral shapes. New atmospherically corrected surface spectral shapes of the northern lowlands, north circumpolar sand seas, and southern highlands are being individually derived to examine spectral differences and similarities between the different geologic environments.

**References:** [1] Adams J. B. and T. B. McCord (1969) *JGR*, 74, 4851-4856. [2] Singer R. B. et al., (1979) *JGR*, 84, 8415-8426. [3] Morris R. V. et al., (1989) *JGR*, 94, 2760-2778. [4] Mustard J. F. et al., (1993) *JGR*, 98, 3387-3400. [5] Mustard J. F. and J.

M. Sunshine (1995) *Science*, 267, 1623-1626. [6] Calvin W. M. (1998) *GRL*, 25, 1597-1600. [7] Merényi, E. R. et al., (1996) *Icarus*, 124, 280-295. [8] Rieder R. et al., (1997) *Science*, 278, 1771-1774. [9] McSween H. Y. et al., (1999) *JGR*, 104, 8679-8715. [10] Foley C.N. et al., (2001) *LPSC XXXII*, Abstr #1979. [11] McSween H. Y. and Keil K. (2000) *GCA* 12, 2155-2166. [12] Christensen P. R. et al. (2000) *JGR*, 105, 9609-9622. [13] Bandfield J. L. et al. (2000) *Science*, 287, 1626-1630. [14] Bandfield J. L. et al. (2000) *JGR*, 105, 9573-9587. [15] Smith M. D. et al. (2000) *JGR*, 105, 9589-9609. [16] Hamilton et al. (2001) *JGR*, 106, 14733-14746. [17] Wyatt M. B. and McSween H. . (2002) *Nature* 417, 263-266. [18] Christensen P. R. et al., (2000) *JGR*, 105, 9632-9642. [19] Hamilton V. E. et al., (2002) *LPSC XXXIII*, Abs #1937. [20] McSween H. Y. et al., (2003) *LPSC XXXIV*, Abs # 1189. [21] Bandfield J. L. (2002) *JGR* 107 (E6), 10.1029/2001JE001510. [22] Wyatt M.B. et al. (2001) *JGR* 106, 14,711-14,732. [23] Rogers D. et al. (2001) *LPSC XXXII*, Abstr #2010. [24] Kraft M. D. et al. (2003) *LPSC XXXIV*, Abstr #1420. [25] Ruff S. W. and Christensen P. R. (2003) *LPSC XXXIV*, Abstr #2068. [26] Morris R. V. et al., (2003) *LPSC XXXIV*, Abstr #1874. [27] Scott D. H. et al., (1986-87) USGS Maps I-1802A, B, C. [28] Tanaka K. L. et al., (2003) *JGR*, 2002je001908, in press. [29] Scott D. H. et al., (1986-87) USGS Maps I-1802A, B, C. [30] Parker T. S. et al., (1989) *Icarus*, 82, 111-145. [31] Head J. W. et al., (1999) *Science* [32] Tanaka K. L. et al., (2001) *Geology*, 29, 427-430. [33] Kargel J. S. et al., (1995) *JGR*, 100, 5351-5368. [34] Kreslavsky M. A. and Head J. W. (2002) *JGR*, 107, 10.1029/2001JE001831. [35] Tanaka K. L. (1997) *JGR*, 102, 4131-4149. [36] Clifford S. M. and Parker T. J. (2001) *Icarus*, 154, 40-79. [37] McGill G. E. and Hills L. S. (1992) *JGR*, 97, 2633-2647. [38] Head J. W. et al. (2002) *JGR* 107(E1), 10.1029/2000JE001445. [39] Tanaka K.L. et al. (2003) *JGR*, in press. [40] Wyatt M. B. et al. (2003) *JGR*, in press. [41] McLennan S. C. (2003) *Geology*, v. 31, no. 4, 315-318. [42] Lowman P. D. (1989) *Precambrian Res.*, 44, 171-195. [43] Marsh B. D. (2002) *GCA*, 66, 2211-2229. [44] Bandfield J. L. and Smith M.D. (2003) *Icarus*, 161, (47-65).

## H<sub>2</sub>O-SILICATE MICROPHYSICS IN ASCENDING VOLCANIC PLUMES ON MARS A. P. Zent, NASA Ames Research Center, Moffett Field, CA, 94035, Aaron.P.Zent@nasa.gov

Physical adsorption of water vapor plays a much more significant role in eruptive plume energetics on Mars than on Earth. The total surface area in martian plumes is likely comparable to terrestrial ash, while the erupting magma and ambient atmosphere are drier. Plumes cool rapidly during ascent, and a limited population of H<sub>2</sub>O molecules find adsorption sites to be increasingly stable. Release of latent heat of condensation and the onset of moist convection are diminished, delayed, or even prevented by adsorptive interaction

We have developed a 5-component numerical model of the behavior of water in eruptive plumes under Mars-like conditions. We have used the model to study the fate of both juvenile and ambient atmospheric water in the eruption column. Here we investigate the adsorptive interaction of water and silicates as they effect plume dynamics and the partitioning and distribution of H<sub>2</sub>O to the martian environment.

Our focus is on the role of adsorption in scavenging H<sub>2</sub>O from the ascending eruption column, and the possibility that adsorptive scavenging depresses the vapor pressure in the column below the level considered in most eruptive models.

There has been an increasing recognition of likely airfall and pyroclastic deposits from explosive volcanism, both on ancient highland volcanoes and in the Tharsis complex [1,2,3,4,5,6]. Further, the nature of martian volcanism appears to be increasingly explosive in older terrains [7], where a number of explosive or multi-genetic volcanoes show evidence of channeling on their flanks. For example, Noachian channels in the Thaumasia and Coprates region tend to originate on volcanoes, or close to rifts, both of which could provide a supply of warm H<sub>2</sub>O [8].

A number of sites have exhibit evidence of airfall deposits, some of them seemingly volatile rich. The Medusae Fossae Formation (MFF) is one example of a potential volcanic airfall deposit. Many hypotheses for the formation of the unit have been proposed. Sakimoto et al., [9] however find that the members of the MFF are not simple, planar strata, but are consistent with eolian or volcanic deposits superposed on top of existing topography.

Grizzaffi and Schultz [10] suggested that the interior plains of the Isidis impact basin reflect the deposition and subsequent removal of a thick layer of material within the basin. They suggested that the deposits contained a significant volatile fraction based on comparison to terrestrial analogs. They

argued that ablation of stagnant debris-laden ice cover produces landforms on Earth similar to those observed in Isidis.

In addition to further documentation of unconformable, volatile-rich deposits northwest of Isidis, Grant and Schultz [11] mapped similar deposits in the Electris region of Mars. Electris also displays unconformable deposits with thick, poorly-defined layering on the order of tens to hundreds of meters. The deposits had locally high volatile content, based on the observation that relatively young valley networks that dissect portions of the deposit are entirely confined within it, and hence an intra-deposit source of water is inferred.

Microphysical interactions determine how water behaves in the plume and, through release of latent heat, effect plume energetics and sedimentation [12]. The surface properties of ash are altered by condensation, which increases agglomeration and speeds precipitation. Although other workers have investigated the interaction of H<sub>2</sub>O and silicates in rising plumes, both on Earth and Mars [12,13,14], they have not considered the possible interaction of H<sub>2</sub>O and silicates via adsorption; no vapor is removed from the plume until saturation is reached.

Our model is based on Glaze and Baloga [15]. We have expanded their model by allowing H<sub>2</sub>O to exist as vapor, unfrozen water (adsorbate or bulk liquid), and ice. We use the scheme shown in

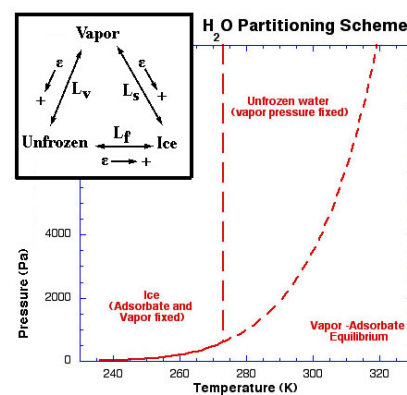


**Fig. 1.** H<sub>2</sub>O partitions between physical adsorption and the vapor phase. If liquid is stable, the vapor pressure is set, and all remaining H<sub>2</sub>O is in the liquid phase. If ice is present, the vapor and unfrozen phases are set by temperature and the ice vapor pressure. Latent heat is released in the direction indicated by the arrows in the inset.

Figure 1 to determine the distribution of H<sub>2</sub>O among phases. Unfrozen water exists in all fields. If the plume is in the vapor field, the total H<sub>2</sub>O is partitioned between the adsorbed and vapor phases such that the adsorption isotherm is satisfied. Because we do not know the adsorptive response of primary martian ash, we assume here the basalt adsorption isotherm reported by Fanale and Cannon [16].

$$\rho_a = \frac{\gamma P^{0.51}}{\exp(\delta / T)}$$

where  $\gamma = 2.09 \times 10^{-12}$  kg H<sub>2</sub>O Pa<sup>-1</sup> m<sup>-2</sup> and  $\delta = -2679.8$  K.

If the plume element is in the unfrozen phase domain, all remaining vapor is assumed to condense to liquid, and the presence of liquid sets the vapor pressure in the plume element. When the plume reaches the freezing point, most of the remaining water is frozen, although a small amount of unfrozen water always remains, in equilibrium with the temperature and vapor pressure over ice.

The plume model itself conserves silicate mass, H<sub>2</sub>O mass, CO<sub>2</sub> mass, momentum and energy throughout the convective rise height. It assumes that ambient atmosphere is entrained at a rate proportional to the rise velocity ( $u$ ) of the plume.

The background atmosphere into which the eruptions occur is a significant control on the evolution of the plume [15]. In the model runs explored here, we will assume that Noachian conditions, and a total atmospheric pressure of  $8 \times 10^4$  Pa (800 mbar). We assume a plausible thermal profile that is valid up to at least 10 km (-4.78 K/km) based on a radiative-convective model [17] (the thermal gradient near the surface is independent of pressure, although the surface temperature is not).

The size frequency distribution of the plume material is specified by the user. We assume that the size frequency distribution of the particles is log-normal. Therefore, in practice, the user specifies the mean and standard deviation of the population.

There are no measurements of the size frequency distribution of silicates in ascending Plinian eruption plumes.

The surface area of martian ash, as produced, is unknown. It is certainly variable among volcanoes on Earth, and between eruptions, even eruptive phases of the same volcano. Therefore, no prescription can be made for this key variable. It will be explored numerically.

One effect that is certainly understood is that the relative importance of internal surface area (cracks, irregularities, vesicles, etc.) becomes greater for

smaller particles. The largest particles (cm-scale) have surface areas not much greater than would be expected from their geometric dimensions. Smaller particles however have significantly greater surface area, as measured in standard surface area test such as the BET test. We explore the effects of different size-frequency

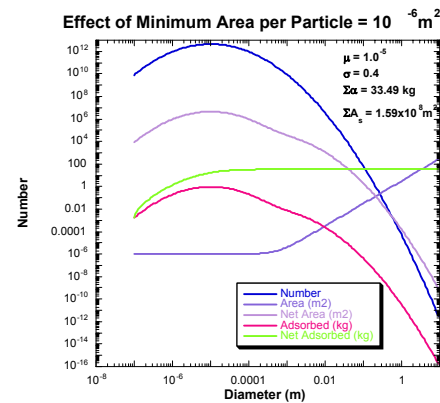


**Fig. 2** Mean grain size is 10  $\mu\text{m}$ , and  $\sigma = 0.4$  for a log-normal distribution. The surface area is approximately geometric, although a minimum area of  $10^{-6} \text{ m}^2$  is assumed for each particle.

distributions and specific-surface area v. grain size relationships. One example is shown in Figure 2, which will be the nominal case for this study.

The adsorptive calculation partitions the total amount of water in each element, which represents the erupted+entrained water, according to Eq. 1, across the surface area available in the log-normal distribution specified by the user (e.g. Fig. 2).

The sensitivity of adsorptive scavenging in the ascending cloud, to particle size frequency distribution can be explored with this adsorptive subroutine. We define a parcel of silicates and H<sub>2</sub>O, and allow that parcel to cool, monitoring the total H<sub>2</sub>O remaining in the vapor phase. In this case, we have defined  $10^7$  kg of silicates in the test volume, with a log-normal size-frequency distribution, a mean grain size of  $10^{-5}$  m, and a minimum of  $10^{-6} \text{ m}^2$  per particle. This is based on observations of terrestrial ash particles that reveal enormous internal surface area. We assume  $10^5$  kg of H<sub>2</sub>O ( $\approx 1$  wt%). The results of this study show significant dependence of the H<sub>2</sub>O sequestered in the adsorbed phase. In Figure 3, we show the effects of varying the standard deviation ( $\sigma$ ) of the log-normal size frequency

distribution from 0.2 to 0.4. During cooling of a parcel, a sharply-peaked ( $\sigma = 0.2$ ) distribution will adsorb considerably more water than a broad ( $\sigma = 0.4$ ) distribution. For the surface area distribution and adsorption isotherm assumed here, approximately 80% of the total water is adsorbed by a  $\sigma=0.2$  distribution in cooling to the liquid condensation temperature, and only about 1% by a  $\sigma = 0.4$  distribution. This indicates that the partitioning of  $H_2O$  is a sensitive function of the total silicate area in ascending plume. Latent heat of adsorption would be released gradually in the  $\sigma = 0.2$  plume, with only 20% of the original  $H_2O$  available for rapid condensation to liquid, the process that initiates moist convection in ascending plumes. Virtually all  $H_2O$  remains in the vapor

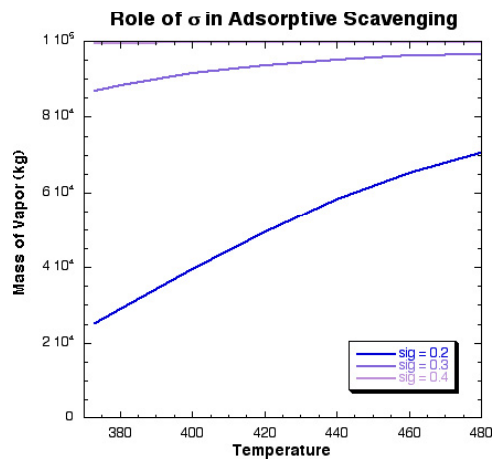


**Fig. 3.** Only about 20% of the initial  $H_2O$  remains in the vapor phase after cooling to 373K when surface area is large ( $\sigma=0.2$ ), but virtually all remains as vapor when  $\sigma = 0.4$ . Where the condensation temperature is  $< 373K$ , the discrepancy is more extreme than shown here.

phase in the  $\sigma = 0.4$  plume.

The plume model is initialized by specifying the initial velocity of the plume at the volcano throat, the radius of the plume, the initial volatile content (assumed to be  $H_2O$ ) and the temperature. We assume that the volcanic gases are not overpressured at the base (i.e. the plume internal pressure is identical to atmospheric ambient), and assume that the silicate particles have a density of  $2600 \text{ kg m}^{-3}$ . This assumption may be inaccurate if the silicate material traps significant gas.

These assumptions are adequate to calculate the mass eruption rate of the individual plume components, silicate and  $H_2O$ , as well as the bulk plume density. The initial phase distribution of the  $H_2O$  is calculated via the phase partitioning calculation described above.

For comparison, we refer to a standard plume, which we specify as  $R_0 = 10\text{m}$ ;  $V_0 = 200 \text{ m s}^{-1}$ ;  $T_0$

$= 525 \text{ K}$ . The rise of a 1 wt %  $H_2O$  ash plume is integrated from the ground upwards via a Runge-Kutta technique.

The behavior of the nominal plume under Noachian conditions is similar to that predicted by other workers (Fig. 4). The plume ascends to approximately 14.5 km. The plume is carried past its neutral buoyancy height (NBH) by momentum. The model assumptions begins to break down near the top of the plume, as the vertical velocity of the plume becomes small. Therefore, precise prediction of the umbrella region of the column is not included in this model.

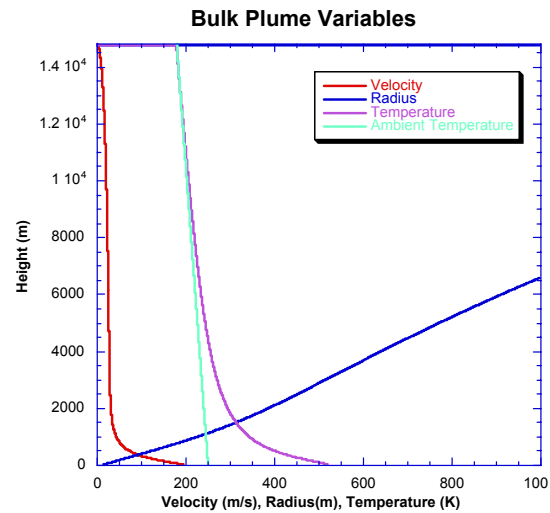


**Fig. 4.** The nominal plume behaves similarly to predictions from other workers.

We next examine the role of varying grain size. The ambient atmosphere is assumed to be dry in this calculation. The standard deviation of the size frequency distribution of the silicate materials is varied to establish the limits of qualitatively similar behavior.

An interesting result is shown in Figure 5. We plot, in blue, the path followed by the vapor pressure curve for two different size-frequency distributions, as they move from high temperature and pressure (upper right), to lower  $T$  and  $P$  (lower left). For both distributions, the mean grain size is  $10 \mu\text{m}$ . We vary the standard deviation of the log-normal size frequency distribution from  $\sigma = 0.3$  (sharply-peaked distribution) to  $\sigma = 0.4$  (somewhat more broadly-peaked distribution).

When the standard deviation of the size frequency distribution is 0.4, the initial conditions ( $T_0 = 525 \text{ K}$ ,  $r_0 = 10\text{m}$ ) force the plume into the superheated liquid phase, even at temperatures well above 373K. The vapor-pressure history follows exactly

the vapor pressure curve (dashed blue line). However, if  $\sigma = 0.3$ , then adsorptive equilibration depresses the vapor pressure in the plume, preventing condensation to liquid in the ascending plume, and inhibiting the latent heat release that initiates moist convection. The vapor pressure remains below the saturation pressure throughout plume ascent.

Selection of plausible values for the variables of choice indicates that Martian volcanoes may be near the boundary between two qualitatively different behaviors. The degree of water in the magma probably won't vary by more than a factor of 2, but doubling the magma  $H_2O$  content to 2 wt % saturates available silicate surface area, and a  $\sigma=0.3$  plume condenses liquid just as a  $\sigma = 0.4$  plume.

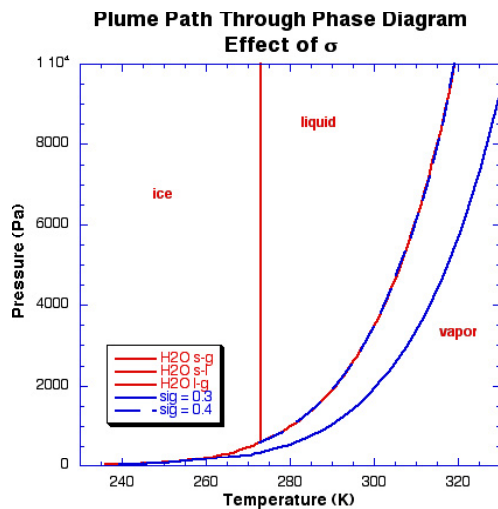


**Fig. 5** More surface area per unit mass in the silicate component of the plume adsorbs more water. In this simulation, adsorption prevents the plume from ever entering the liquid  $H_2O$  field when  $\sigma$  is reduced from 0.4 (dashed blue line following phase boundary) to 0.3 (solid blue line).

There are additional uncertainties in the model result presented here. For example, simple physical adsorption is unlikely to be the only interaction between  $H_2O$  vapor and the ascending ash. Direct chemical interaction will irreversibly remove some  $H_2O$  from the plume, producing alteration of the ash. The adsorptive behavior of hot ash particles is unknown, and the adsorption isotherm used here is extrapolated outside the domain in which it is experimentally verified.

The actual size frequency distribution of the silicate material as it is erupted is unknown, as is the specific surface area of the ash particles. The behavior of the plume is extraordinarily sensitive to these variables, since the distribution of available  $H_2O$  on the available surface area controls latent heat release and plume energetics.

Entrainment of ambient atmosphere with  $H_2O$  will also tend to increase adsorptive coverage, and lead to condensation of liquid-phase  $H_2O$ . However, even in the terrestrial tropics, plume ascent can do no more than triple the initial  $H_2O$  content [14]. Therefore, a cold-dry Martian atmosphere may not hold enough  $H_2O$  to saturate in an ascending plume with high surface area. Under warmer, wetter conditions, adsorptive scavenging is less likely to prevent condensation, perhaps leading to enhanced agglomeration and sedimentation of volatile-rich deposits near the source.

#### References:

- [1] Gregg et al., LPSC 33, abs. 1560, 2002; [2] Hynek et al., LPSC 33, abs. 1408, 2002; [3] Mouginiis-Mark abs. 1407, 2002; [4] Tanaka and Leonard, *JGR*, **100**, 5407-32, 1995 [5] Greeley and Crown, *JGR*, **95**, 7133-49, 1990, [6] Crown and Greeley, *JGR*, **98**, 3431-3451, 1993 [7] Stewart and Head, *JGR*, **106**, 17505-17513, 2001, [8] Tanaka et al, *JGR*, **103**, 31407-19 1998, [9] Sakimoto et al., *JGR*, **104**, 24141-24154, 1999 [10]Griffazi and Schultz, *Icarus*, **77**, 358-381, 1989; [11] Grant and Schultz, *Icarus*,**84**, 166-195, 1990; [12] Herzog et al., *J. Volcan. Geotherm. Res.*,**87**, 55-74, 1998; [13] Hort and Weitz, *JGR*, **106**, 20547-20562, 2001; [14] Glaze et al., *JGR* **102**, 6099-6108, 1997; [15] Glaze and Baloga, *J. Geophys. Res.*, **101**, 1529-1540, 1996.; [16] Fanale and Cannon *JGR.*, **83**, 2321-2325, 1978; [17] Kasting, *Icarus*, **94**, 1-13,1991

**DECAMETER-SCALE RIPPLE-LIKE FEATURES IN NIRGAL VALLIS AS REVEALED IN THEMIS AND MOC IMAGING DATA.** J. R. Zimbelman<sup>1</sup>, <sup>1</sup>Center for Earth and Planetary Studies, MRC 315, National Air and Space Museum, Smithsonian Institution, Washington, D.C. 20013-7012; jrj@nasm.si.edu.

**Introduction:** Mars Orbiter Camera (MOC) images quickly revealed the nearly ubiquitous occurrence of decameter-scale ripple-like features [1-3]. These features have been interpreted as either small dunes or large ripples [1-6]. THEMIS images now provide a new way to examine these distinctive features, in conjunction with both MOC images and field results from large terrestrial aeolian ripples. A portion of the central section of Nirgal Vallis is used here as a site to study these ripple-like features at several scales.

**THEMIS:** *IR images* - 100 m/pixel. Both daytime and nighttime IR images have been released for most of Nirgal Vallis [7]. The nighttime image (Fig. 1, left) was obtained at 3.3 H local time, and it reveals a relatively uniform temperature for the plains around the valley, warmer temperatures on crater rims and the valley wall rims, and cooler temperatures on the floors of both the valley and the larger craters. The crater thermal pattern is radially symmetric, but portions of the valley lack warm rims on their northern sides. Subtle lineations suggest winds from the southeast, including warmer wind streaks behind large craters. The daytime image (Fig. 1, right) is dominated by

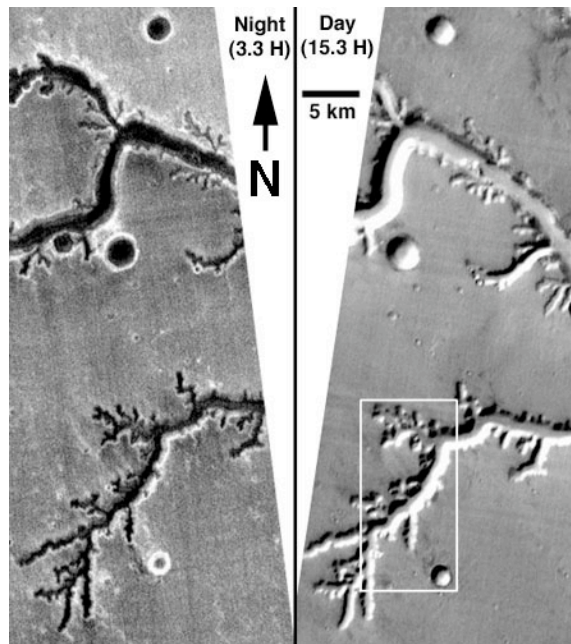


Figure 1. Nighttime (left) and daytime (right) THEMIS IR images (band 9), central Nirgal Vallis. White box shows location of Fig. 2. Centered on 27.5°S, 317.2°E. Night: I01269004, 3/29/02. Day: I016200004, 5/25/02. NASA/JPL/ASU.

slope effects; sun-facing walls of both craters and the valley are warm (bright) and the shadowed walls are cool (dark). The valley floor has a relatively average temperature similar to that of the surrounding plains, definitely NOT the warm temperature that might be expected if the cool nighttime valley floor temperatures are interpreted simply as a low thermal inertia surface. The wind streaks by large craters are slightly cooler, consistent with a higher thermal inertia than that of the surrounding plains.

**VIS image** - 19 m/pixel. The VIS image (Fig. 2) was taken concurrently with the daytime IR image in Fig. 1, and here is rotated to match the north-up orientation of the IR images. The ripple-like features are only resolved in portions of the valley floor (see 2X inset). Valley floors and plains have a similar albedo.

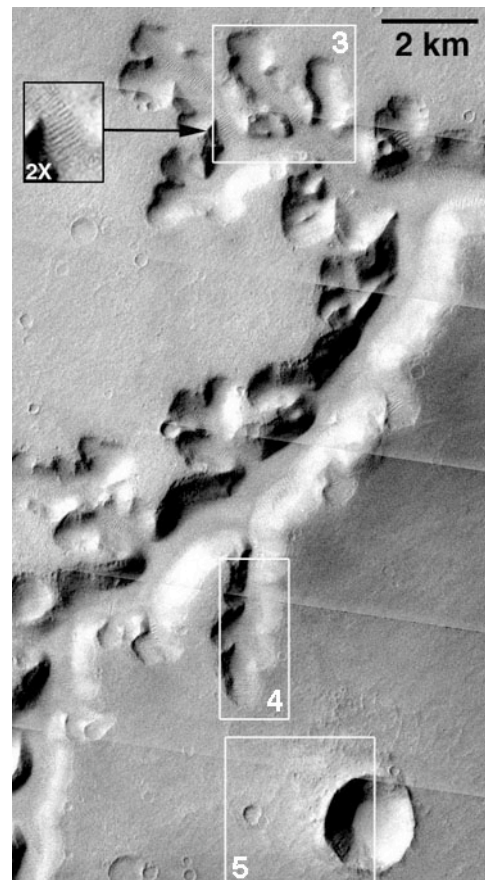


Figure 2. THEMIS VIS image of a portion of Nirgal Vallis (see Fig. 1 for context). 2X enlargement (black box inset) shows ripples on valley floor. White boxes show locations of Figs. 3 to 5. V019200005, 5/25/02. NASA/JPL/ASU.

**MOC: Image E02-02651, 2.8 m/pixel.** MOC reveals exquisite details of the ripple-like features in Nirgal Vallis. Numerous ripple-like features occupy the valley floor, with ridge crests generally transverse to the valley axis, displaying crest-to-crest wavelengths of from 30 to 100 meters (Fig. 3). This pattern is consistent with wind predominantly parallel to the valley axes, confined by the valley topography. Small impact craters are present on some rippled areas (arrows, Fig. 3). Valley branches on the southern side of the main valley display similar ripple-like patterns on their floors (e.g. Fig. 4), indicating the floor feature characteristics are not the result of localized conditions.

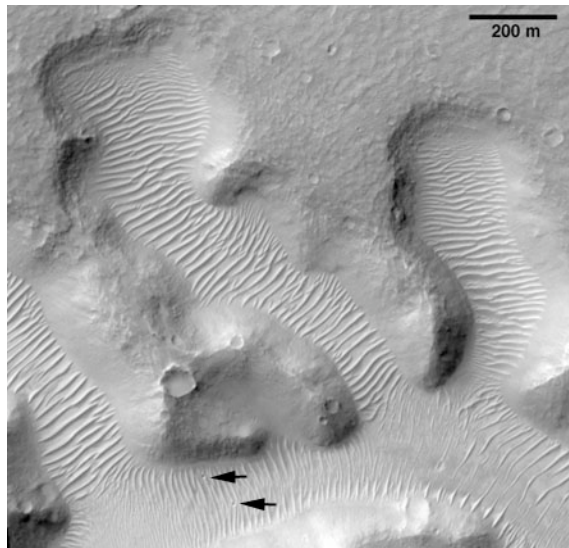


Figure 3. Ripples on the floor of Nirgal Vallis (see Fig. 2 for context). Two impact craters (arrows) are superposed on the ripples. NASA/JPL/MSSS.

Valley wall segments show no distinguishing differences across valley segments. Although illumination conditions vary with valley orientation, opposing valley walls show no evidence of substantial differences in wall texture or morphology on opposite sides of the valley. This point is relevant in relation to localized thermal asymmetries for some valley segments, as noted above.

The MOC image shows that ripple-like features are not confined solely to the valley floor. The surrounding plains south of the valley show isolated ripple-like features (Fig. 5) in an area that corresponds to a slightly lower nighttime temperature than that of the plains as a whole. North of the large crater in Fig. 5, in an area of slightly higher nighttime temperature, the plains surface has a scoured texture that might be due to enhanced aeolian erosion within the zone downwind of the crater. The upper part of the crater rim shows layered outcrops that are the likely cause of the warm



Figure 4. Ripples on floor of a Nirgal Vallis branch valley (see Fig. 2 for context). NASA/JPL/MSSS.

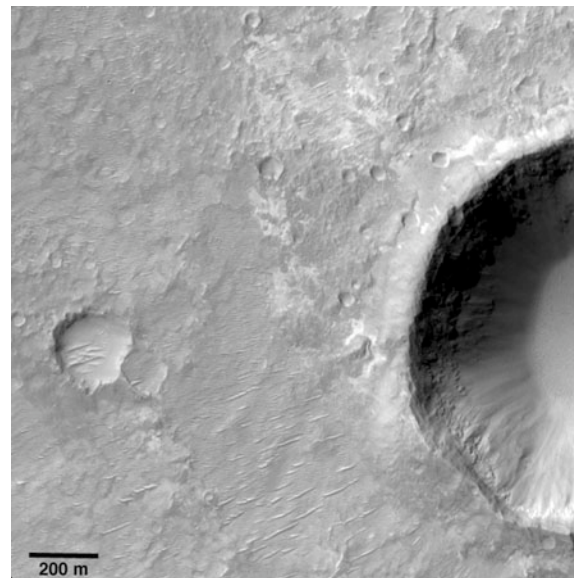


Figure 5. Isolated ripples on plains south of Nirgal Vallis (see Fig. 2 for context). Ripples correspond to colder area west of crater in the nighttime thermal image (Fig. 1). NASA/JPL/MSSS.

nighttime temperatures characteristic of the larger craters in this area (e.g. Fig. 1). The crater floor lacks distinctive morphology, even at MOC resolution, so that it is unlikely that the cold nighttime temperatures in the crater are due to unobserved ripples.

**Field Examples:** Field studies are underway to document large aeolian ripples throughout the western United States [5, 6]. All large ripples observed to date are covered with a thin accumulation (often a monolayer) of coarse particles, ranging from granules to small pebbles (2 mm to ~1 cm in diameter), over a substrate of medium sand (Fig. 6) to fine silt. Some large ripples have smaller coarse-particle ripples superposed on their lee (wind-shadowed) sides (Fig. 6). Large aeolian ripples only occur in locations displaying a bimodal particle size distribution (medium sand



Figure 6. Aeolian ripples at Great Sand Dunes National Monument, central Colorado. Large ripples have a wavelength of ~3.7 m (see Fig., 7). Sand showing typical aerodynamic ripples advanced from lower right. White card is 10 cm long. JRZ, 9/20/02.

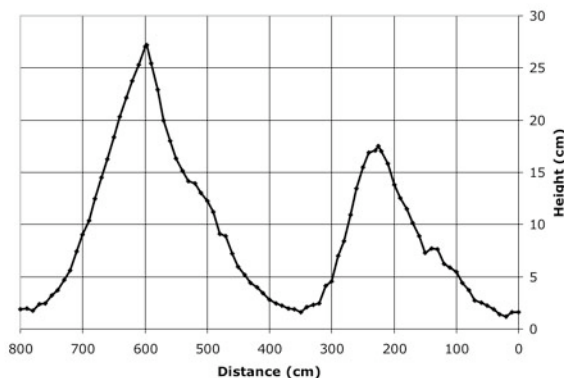


Figure 7. Profile across two large aeolian ripples at Great Sand Dunes National Monument (see Fig. 6). A  $2.2^\circ$  regional slope has been removed from the profile, and the horizontal axis is reversed here to match the orientation seen in Fig. 6. ~15X vertical exaggeration.

and the coarser particles), with the large particles often originating on surrounding hills [5]. Ripples have been measured (e.g. Fig. 7) with wavelengths ranging from ~60 cm to nearly 10 m, the later being comparable to the smallest wavelength ripple-like features observed in MOC [6].

Measured ripple profiles indicate that some examples are highly asymmetric (e.g. lee slope of  $22^\circ$  and stoss slope of  $6^\circ$ ) [6], while others are more symmetric (e.g. Fig. 7). Trenching into the ripples does not reveal extensive internal layering, although some examples did show layering parallel to avalanching down the lee slope. The largest ripples (wavelengths  $>5$  m) documented in the southwestern United States occur on playa margins and are cored with fine silt instead of the medium sand typical of all large ripples found on a sand substrate [6].

**Discussion:** The Martian ripple-like features are likely not active under present atmospheric conditions, as evidenced by the impact craters on some of them (Fig. 3). The Martian features are most often higher albedo than their surroundings [2], except where they occur on the surface of large (dark) sand dunes [3]. What is the thermal inertia of the ripple materials? This is difficult to quantify specifically, but the THEMIS nighttime IR images provide important new constraints to the question. The nighttime thermal image of central Nirgal Vallis (Fig. 1) indicates that the ripple-covered floors of Nirgal Vallis have a lower effective thermal inertia than that of the surrounding plains, which are typically  $280$  to  $300$  ( $\text{J m}^{-2} \text{s}^{-1/2} \text{K}^{-1}$ ) in this part of the planet [8]. With a thermal inertia  $<280$ , the ripples has a lower thermal inertia than that of the dark aeolian materials trapped within large craters [9].

The thermal inertia signature of the ripple-like features on Mars is not what was originally anticipated if these features are directly analogous to large terrestrial aeolian ripples with a relatively thin surface coating of coarse particles [5]. A low nighttime temperature without an elevated daytime temperature might indicate an albedo effect, where the entire diurnal temperature curve has been lowered due to a lower surface albedo, but this is not consistent with the similar overall albedos of both the Nirgal Vallis ripples and the surrounding plains (Figs. 2 to 4). One hypothesis for explaining the observed thermal characteristics of the rippled surfaces is that a relatively thin ( $<1$  cm) dust layer has become aerodynamically trapped in and around the coarse particles on the ripple surface. This scenario represents a reduced-scale analogy to dust and sand that becomes trapped around bushes and large rocks in terrestrial deserts. Such a thin dust layer might not alter the reflectance enough to affect the apparent albedo in THEMIS VIS and MOC images,

but still depress the nighttime temperatures relative to the more dust-free surface of the surrounding plains.

An alternative hypothesis is that the coarse particles involved in making Earth-like large aeolian ripples on Mars are aggregates of fine dust or sand, similar to sand-sized dust aggregates previously proposed for sand-sized materials on Mars [10]. There is no obvious mechanism for induration of a sand-sized deposit that produces a thermal signature like the one displayed in the THEMIS images of rippled surfaces. It also seems unlikely that a hypothesis requiring ripple particles that are somehow unique and distinct from the dark sand typical of most large sand dunes on Mars [e.g. 2] is viable, given the relatively uniform appearance of the ripple-like landforms across a large portion of the Martian surface [4, 6]. The kinds of complex surface particle distributions suggested in the above hypotheses have diurnal thermal properties that should be testable with multiple THEMIS nighttime IR coverage of rippled surfaces obtained at different times of night. It is anticipated that such a diurnal assessment procedure will be a focus of future study as more THEMIS data are released.

**References:** [1] Malin M. C. et al. (1998) *Science*, 279, 1681-1685. [2] Edgett K. S. and Malin M. C. (2000) *JGR*, 105, 1623-1650. [3] Malin M. C. and Edgett K.S. (2001) *JGR*, 106, 23429-23570. [4] Zimbelman J. R. and Wilson S. A. (2002) *LPS XXXIII*, Abstract #1514. [5] Williams S. H. et al. (2002) *LPS XXXIII*, Abstract #1508. [6] Wilson S. A. et al. (2003) *LPS XXXIV*, Abstract #1862. [7] THEMIS web site, <http://themis.la.asu.edu/>. [8] Mellon M. T. et al. (2000) *Icarus*, 148, 437-455. [9] Edgett K. S. and Christensen P. R. (1994) *JGR*, 99, 1997-2018. [10] Greeley R. (1979) *JGR*, 84, 6248-6254.

**THE MARS RECONNAISSANCE ORBITER (MRO) MISSION.** Richard W. Zurek, MRO Project Scientist, Mail Stop 183-335, Jet Propulsion Laboratory, 4800 Oak Grove Drive, Pasadena CA 91109 (richard.w.zurek@jpl.nasa.gov).

In August 2005, NASA's Mars Exploration Program (MEP) will launch the Mars Reconnaissance Orbiter (MRO) to Mars. Carrying a suite of six science instruments, UHF radio relay, and two technology demonstration packages, the MRO Mission pursues the NASA MEP "Follow the Water" strategy through a series of remote sensing observations. These are designed to characterize the current Mars climate, including the thermal structure and circulation of its atmosphere, the stratigraphy and composition of its surface, and the three-dimensional structure of the uppermost ground layer. In addition, the MRO will provide globally distributed data to be used to identify and characterize future landing sites that have a high potential for further scientific discovery.